Source Apportionment of Size Resolved Airborne Particulate Matter on Sable Island, Nova Scotia, Canada

by

Yunchen Li

Submitted in partial fulfilment of the requirements
for the degree of Master of Applied Science

at

Dalhousie University

Halifax, Nova Scotia

December 2017

Table of Contents

List of Tables

List of Figures

Abstract

Marine biogenic VOC rapidly undergo gas-to-particle conversion, and can serve as a significant natural source of ultrafine airborne particulate matter, that can alter global climate. However, the role phytoplankton emissions play in UFP and cloud formation, and subsequent mediation of climate are still not well understood. In this study, the relationship between marine phytoplankton abundance and size-resolved particle number and mass was studied on Sable Island as part of the NASA NAAMES study. Utilizing the USEPA PMF source apportionment model yielded four size-resolved factors (sources of PM): sea spray (2.2% of total UFP), secondary marine biogenic particles (78.2%), long range transport (4.4%) and island surface dust (15.2%). The strong correlations between UFP (20-30 nm & 30-50 nm) and chlorophyll a ($R^2 = 0.815$ and $R^2 = 0.815$), was the most salient feature of this study and provides powerful insight into ocean-atmosphere dynamics that remain high uncertainty in global climate.

List of Abbreviations Used

APS	TSI aerodynamic particle sizer model 3321
ASO_4	Ammonium sulphate
BC	Black carbon
CCN	Cloud condensation nuclei
Chl a	Chlorophyll a
CMB	Chemical Mass Balance
CO_2	Carbon dioxide
DMS	Dimethyl sulphide
DRX	TSI DustTrak DRX model 8533
GPC	Gas-to-particle conversion
HYSPLIT	Hybrid Single-Particle Lagrangian Integrated Trajectory
IPCC	Intergovernmental Panel on Climate Change
LRT	Long range transport
MODIS	Moderate Resolution Imaging Spectroradiometer
NASA	National Aeronautics and Spcae Asministration
NE US	Northeast United States
NH_3	Ammonia
$(NH_4)_2SO_4$	Ammonium sulphate
NOAA	National Oceanic and Atmospheric Administration
NO_2	Nitrogen dioxide
NO_x	Nitrogen oxides

NS	Nova Scotia
O&G	Oil and gas
O_3	Ozone
PCA	Principle Component Analysis
PM	Particulate matter
PMF	Positive Matrix Factorization
SO_2	Sulfur dioxide
SO_4^{2-}	Sulphate
SOA	Secondary organic aerosol
TSP	Total suspended particles
UFP	Ultrafine Particle
UFPM	TSI ultrafine particle monitor model 3031
USEPA	US Environmental Protection Agency
VIIRS	Visible Infrared Imaging Radiometer Suite
VOC	Volatile organic compound

Acknowledgements

I'm grateful to my supervisor Dr. Mark Gibson and Dr. Susanne Craig for their continued support, guidance and insightful advice. I am grateful to the researchers at NASA, for their support and participation in the study. I would like to thank my parents, for their continuous and generous support during my school years. I also would like to thank all the members of the Atmospheric Forensics Research Group, for their tremendous hard work on this project. Special thanks to the Environmental Studies Research Funds and Natural Resources Canada for funding the project, Gerry Forbes and Maritime Air Charter for arranging travel to Sable Island. Finally, I would like to acknowledge everyone in Environment Canada and Parks Canada for their help with instrument maintenance and data collecting. Last but not least, I would like to thank my friends and family for their continuous moral support.

CHAPTER 1. Introduction

Particulate matter (PM), also known as airborne particles or aerosols, refers to any substance, that exists as a liquid or solid in the atmosphere under normal conditions, with a size of 0.001 to more than 100 μm (Seinfeld & Pandis, 2016). In the field of atmospheric chemistry and physics, airborne particles with a median aerodynamic diameter ranging from 1 nm to 10 μm suspend in the atmosphere as PM (Seinfeld & Pandis, 2016). However, in the field of air quality, the definition is rather vague, airborne PM is defined as fine solid or liquid particles dispersed in a gas, and popular usage often describe them as a particle-air mixture. Airborne particulate matter is considered as a mixture of solid and droplets suspended in the atmosphere (Davidson, Phalen, & Solomon, 2005; Seinfeld & Pandis, 2016; World Health Organization, 2013).

Particulate matter is classified by size: PM with median aerodynamic diameters less than or equal to 10 μm are referred to as PM_{10}, PM ≤ 2.5μm ($PM_{2.5}$) are referred to as fine particles, PM between $PM_{2.5}$ and PM_{10} are referred to as coarse particles, ≤ 0.1 μm as ultrafine PM (UFP) (EPA, 2016; Gibson et al., 2009, 2013, 2015). PM are also categorized into primary and secondary particles depending on how they were generated (Seinfeld & Pandis, 2016). Primary particles come from direct emissions such as combustions (biomass burning) and sea spray. Secondary particles are formed through nucleation and gas-to-particle conversion (Fountoukis et al., 2012; Hinds, 1999; Seinfeld & Pandis, 2016). Aerosols also vary in their air dispersity properties depending upon their density and morphology. A homogeneous aerosol is an aerosol where all chemical and physical properties are identical; monodisperse aerosol can be produced in the lab

that all the particles are in the same size; polydisperse aerosols are the most common aerosols found in virtually all size-fractions but fresh gas-to-particle conversion. But these particles quickly coagulate and mix with other UFP in the air to become polydisperse (Hinds, 1999).

In a global view, major sources of airborne PM are sea-salt, mineral dusts, combustion and industrial processes (Seinfeld & Pandis, 2016). Sea-salt comes from marine emissions, it consists of sea salts as well as small contributions from halogens, sulfates, carbonates and volatile organic compounds (VOC) (Gibson, et al., 2013). The major sources of coarse particles ($PM_{2.5}$-PM_{10}) are windblown dust, sea spray, evaporated solvent and water droplets, pollens, and mechanical disruption, the major sources of fine particles are evaporation of fog and clouds.

PM is known to have an adverse impact on human health (Dockery et al., 1993). Because PM <PM_{10} are small enough to penetrate the respiratory system and from there the circulatory system; therefore, they can increase the risk of lung and heart disease (Dockery, 2009; WHO, 2013). Long-term exposure to $PM_{2.5}$ is known to be associated with a higher risk of lung cancer, and cardiopulmonary mortality as it can penetrate deeper into the lung and bloodstreams than PM_{10} (Monks et al., 2009; Pelucchi et al., 2009; Pope III et al., 2002; WHO, 2013). The World Health Organization (WHO) estimated that 3.1 million deaths were attributable to $PM_{2.5}$ in 2010 (WHO, 2013). Recently, UFP has raised researchers' interests because they not only can enter the lungs and cause disease but also can enter the brain directly through the olfactory system where they are now suspected as contributing to Dementia and Alzheimer's disease (Calde On-garcidu Nas et al., 2004; Sioutas, Delfino, & Singh, 2005). With a smaller size, higher

mass concentration, and larger surface area, UFPs can deposit more pollutants into the lung or respiratory system than $PM_{2.5}$ or PM_{10}. Therefore, to understand the impact on health it is necessary to know where the source, chemical, physical, biological and toxicological characteristics of PMs come from and what they consist of, although this falls out with the aims and objectives of this thesis (Gibson et al., 2015).

Airborne particulate matter also has an impact on climate change. PM, expecially UFP, can serve as cloud condensation nuclei (CCN) that can form fog or cloud droplets when the humidity is over 80% (IPCC, 2014; Seinfeld & Pandis, 2016). Both PM and clouds scatter and absorb incoming solar radiation. In this case, PM can significantly affect radiation balance and therefore affect weather and climate. However, there is still a great deal of uncertainty how PM-cloud interactions affect solar radiation, and therefore their impact on climate (IPCC, 2014). Marine emission is the dominant source of natural emissions to the atmosphere (Seinfeld & Pandis, 2016). However, due to the tremendous area of ocean and remote restriction, there is still a large gap in knowledge about interactions between marine emissions and atmosphere. Sable Island is a truly marine environment (with very little antrhopogenic or continental influence), therefore it is an ideal sampling site to study how secondary biogenic marine emission influence atmosphere and climate change.

1.1 Aims and Objectives of the Study

There are two objectives of this study: 1). To investigate the correlation between biogenic emissions from phytoplankton and particle formation in North Atlantic; and 2) To apportion the sources of size-resolved particulate matter on Sable Island in 2016.

CHAPTER 2. Literature Review

2.1 Atmosphere - Airborne Particulate Matter

The study of atmospheric particles relates to a wide range of fields: mass/molar concentrations, sizes, chemical compositions, phase (liquid or solid) and morphology (Seinfeld & Pandis, 2016). The most commonly measured PM property is mass concentration, it is a critical criterion for assessing health and environmental effects. In addition, most recently size-resolved particle number counts have become an important measurement metric due to their reactivity, role in CCN formation and other known or suspected health effects (Brace et al., 2014). Mass concentration refers to the mass of PM in a unit volume of air; the units normally encountered in ambient air being $\mu g/m^3$. Number concentration refers to the number of particles in a unit volume of air, and its unit is number/cm^3. Normally, when referring to health aspect of PM, mass concentration is the primary indicator (WHO, 2013), number concentration is widely used in atmospheric chemistry research, and occupational exposure in industries such as welding, electronics, material science or non-cold surgical procedures, e.g. cautery or laser surgical tools (Brace et al., 2014; McNeilly et al., 2004)

2.1.1 Particle Characteristics

Particle characteristics is an essential part in airborne PM study. Three main characteristics of PM being discussed in the presented research filed are particle size, shape, and density (Hinds, 1999). The composition and size of PM vary widely in space and time (Davidson et al., 2005). Monodisperse PM possesses particles of identical sizes, but most PM is polydisperse and consists of particles in a wide range of sizes. It is common to have a hundredfold range between the largest and smallest components

(Brimblecombe, 1996; Hinds, 1999). Therefore, size distributions are used to characterize PM assemblages. Based on Whitby and Cantrell's suggestion (Figure 2-1), according to distributions of their surface area, particles can be divided into several modes: nuclei mode (<10 nm), Aitken mode (10 – 100 nm), accumulation mode (0.1 – 2.50 μm) and coarse mode (>2.50 μm). Particles in nucleation and Aitken mode are also referred to as ultrafine particles or nanoparticles, accumulation mode particles are called fine particles, and coarse particles are under coarse mode but smaller than 10 μm (Seinfeld & Pandis, 2016).

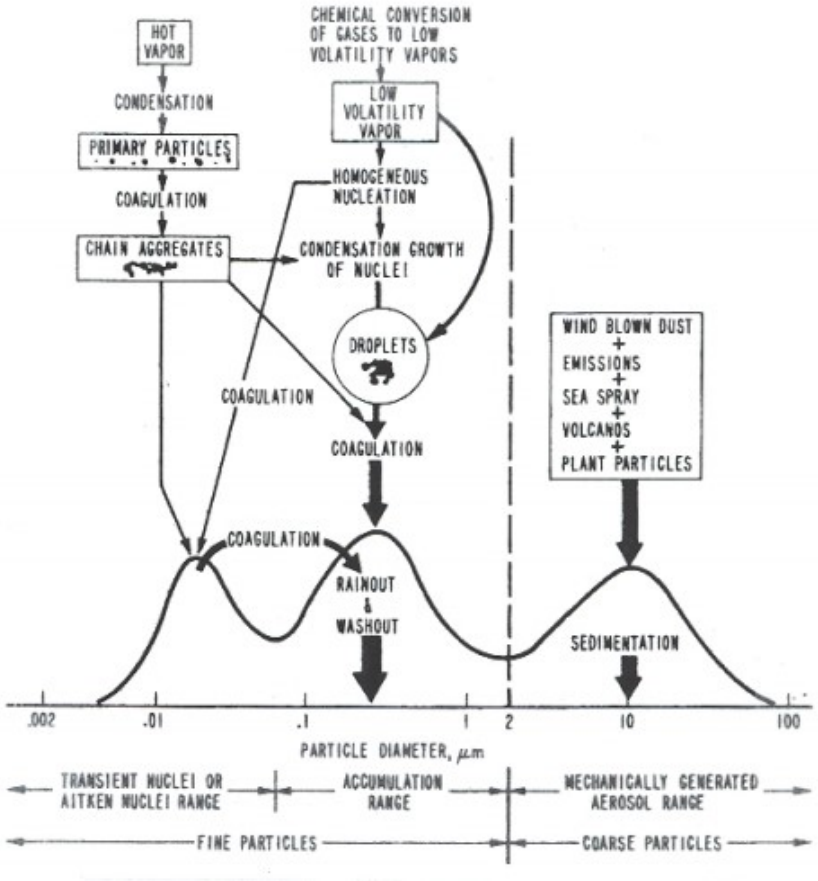

Figure 2-1. Idealized distribution of particle surface area proposed by Whitby and Cantrell, 1976 (Seinfeld & Pandis, 2016).

Size is the most important character for assessing the behavior of PM as most of their properties are determined by their size (Brimblecombe, 1996). Table 2-1 summarized a comprehensive comparison among different size fractions of particles, their source formation, chemical composition, lifetime in the atmosphere, and fate and transport. Coarse particles tend to move slowly and have shorter lifetimes (minutes to hours), and can be removed from the atmosphere easily by rainfall or dry deposition. Ultrafine particles, or particles in nuclei and Aitken modes, can move faster but also have short lifetime (minutes to hours) due to the fact that they are principally removed by coagulation with larger particles or grow into fine particles via condensation and coagulation. Fine particles, or particles in accumulation mode, are comparatively hard to be removed due to their moderate size, and therefore accumulate and persist longest (days to weeks) (Hinds, 1999; Seinfeld & Pandis, 2016; Wilson & Suh, 1997).

Table 2-1. Comparison of particle fractions (Wilson & Suh, 1997)

	Fine		Coarse
	Nuclei	Accumulation	
Formed from:	Combustion, high-temperature processes, and atmospheric reactions		Break-up of large solids/droplets
Formed by:	Nucleation Condensation Coagulation	Condensation Coagulation Evaporation of fog and cloud droplets in which gases have dissolved and reacted	Mechanical disruption (crushing, grinding, and abrasion of surfaces) Evaporation of sprays Suspension of dusts Reactions of gases in or on particles
Composed of:	Sulfates Elemental carbon Metal compounds Organic compounds with very low, saturation vapor pressure at ambient temperature	Sulfate, $SO_4^{=}$ Nitrate, NO_3^- Ammonium, NH_4^+ Hydrogen ion, H^+ Elemental carbon Large variety of organic compounds Metals: compounds of Pb, Cd, V, Ni, Cu, Zn, Mn, Fe, etc.	Suspended soil or street dust Fly ash from uncontrolled combustion of coal, oil, and wood Nitrates and chlorides from HNO_3 and HCl Oxides of crustal elements (Si, Al, Ti, and Fe) $CaCO_3$, NaCl, and sea salt Pollen, mold, and fungal spores Plant and animal fragments
		Particle-bound water	Tire, brake pad, and road wear debris
Atmospheric half-life:	Minutes to hours	Days to weeks	Minutes to hours
Removal processes:	Grows into accumulation mode	Forms cloud droplets and rains out Dry deposition	Dry deposition by fallout Scavenging by falling rain drops
Travel distance:	<1 to 10s of km	100s to 1000s of km	<1 to 10s of km (100s to 1000s in dust storms)

Particle morphology is also important as it can provide information about the state of the particle, its source, potential health effects, behavior in the atmosphere and its optical properties (Beranek, Imre, & Zelenyuk, 2012). Liquid particles are generally spherical, but solid particles are usually irregularly shaped. For aspherical particles, median aerodynamic diameter is used as the diameter for spherical particles, it is defined as the diameter that a spherical particle with density of 1000 kg/m^3 would have when it has the same velocity as aspherical particles of interest (Slowik et al., 2004), e.g. a 1-µm aerodynamic diameter particle behaves aerodynamically like a 1-µm water droplet, regardless of its shape, density or size (Hinds, 1999). Aerodynamic diameter is usually selected by inertial methods such as impactors and cyclones, with the remaining desired size of particles flowing into a measurement device or captured on a filter. If captured on a filter, the chemistry, morphology and toxicology can then be studied (Gibsom, et al., 2009)

The density of PM highly depends on their sources and shapes (Hinds, 1999; Slowik et al., 2004). Particles from fermentation processes or spray may share similar density and smell with their parent materials. However, particles from combustion may have a very different density from their sources due to voids being created (Hinds, 1999). Particles with voids are less dense than those without voids. Also, combustion particles aggregate in different ways, some of them aggregate and become compact while some of them aggregate loosely (Slowik et al., 2004).

2.1.2 Particle size distribution

Particle size distribution is an important physical property of airborne PM and is influenced significantly by gas-to-particle conversion, and therefore affect cloud

formation and the scattering and adsorption of light (Burkart et al., 2017). As the size of PM is dynamic, the changes occur when a vapor condenses, or particles collide and adhere to each other. Normally, mathematical approaches are used to describe particle size distribution (Seinfeld & Pandis, 2016). A summary of particle information is provided by forming a series of continuous size fractions; the number concentration of particles in each fraction is also determined (*unit*: cm^{-3}). The distribution is then displayed in the form of a histogram. The size range for each size fraction may differ; for example, for the UFP size fraction observed in this study ranges between 20-30 nm and 200-800 nm. The size bins of these size fractions also vary, which can bias in way the data is presented, as the area below the curve will not be proportional to the number concentration, therefore PM size distributions are normalized by dividing the concentration by the corresponding size range. The value of aerosol distribution n_i for a size fraction was expressed as the ratio of the absolute aerosol concentration N_i and the size ΔD_p (Seinfeld & Pandis, 2016):

$$N_i = n_i * \Delta D_p$$

As ΔD_p needs to be as small as it can be, so the limit $\Delta D_p \rightarrow 0$ will be taken, and dD_p will be adopted. Therefore, the size distribution function $n_N(D_p)$ can be expressed as

$n_N(D_p)dD_p$ = number of particles per cm^3 of air having diameters

in the size range D_p to $(D_p + dD_p)$

To show a better distribution graph $\ln D_p$ or $\log D_p$ are used instead of D_p, it will then be expressed as

$n_N(\ln D_p)d\ln D_p$ = number of particles per cm^3 of air having diameters

in the size range $\ln(D_p)$ to $(\ln D_p + d\ln D_p)$

Figure 2-2 below shows the size distribution with regards to number and volume; nucleation mode particles account for most of the numbers while fine particles account for most of the volume. It is shown that fine mode particles account for most of PM surface area, which is a result of their coagulation history. Particles in nuclei and accumulation modes tend to coagulate with each other and this enlarges the surface area.

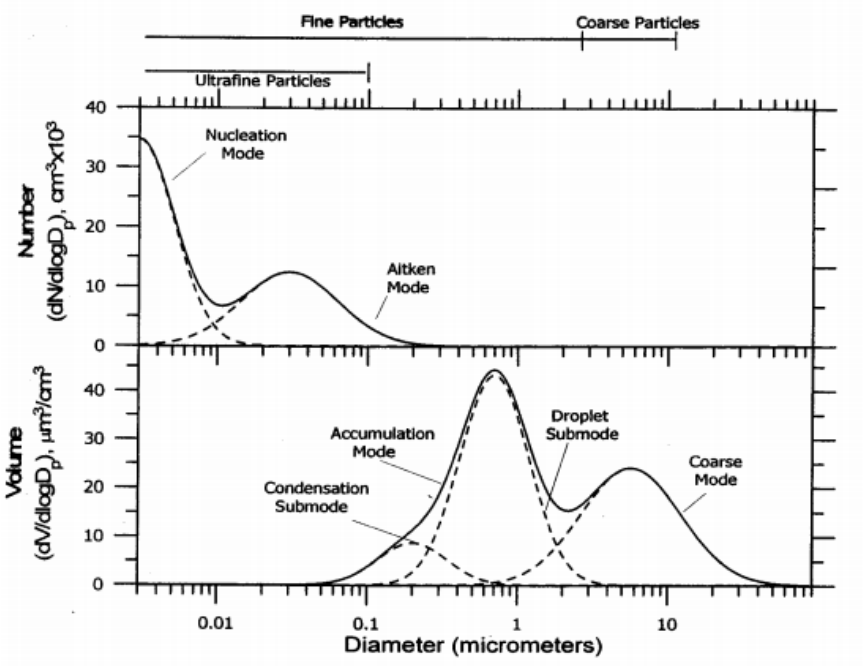

Figure 2-2. Atmospheric aerosol number and volume distributions versus particle size (Wilson & Suh, 1997).

2.1.3 Particle Sources and Species

Particle sources can be classified differently, and can be separated into anthropogenic and natural sources (Hinds, 1999); spatial and widespread surface sources (Hobbs, 1993); or primary and secondary PM sources (Brimblecombe, 1996), etc. In this study, the anthropogenic and natural sources will mostly be discussed. Anthropogenic sources include combustion, construction, mining, and some other human activities.

Natural sources are related to marine emissions (e.g., sea spray, biological PM), forest fires, desert dust (Hobbs, 1993).

The ocean covers 71% of the Earth's surface area; it used to be considered as one of the most significant sources of atmospheric PM, mainly in the form of sea spray, which makes sea spray a major natural source of coarse PM (Hobbs, 1993; Teather et al., 2013). Sea spray was initially considered to be dominated by sea salt, coming from windblown sea surface bubbles and breaking waves (Fuzzi et al., 2015; O'Dowd et al., 2014). However, it became evident that it not only contains sea salt but also contains enriched compounds from marine biomass metabolism, which can form secondary organic particles (SOP) (Fuzzi et al., 2015; Hobbs, 1993; O'Dowd et al., 2014). In a global view, sea spray aerosol accounted for 1400-6800 Tg/yr of PM, where SOP is estimated to contribute to 14 Tg C/yr (Fuzzi et al., 2015; IPCC, 2014). In a coastal city such as Halifax, sea spray accounts for 18.3% of $PM_{2.5}$, while long-range-transport (LRT) accounting for 47% of $PM_{2.5}$ (Gibson, Pierce, et al., 2013; World Health Organization, 2013).

Mineral dust particle is a dominant component of airborne PM globally (Mahowald et al., 2011). According to Ginoux et al. 2012, mineral dust accounts for 75% of the global dust emissions where 25% are from anthropogenic emissions (mostly from agriculture and resuspension of dust particles by traffic). Natural emissions are caused by wind blowing undisturbed area. Global largest mineral dust source is the Sahara-Sahel region of northern Africa; central Asia is the second largest dust source region (Fuzzi et al., 2015; Seinfeld & Pandis, 2016). The main components of mineral dust are quartz, clays, calcite, gypsum and iron oxides. The mean lifetime of dust particles in the air is

two weeks, which allows for thousands of kilometers travel. Because of such long lifetime, mineral dust is growing into a global air quality concern (Seinfeld & Pandis, 2016; Wilson & Suh, 1997). Construction sites are also becoming a major concern of PM as they are generating dust from concrete, cement, wood, stone, and silica, all of which can contribute to health problems, especially most of them are happening in cities or areas with a large population (Teather et al., 2013).

The fire has been a feature of the Earth for a long time. Combustion processes are the dominant contributor to anthropogenic sources (Seinfeld & Pandis, 2016). It also includes biomass combustion, fossil fuel exhaustion, power generation, as well as wildfire which is not part of anthropogenic activities but can be one indirect result of anthropogenic activities. Most of biomass burning occurs in tropics and is a major source for black carbon, organic carbon (VOCs) and ozone precursors (Dohoo, Guernsey, Gibson, & Vanleeuwen, 2013; Seinfeld & Pandis, 2016; Wheeler et al., 2014). In industrial factories including fossil fuel combustions, fuel combustion with impurities can result in the emission of nitrogen and sulfur containing gases, which oxidize in the atmosphere to form nitrates and sulfates of ammonia (Gibson, Heal, et al., 2013; Gibson, Kundu, & Satish, 2013). There are hundreds of wildfires in North America every year and generate a tremendous amount of primary and secondary PM emission to the atmosphere. Most of them can travel thousands of kilometers before being removed from the atmosphere (Gibson, Heal, et al., 2013; Palmer et al., 2013; Wheeler et al., 2014).

The major sources of coarse particles are from the break-up of large solids or droplets such as windblown dust, sea spray, evaporated sprays, pollens, mechanical disruption (e.g. grinding, crushing). Fine particles usually are formed from combustion

and gaseous reactions by coagulation of ultrafine particles and evaporation of fog and clouds (Figure 2-1) (Wilson & Suh, 1997). Fine and coarse particles have different chemical compositions and sources, so they are not transferrable. However, fine particles can be from coagulation of particles in nucleation mode (Hinds, 1999; Seinfeld & Pandis, 2016). Aitken-mode ultrafine particles (20-100 nm) come from combustion emission and gas-to-particle conversion (Seinfeld & Pandis, 2016).

Surface PARticulate mAtter Network (SPARTAN), compostion and real-time sampling network at various sites around the world (marine, urban, rural), conducted a study on the source distribution of $PM_{2.5}$ (Figure 2-3). The major $PM_{2.5}$ components found were ammonium nitrate (ANO_3) and ammonium sulfate (ASO_4). ANO_3 and ASO_4 can be formed from the gas-to-particle conversion of NH_4^+, which in most areas are from agriculture sources and fertilizer applications (Snider et al., 2016; Wang et al., 2015). RM is residue matter which is mainly organics; EBC is equivalent black carbon which is primary PM emitted from combustion, TEO is trace elemental oxides which are summation of trace elements such as Zn, V, Ni, Cu, As, Se, Ag, Cd, Sb, Ba, Ce, and Pb; PBW is particle-bound water, which is basically water uptake in inorganics such sea salt, ANO_3, and ASO_4. κ_v is the aerosol hygroscopicity parameter representing the contribution of water uptake of each component (Snider et al., 2016).

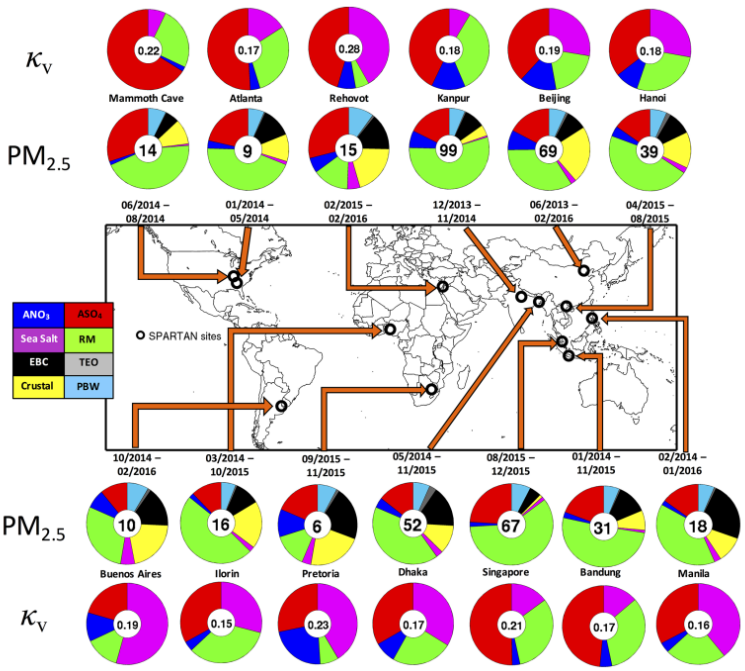

Figure 2-3. Global $PM_{2.5}$ speciation (Snider et al., 2016).

2.1.4 Health effects

Air pollution has an extensive history, which can be traced back to 1272 when England was still governed by King Edward I; he was trying to clear the sky by banning the use of "sea coal" in London, a mineral coal from the sea. According to the record, one of the earliest publications dealing with air pollution was a pamphlet written by John Evelyn, who was also the founding members of the Royal Society, published in 1661. However, it was not until recent centuries, after a dreadful fog in London back in 1873, or a severe fog in 1930 in Meuse Valley, Belgium, that air pollution became a major global issue (Wark, Warner, & Davis, 1977). Today we still see extreme air pollution events in major cities, such as recent frequent occurrences of thick haze in eastern China (Huang et al., 2014; Targino et al., 2016).

Airborne pollutant includes smoke, fumes, soot, smog, and other combustion products, also natural particles such as surface dust, pollen, and spores. It includes not only primary particles coming directly from exhaustion and emissions of pipelines and cars but also secondary particles, which form from condensation of vaporized materials (sulfate and nitrate) or the oxidation of gases in the atmosphere. So particulate air pollution is a mixture of contaminants from various sources (Dockery, 2009; Hinds, 1999).

A link between mortality and air pollution was established dating back to 1980's by Drs. Joel Schwartz, Allan Marcus, Arden Pope and David Bates (Dockery, 2009). Previous studies conducted by Dr. Joel Schwartz and Dr. Arden Pope showed that airborne particulate matter have a positive correlation with mortality, a decrease in concentration of PM could lead to a decrease mortality rate. Later in 2000, WHO started Global Burden of Disease project, the effects of outdoor and indoor air pollution, water quality,and climate change on different ages, sex and world regions were assessed globally. The study revealed the direct link between outdoor air pollution and increased cardiopulmonary disease mortality as well as trachea mortality and acute respiratory infection in children (Cohen et al., 2005).

The human respiratory system is effective at filtering and removing harmful substances such as coarse PM before they reach the lower airways and lung tissue, only a fraction containing the smallest particles can reach deep into the lung. Breathing faster can help with diminishing UFP deposition due to less time for sedimentation and diffusion (Harrison, 1990). Some airborne pollutants may have instant effects, for example, after being exposed to sulfur dioxide (SO_2) for few minutes, some individuals can suffer airway constriction (Dominici et al., 2006; Harrison, 1990; Pope III et al., 2002; WHO, 2013).

Short-term exposure (minutes to months) to high levels of PM in winter is also accompanied by still and cold anticyclonic weather conditions, in the meantime, associated cold snaps can also lead to increased mortality from cardiac and respiratory upset (Harrison, 1990). Short-term exposure can also lead to acute effects which include but not limited to cardiovascular and respiratory constriction (Dominici et al., 2006) and poor vascular function and diastolic blood pressure increase (Brook et al., 2009). Some pollutants only affect individuals after prolonged or repeated exposure, which may take years. Medium-term (months - 10 years) can result in increased chance of a cough, wheeze, asthma, and bronchitis, also infection and reduction in lung function and lung growth in children. Long-term (more than ten years) exposure can lead to chronic effects which include pregnancy loss, increased mortality from cardiopulmonary diseases and lung cancer and shorter lifespan (Ha et al., 2017; Harrison, 1990; Pope III et al., 2002; Teather et al., 2013).

2.1.5 Environmental effects

Homogeneous nucleation is the formation of PM from a supersaturated vapor without condensation. Heterogeneous nucleation or condensation is the formation and growth of particle stimulated by the presence of condensation nuclei or ions. Condensation is the dominant process for the formation of clouds in the atmosphere. Even in unsaturated vapor, the attractive forces between molecules, such as Van der Waals forces, can stimulate the formation of PM chunk. The PM chunks are formed continuously but are continuously decomposed. When the vapor is supersaturated, the PM chunk number concentration increases to the frequent collision point, and this process is called “agglomerates”. When “agglomerates” reaches a certain size, the PM chunk will become stable and condensate to form a larger particle. In photochemical

processes in the atmosphere, some gaseous reactions are stimulated by UV light and produce compounds that can be easily vaporized. These compounds can exist at high concentrations in the atmosphere and form particles by homogeneous nucleation; it is called gas-to-particle conversion (Hinds, 1999; Seinfeld & Pandis, 2016).

Particulate matter can modify atmospheric radiation as well as alter cloud properties (Mahowald et al., 2011). The existence of particles in the air boosts the condensation of water droplets in the air (by heterogeneous nucleation). The airborne PM on which cloud droplets form determine the concentration and sizes of droplets, and therefore it determines the properties and reflection ratio of clouds (Hinds, 1999; Hobbs, 1993). Cloud droplets formed from PM tend to have smaller size and larger number concentration, which result in clouds with higher albedo. In this way, airborne PM can alter incoming radiation and cause indirect effects on cloud cover, which can cause a cooling effect and therefore affect climate (Hansen, Sato, Kharecha, & Von Schuckmann, 2011; Hobbs, 1993; Seinfeld & Pandis, 2016). Some particles absorb light, which has a net warming effect on climate and the Earth's surface. When the temperature is increased, there will be more vapor in the air; as vapor is a greenhouse gas, it will warm the earth directly (Hinds, 1999; Seinfeld & Pandis, 2016; Solomon & Hopke, 2008).

UFP formed from nucleation of gases and coagulating into detectable sizes (>20 nm) have been observed at the marine area around the world (Kulmala et al., 2004; Vaattovaara et al., 2006). UFP can grow into larger particles and scatter incoming radiation whereby may affect the atmosphere radiation budget as well as cloud physics. Furthermore, they can interact with anthropogenic gases (e.g. condensation of HNO_3 and

halogens) and influence marine and continental biochemical system (Fuzzi et al., 2015; Slingo, 1990; Vaattovaara et al., 2006).

Mineral dust particles affect climate directly and indirectly; they can alter marine biogeochemistry and human health. Iron oxides from terrestrial dust can absorb visible radiation and warm atmosphere, while mineral dust particles are also scattering radiation which leads to surface cooling. These effects may impact wind field and climate regionally (IPCC, 2014). In addition, dust mediates carbon uptake by providing iron, a limiting phytoplankton nutrient, in many ocean regions. Mineral dust mainly contribute coarse and fine particles (Fuzzi et al., 2015).

When excessive SO_2 and NO_x are released into the air, they can react with water molecules and cause an elevated level of hydrogen ions (low pH) in the atmosphere. As SO_2 can react both as an oxidizing agent and an reducing agent, it can react with O_2, water, and metal salts through photochemical or catalytical reaction to form SO_4^{2-} which is a form of sulfuric acid. Excessive gaseous SO_2 can enter vegetation stomata and disrupt leaf cell structure (Gibson et al., 2013); while liquid acids deposit in the form of precipitation, they tend to have low pH and can affect plant life and aquatic environments, as well as cause damage to limestone, stone statues or construction base for buildings (Bell & Treshow, 2002; Querol et al., 2004).

2.2 Ocean - Phytoplankton

Living in the ocean are millions of tiny plants known as phytoplankton. The word “phyto-” comes from the Greek words φυτόν (phyton), meaning "plant"; and “plankton” comes from πλαγκτός (planktos), meaning "wanderer" or "drifter”. Like land plants, the

growth of phytoplankton requires light, inorganic carbon (i.e. CO_2), water, mineral nutrients, and ambient temperature. They take up carbon dioxide (CO_2) from water and energy from the sun, then produce carbohydrates and O_2 via photosynthesis (Boney, 1989). Phytoplankton are some of Earth's most critical organisms not only because they generate more than 40% of the oxygen in the atmosphere (Hader & Schafer, 1995) but also because they are the primary producers of the ocean—the organisms that form the base of the food chain (Saltzman & Cooper, 1989).

2.2.1 Ocean - atmosphere interaction: VOC - DMS

Volatile organic compounds (VOCs) are a diverse group of chemicals mostly emitted from anthropogenic activities (e.g. indoor cooking) and biomass (e.g. biological stress) (Dohoo, Read Guernsey, Gibson, & Van Leeuwen, 2015). VOCs have low boiling points and high vapor pressure, which allows them to evaporate easily into the atmosphere and contribute to forming hydroxyl radicals. Because of this, VOC can have huge impacts on Earth systems, including mediating stratospheric ozone, the formation of ground-level ozone and secondary ultrafine particle formation (Halsey et al., 2017; Jacob et al., 2002; Singh, Kanakidou, Crutzen, & Jacob, 1995). Phytoplankton account for most marine VOCs. Like land plants, phytoplankton emit VOC when suffering physical (e.g. temperature change, oxidative) or biological (e.g. starving, predators) stress as well as intracellular metabolism. VOCs emitted from phytoplankton are halocarbons (e.g. bromomethane, iodomethane), hydrocarbons (e.g. isoprene) (Moore, Oram, & Penkett, 1994) and DMS (CH_3SCH_3). It has been established that DMS is the result of enzymatic cleavage of dimethylsulfoniopronic acid (DMSP) (Saltzman & Cooper, 1989).

A hypothesis "CLAW" was proposed by Charlson et al. (1987) that the Earth's climate could be affected negatively by the production of DMS, which was proved to be undergoing series of chemical reactions that would increase cloud formation, and therefore cool down the Earth via albedo effect (Charlson, Pompei, Ales, & MacKenzie, 1987; Quinn & Bates, 2011; Saltzman & Cooper, 1989). However, some recent laboratory studies and modelling efforts bring into question the validity of the hypothesis (Quinn & Bates, 2011). Chlorophyll-a concentration was a major criterion used to represent phytoplankton biomass in the remote marine area.

2.2.2 North Atlantic Phytoplankton Bloom

Phytoplankton growth strongly depends on light, nutrition and temperature. Therefore, it follows strong seasonal patterns. Like all plants, they depend upon energy from sunlight to drive the photosynthetic process. Additionally, water temperature has a strong impact on growth (Henson, Dunne, & Sarmiento, 2009; Saltzman & Cooper, 1989). Every spring, the North Atlantic hosts one of the largest phytoplankton blooms in the world (Siegel, Doney, & Yoder, 2002). During the winter, the water column mixed layer is deep as a result of a breakdown of the thermocline and strong wind driven mixing. The sun angle is low, which reduces the average light intensity, so phytoplankton do not have enough light for growth. When spring comes, the incident light increases while mixing layer shallows, which leads to an increase in average light intensity, and therefore, a boost in energy uptake from the sun leading to the initiation of the phytoplankton bloom (Boney, 1989; Henson et al., 2009).

The Scotian Shelf is a highly productive area of the Canadian northwestern Atlantic Ocean (Shadwick et al., 2011). This shelf region is a productive spot for high-value

multi-species fisheries (Fournier, Marra, Bohrer, & Det, 1977). It is heavily influenced by outflow from the Gulf of St. Lawrence; it also receives a downstream flow of water from the Labrador Sea (Shadwick et al., 2011). During the spring bloom, relatively large diatoms dominate the phytoplankton assemblage. The diatoms rapidly deplete nutrients in the water column, and the spring bloom terminates when nutrient levels can no longer support their growth requirements. As the season progresses into late spring and summer, the nutrient-depleted surface water warms and stratifies, creating conditions favorable for the growth of smaller cells such as pico- and nanophytoplankton (Craig et al., 2015). A smaller, subsidiary bloom is often observed in the autumn as increasing storm activity entrains deeper, nutrient rich water into the surface layer that is still relatively well-lit during these months.

2.3 Sable Island

2.3.1 Location and History

All measurements of this study were conducted on Sable Island (43.9337° N, 59.9149° W), located on Northwest of Atlantic, 300 km southeast of Halifax, and 180 km off the coast of Nova Scotia (43.55° N; 60.01° W). Sable Island, named after French word for sand (*le sable*), is a crescent-shaped sandbar approximately 1 km wide and 40 km long (Duderstadt et al., 1998; “Friends of Sable Island Society | A Brief History of Sable Island,” 2012). Error! Reference source not found. below shows the location of Sable Island on the map. Because of its well-known horses, unique ecosystem and unique location, Sable Island became a national park in 2013 (Government of Canada, 2014).

Figure 2-4**.** Location of Sable Island (Adapted from Hayes. A., 2013).

Sable Island station managed by Parks Canada and Environment Canada, is the only staffed facility on the island. The climatological record on the island began on as early as 1871 after the establishment of the Meteorological Service of Canada (MSC). Ocean/air chemistry/air quality studies have been carried out on Sable Island since 1960's, the studies include pollen measurements, aerosol particle counting, soot measurement, gaseous pollutants (including NO_x, SO_2, O_3, CO, CO_2, hydrocarbons, halocarbons, and organochlorines) (Waugh et al., 2003). As Sable Island is 160 km from Nova Scotia, it is mostly influenced by the ocean. Therefore it is an ideal location for measuring long-term marine emissions as well as continent outflows of smog, vegetation emissions and wildfire smoke (Duderstadt et al., 1998).

Two natural gas projects are located offshore Nova Scotia, both are not far from Sable Island (Figure 2-4) and have been there since 1992. One is the Deep Panuke, Alma, and Thebaud oil and gas (O&G) platforms; the other is the Sable Offshore Energy. Petroleum activities (Cohasset-Panuke Project) was ongoing around Sable Island during 1992-1999 operated by Pan Canadian (now Encana) and Lasmo. After that, the Deep Panuke Offshore Gas Development Project (Deep Panuke in Figure 2-5) was brought on-line on July 22nd, 2013 by Encana Corporation. The Sable Offshore Energy Project (the Thebaud, Alma, North Triumph and Venture complex in Figure 2-5) began in 1999 operated by Exxon Mobil and partners (Hayes, 2014).

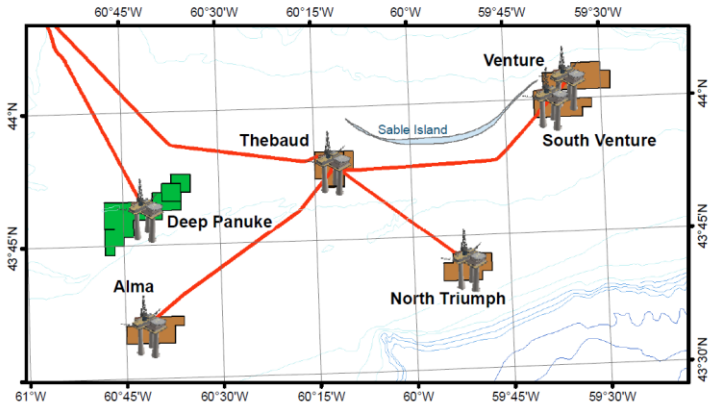

Figure 2-5. Offshore oil and gas activities near Sable Island (Canada NS offshore Petroleum Board, 2013).

2.3.2 Access to Sable Island

There are three ways to reach Sable Island: by helicopter, by vessel and by small plane. Private helicopter operators are not accessible to Sable Island, so helicopters are used at the discretion of the Canadian Coast Guard (CCG) and are subject to operational requirements. A round trip to Sable Island by helicopter costs $12,000 (Gerry Forbes, personal communication, February 1, 2016). Adventure Canada provides two trips to

Sable Island in June with the cost between $3,444 and $15,000 per person, depending on the cabin. It takes about 16 hours to get there from Eastern Passage ("Adventure Canada | Sable Island," 2017). The preferred method of traveling to Sable Island is by small plane (Barnett, 2016). The cost of a round trip to Sable Island by the plane is about $5,500 (Barnett, 2016). The first and last time I traveled to Sable Island was aboard the Britten-Norman Islander aircraft (Figure 2-6), operated by Ted and Debbie Brekelmans for Maritime Air Charter Limited/Sable Aviation.

Figure 2-6. Britten-Norman Islander aircraft operated by Maritime Air Charter Limited for transportation to Sable Island ("Sable Aviation - Aircraft Charter to Sable Island," 2017).

The island was visited every two months between May and December, to calibrate and maintain instruments, and to conduct instrument programming and data gathering. Environment and Climate Change Canada (ECCC) personnel stationed on Sable Island, also assists with downloading data from instruments every two weeks and trouble-shooting when needed.

2.4 Source Apportionment

2.4.1 Potential sources around Sable Island

Industrial areas along the northeast (NE) coast in the US such as Pennsylvania, New York, and port areas are known to have many fossil fuel power stations, which indicates a source for long-range transport (LRT), were determined by Dr. Jeong and Dr. Gibson in 2011 and 2013 as potential PM source regions for Halifax (Gibson et al., 2013; Jeong et al., 2011). 40% of particulate matter around Halifax are secondary sulfate and nitrate coming from trans-boundary emissions from Pennsylvania and New York (Figure 2-7). Second significant source is sea salt, accounting for 18% of PM (Gibson et al., 2013; Jeong et al., 2011).

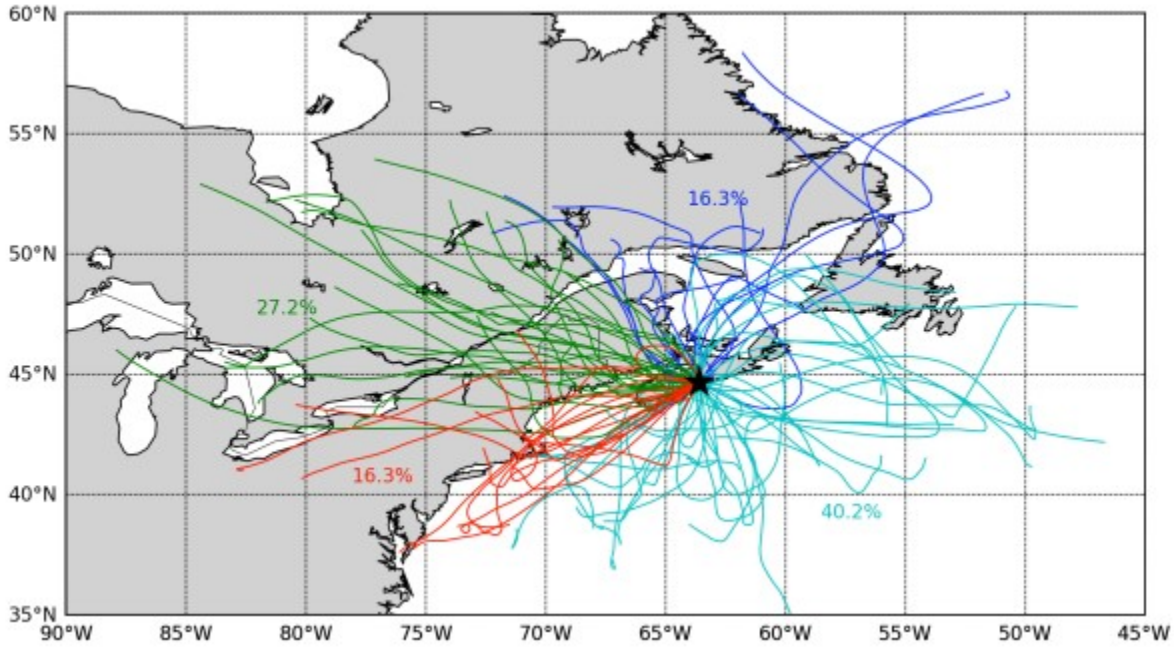

Figure 2-7. Map of HYSPLIT 2-day air mass back trajectories from a source identification study in Halifax in 2011 (Gibson et al., 2013).

From the Figure 2-7, it can be seen that 40.2% of air flow (light blue) over a typical year comes from the marine environment, with typical few anthropogenic sources; 16.3%

(red air mass back trajectories) originate from the NE US and pass over regions of high anthropogenic emissions. Airflow from the NE US is typically laden with secondary ammonium sulphate and ammonium nitrate, which can make up 30-90% of PM mass (Gibson et al., 2013, 2015; Jeong et al., 2011). Another 16.3% (indigo blue air mass back trajectories) originate from the North area, which has few anthropogenic activities. However, most of them would pass over Gulf of St. Lawrence, the Labrador Sea or Northumberland Strait (the strait between NS and Prince Edward Island (PEI)), which can bring VOC from phytoplankton if it is during phytoplankton bloom season. 27.2% pass over Windsor-Quebec corridor, which also has high anthropogenic emissions and industrial emissions, is a major source region of secondary inorganic gases and organic matters (Gibson et al., 2013; Jeong et al., 2011).

There are also offshore oil and gas fields near Sable Island, which can be related to emissions of greenhouse gases (GHGs, CO_2, and CH_4), O_3 inducers (e.g. N_2O, NO_x and VOCs), and climate-relevant substances (e.g. PM, BC and SO_4) (Beusse et al., 2013; Compounds, Devices, Sources, & Sources, 2007; Hansen et al., 2011). Combustion, flaring, vented and fugitive sources are the major potential sources from petroleum activities. Combustion processes are commonly seen in engines, heaters, incinerators, and turbines; flaring is a source for combustion too. Flaring happens when there are excess gases that accumulate in the tops of tanks or unused from processes. Efficient flaring will only produce methane (CH_4) and carbon dioxide (CO_2) (Kearns et al., 2000). Potential gases like NO_x, CO, VOCs, and CH_4 can be emitted from combustion processes. Vented process is the release of gases to balance the pressure during flaring processes (Beusse et al., 2013; Kearns et al., 2000), which occurs in pneumatic devices, dehydration processes, gas

sweetening processes, chemical injection pumps, compressors, tanks, and well testing, completions, and workovers. Fugitive sources exist in leaks and evaporations such as valve and connector leaks, or tank evaporations (Beusse et al., 2013).

There were three air quality instruments deploying during the study on Sable Island: TSI 3321 Aerodynamic Particle Sizer model (APS), TSI DustTrak DRX Aerosol Monitor model 8533, and TSI 3031 Ultrafine Particle Monitor model (UFPM). The APS measures $PM_{0.5\text{-}20}$ number concentration, DustTrak gives $PM_{1/2.5/4/10/TSP}$ mass concentration and UFPM is UFP number counter. In this study, UFP measured by UFPM are in the range from 20 to 800 nm, it can give most information needed for gas-to-particle conversiont study; however, for smaller UFP with size smaller than 20 nm, Fast Mobility Particle Sizer Spectrometer 3091 is another option. It can measure PM in the range from 5.6 to 560 nm with 32 channels of resolution. It can also provide visualize the particle size distribution with a resolution of one second (TSI Incorporated, 2015).

2.4.2 Air Mass Back Trajectory Modelling

Air mass back trajectory modelling has an extensive heritage, and has been used widely in air quality studies (Gibson et al., 2009, 2013; Hondula et al., 2010). When using trajectory-based methods, researchers estimate the paths air parcels take before termination at a receptor, e.g. Halifax. The trajectory origin and path can help identify upwind source regions of air pollutants (Stohl, 2002). During air mass back-trajectory modelling, an approximate three-dimensional air mass moving path is typically estimated from previous wind field and pressure data. There are some shortcomings of air mass back trajectory modelling. Firstly, an accurate trajectory depends strongly on the resolution of the meteorological data and computational methods (Stohl, Haimberger,

Scheele, & Wernli, 2001); secondly, 20% of travel distance may shift due to trajectory computation errors and wind field analysis (Stohl, 2002). However, apart from these shortcomings, air mass back trajectory modelling is still good way of examining atmospheric flow patterns and identifying upwind source regions of air pollution.

The HYbrid Single Particle Lagrangian Integrated Trajectory Model (HYSPLIT) is used to compute air mass back trajectory in this study. It is a computer model designed for computing simple air mass trajectories and simulation of complicated air parcel group transport, dispersion, chemical interaction, and deposition. HYSPLIT was developed by National Oceanic and Atmospheric Administration (NOAA) and Australia's Bureau of Meteorology. It has been widely applied in atmospheric fields; e.g. it has been used to investigate source regions of $PM_{2.5}$ in Halifax area, NS during summer of 2011 (Gibson et al., 2013); Rosselli et al. also used HYSPLIT to reconstruct the wind flow to explore airborne dust-carried microbial contamination in the Mediterranean area (Rosselli et al., 2015).

2.4.3 Positive Matrix Factorization

Positive Matrix Factorization (PMF) is a mathematical receptor model and has been used for source apportionment of PM for over a decade. It can also be used to analyze environmental data such as surface water, ambient air, indoor air and precipitation (Comero, Capitani, & Gawlik, 2009; Gibson et al., 2015). Paterson et al. (1999) used PMF to apportion air pollutant sources at various sites around the southern end of Lake Michigan in 1997 (Ramadan, Song, & Hopke, 2000).

The fundamental principle of receptor model is that mass conservation can be assumed, and a mass balance equation can be achieved to identify and apportion sources

of airborne particulate matter (Kim & Lee, 2005). The approach of this is to gather a large number of elemental concentrations of air sample components. A mass balance equation can be used to represent all *m* chemical species in *n* samples as contributions from *p* independent sources:

$$x_{ij} = \sum_{k=1}^{p} f_{ik} g_{kj} \quad (1)$$

where x_{ij} is the i^{th} elemental concentration measured in the j^{th} sample, f_{ik} is the gravimetric concentration (ng/mg) of the i^{th} element in material from the k^{th} source, and g_{kj} is the airborne mass concentration (mg/m^3) of material from the k^{th} source contributing to the j^{th} sample.

PMF is a multivariate factor analysis tool to divide a matrix of sample data into two matrices: factor contributions (F) and factor profiles (G). Factor contributions and profiles will be used by users to interpret and determine the potential sources for the samples via known source profile information (Norris, Duvall, Brown, & Bai, 2014). PMF uses both sample concentration and user-provided uncertainty (uncertainty = 0.2 for this study) associated with the sample data to weigh individual points. PMF relies greatly on the knowledge of chemical tracers determined from the PM chemical composition to identify the sources of each component factor. The factor analysis model can be written as:

$$X = GF+E \quad (2)$$

Where G is a n by p matrix of source chemical compositions and F is a p by m matrix of source contributions to the samples. Each sample is observed along the time series.

Data for PMF is required to be chosen cautiously which means the data should be representative and meaningful, and that the error estimation and adjustment for the missing data can be reliable (Ramadan et al., 2000). The error estimates for each observed data point were weighted point by point, and the essence of PMF is as follows:

$$\min_{G,F} Q(X, \sigma, G, F) \tag{3}$$

where

$$Q = \left\| \frac{(X - GF)}{\sigma} \right\|_{F,G}^2 = \sum_i \sum_j \left(\frac{e_{ij}}{\sigma_{ij}} \right)^2 \tag{4}$$

$$e_{ij} = x_{ij} - \sum_{k=1}^{p} g_{ik} f_{kj} \tag{5}$$

A critical step in PMF model analysis is to determine the number of factors. Q is a critical parameter for PMF, as defined in Equation (4) (Norris et al., 2014; Ramadan et al., 2000). It can be used to help determine the optimal number of factors with the two version of Q, Q(robust) and Q(True). Q(True) is calculated to describe the goodness of fit for all points, Q(robust) is calculated to describe the goodness of fit for points not fit by the model. Reasonable error estimation for each data point are assumed to be available, then Q should be theoretically equal to the number of data points in the data set (Ramadan et al., 2000). However, there are often missing and abnormal data points in the dataset, so it is reasonable that Q value deviates from the theoretical value (Ramadan et al., 2000). Moreover the optimal run out of all the running results was the one with lowest Q(Robust) value along the path (Ramadan et al., 2000).

CHAPTER 3. Materials and Methods

3.1 Sable Island Experimental Facility

The air chemistry shed was set up on Sable Island to place instruments for this study. It locates on the west side of Sable Island Main Station, besides the Parks Canada and ECCC buildings (upwind of diesel generators and other emissions from anthropogenic activities). Airborne particulate matter mass and size-resolved particle number concentration instruments were used continuously for this study. The inlets of air samplers were installed on the roof of the shed, about two meters above the ground (shown in Figure 3-1). The left one in the figure is the inlet for TSI 3321 Aerodynamic Particle Sizer model (APS), the middle one is for TSI 3031 Ultrafine Particle Monitor model (UFP), and the right one is a Thermo 5012 MAAP black carbon instrument. All three instruments measured airborne PM concentration at a resolution of 15 minutes, which is adequate considering gas-to-particle conversion normally takes hours to happen.

Figure 3-1. Sampling equipment on the roof.

3.1.1 TSI Aerodynamic Particle Sizer model 3321

One TSI APS (shown in Figure 3-2) is used for measuring real-time dynamic aerosol number concentrations. The range of the measurement is 0.5 - 20μm over 52 channels. A flow rate of 5L/min was used via an internal pump, a laser was used as the light scattering and an avalanche photodetector (APD) as the sensor (TSI Incorporated, 2012a). The APS was set to export sample data in .txt format automatically at 15-minute intervals. The APS along with its sampling inlet was installed in the Sable Island Air Chemistry shed on Wednesday, September 30. The inlet was levelled and secured on the roof of the Air Chemistry shed by a tripod, stainless steel mounting brackets were used to hold the feet of the tripod. A 1.25-inch diameter hole was drilled through the roof and ceiling of the shed to accommodate a candy cane inlet for the APS. The indoor end of the inlet was connected to APS with anti-static tubing from TSI. A weatherproof rubber flashing was installed around the inlet at the roof opening and sealed with a weatherproof roofing tar to prevent water ingress into the shed. Typical household window bug screen was strapped to the inlet entrance to keep bugs, sand, and other debris from entering the equipment.

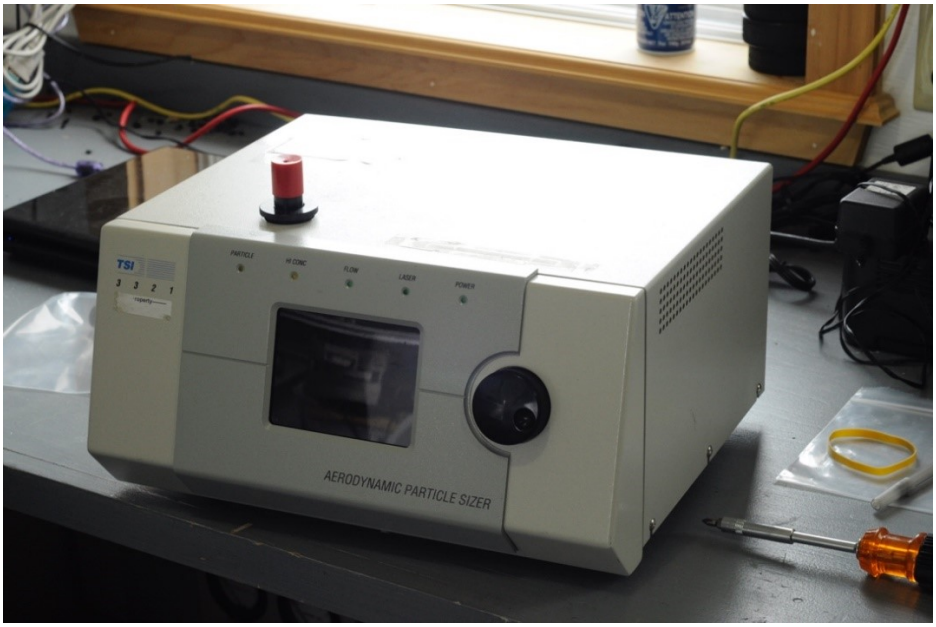

Figure 3-2. TSI aerodynamic particle sizer (APS) model 3321.

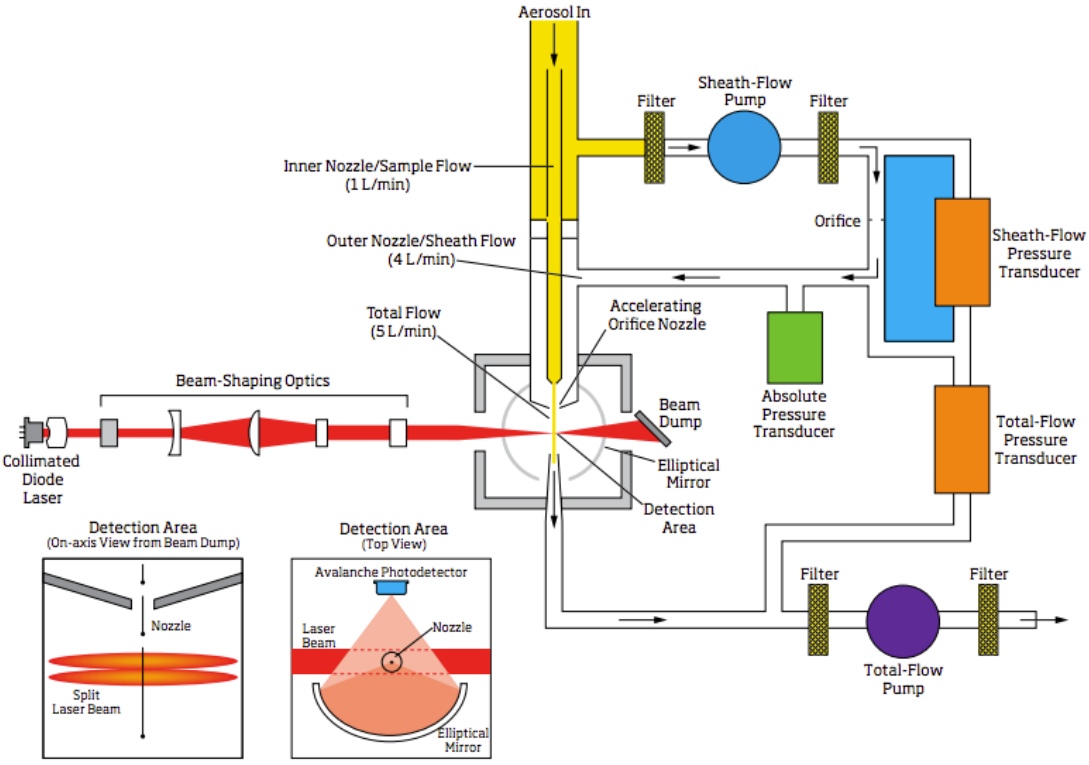

Figure 3-3. Flow Schematic of APS.

As illustrated above in Figure 3-3, the APS firstly accelerates the aerosol sample flow through an accelerating hole, also known as a critical orifice. The larger particle is accelerated more slowly as it has larger inertia. After particles exit the nozzle, they enter detection area and cross two split laser beams. The laser beam is emitted by a collimated diode laser and reflected by a beam dump, so there are two overlapping laser beams. The light will be scattered when each particle crosses through laser beams and will be collected by an elliptical mirror. The mirror is placed 90 degrees to the laser beam; the scattered light will be focused onto an avalanche photodetector (APD). The APD then converts the light signal into electrical signal. Each particle will give a single signal with two crests due to the overlapping laser beams. Moreover, the time-of-flight (mostly within four nanoseconds) between two peaks will be measured to determine the aerodynamic size of the particle. For the smallest particle (< 0.523 μm), only one crest will be detected due to its small size and high velocity (TSI Incorporated, 2012a).

3.1.2 TSI DustTrak DRX Aerosol Monitor model 8533

The TSI DustTrak DRX Aerosol Monitor model 8533 shown below in Figure 3-4 is a desktop instrument for measuring particle mass concentration. It measured real-time particulate matter mass concentration in the size fractions of PM_1, $PM_{2.5}$, PM_4, PM_{10} μm and total suspended particles (TSP). TSP is particles smaller than 60 μm. The DRX operated at a flow rate of 3L/min. The concentration detection range is between 0.001-150 mg/m^3, the range of particle size detection is 0.1-15μm (TSI Incorporated, 2012b). Aerosol data can be downloaded by inserting a USB device into the DRX. The data was downloaded every Thursday by ECCC, the flow rate should be checked and the DRX

should be calibrated before resuming measuring. The DRX was shut down and brought back to the lab in February due to unsolved errors.

Figure 3-4. TSI DustTrak DRX Aerosol Monitor model 8533 (Photo Courtesy of Codey Barnett).

The theory of operation scheme is shown in Figure 3-5 below. The aerosol is absorbed through the aerosol inlet and go into two directions continuously by an internal diaphragm pump. Some are split to pass through a HEPA filter before going into the sensing chamber, the rest aerosols. Then the particle will interact with a laser beam emitted from a laser diode. The light first passes through a collimating lens and then a cylindrical lens to give a thin sheet of laser light. The light scattered from particles will be collected by a gold-coated mirror and then focused onto a photodetector, which will cause a voltage difference in photodetector and form photodiode signal (TSI Incorporated, 2012b).

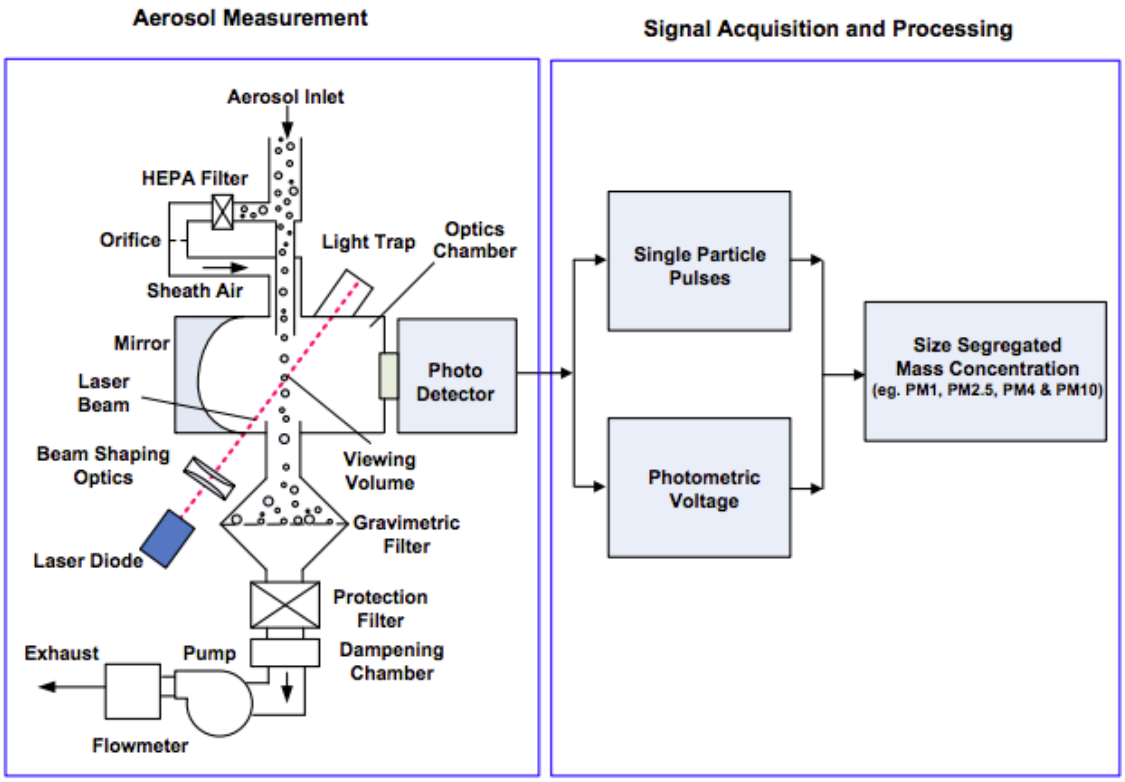

Figure 3-5. Flow Schematic of DustTrak.

3.1.3 TSI Ultrafine Particle Monitor model 3031

The TSI UFP model (shown in Figure 3-6) (UFPM) was used for collecting real-time aerosol size-distribution and number concentration data (TSI Incorporated, 2012b). It is designed for aerosols with a median aerodynamic diameter between 20 nm to 800 nm. The operation time was set to 15-min intervals continuously. The UFPM on Sable Island was equipped with TSI 3031200 Environmental Sampling System (ESS) (shown in Figure 3-7) that included a PM_{10} size-selective inlet, PM_1 sharp cut cyclone, flow splitter, Nafion dryer, and particle filter (Monitoring, 2014). A flow rate of 16.67 L/min was achieved using the internal vacuum pump from UFPM 3031 and an external vacuum pump to the left of UFPM for model 3031200 sampling system.

Figure 3-6. TSI UFP model 3031 front face.

Figure 3-7. TSI 3031200 Environmental Sampling System.

The operation schema is shown in Figure 3-8, steps are (A). To charge the particles (in Corona-Jet charger), (B). To classify them by sizes (in Differential Mobility Analyzer, short for “DMA”) and (C). To quantify the concentrations (Hillemann,

Zschoppe, & Caldow, 2007). The aerosols were drawn through the roof-top inlet into the device on Sable Island. Inside the device, the aerosols firstly enter an equalization tank to mix up and smooth out the fluctuations. Then the aerosol flow will be separated into a 1L/min ion jet flow and a 4L/min aerosol flow. The 1L/min flow will be going through a carbon filter, HEPA filter and an ionizer; the aerosol flow will be going into a mixing chamber to mix with ions delivered by the filtered clean air.

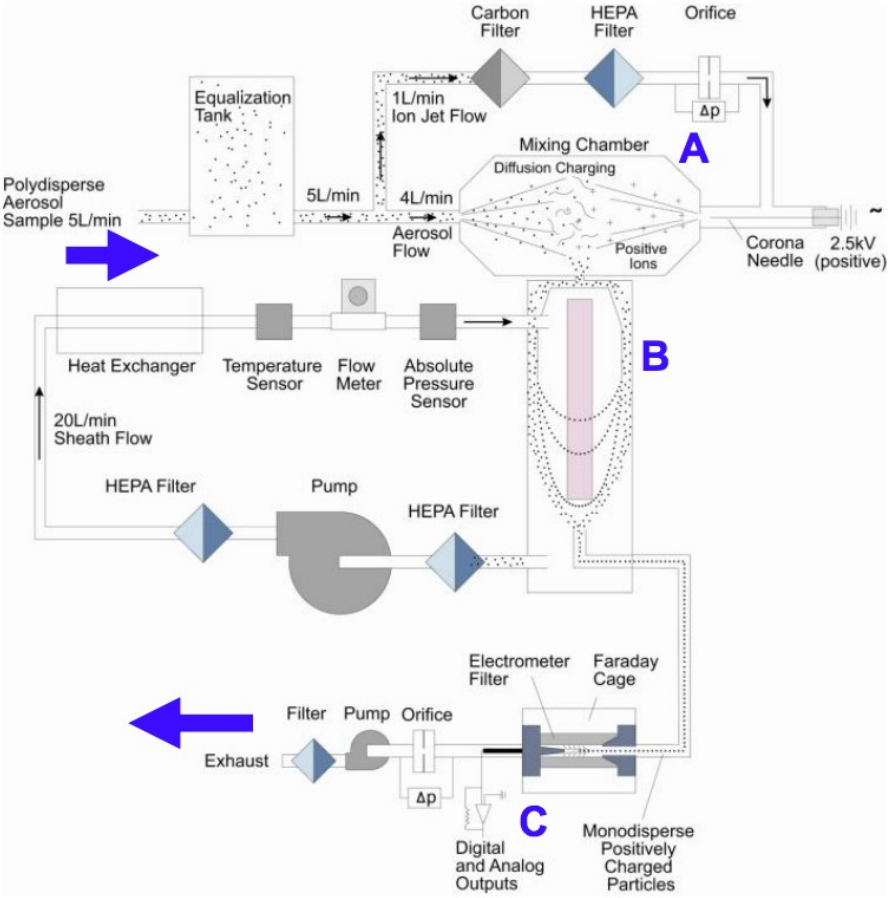

Figure 3-8. Schematic of UFP model 3031.

After going through the mixing chamber, the aerosols become charged and move to DMA for size classification. The DMA is a metal cylinder with a high-voltage metal cylindrical rod attached in the center (as shown in Figure 3-9). The aerosols enter from

the top of DMA column and flow down, which is maintained at a controlled negative voltage to collect aerosols (shown as orange part in Figure 3-9). The outer cylinder is electrically grounded so an electric field will be created in the space and attracting positively charged particles to the collector rod. The location that particles will be precipitating along collector rod is determined by the particle electrical mobility, the DMA flow rate, and the DMA inside the structure. Particles within a narrow range of electrical mobility exit along the monodisperse air flow through a slit at the end of collector rod. They will be transferred to electrometer to determine particle concentration (TSI Incorporated, 2012b).

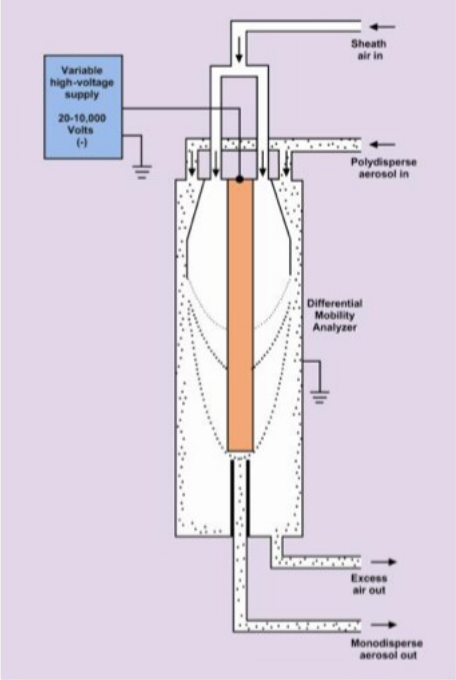

Figure 3-9. Operation principle of the DMA Flow.

3.2 Meteorological data

There are two weather stations on Sable Island; for this study the meteorological data was obtained from the station (ID: 8204703) located 100 meters from the air chemistry shed with an elevation of 1.2 meters. It was chosen because it provides wind speed, wind direction and weather condition while the other only gives temperature. The meteorological data used in this study was retrieved from the Government of Canada climate website (http://climate.weather.gc.ca/) and used as a supplement when apportioning sources of PM.

3.3 Statistical Analysis and Graphing

The data collected from instruments was organized into spreadsheets in Microsoft Excel based on sampling dates. Firstly, data was cleaned by removing null data and unexpected extreme values, as well as data measured in calibration and malfunction days. As most PM data was measured at an interval of 15 minutes, so it was necessary to generate hourly, diel and daily averages data for better understanding. Descriptive statics of annual $PM_{1/2.5/4/10}$, total mass concentrations and UFPs were then generated in RStudio or Excel; annual time series were also generated in Excel for annual capturing spikes or trends. Seasonal time series were also plotted to see the difference between seasons. HYSPLIT and the NASA Terra MODIS, Aqua MODIS, and VIIRS satellites were used to investigate potential source regions for spikes observed in the plots. In this study, seasons were divided in the following way: Spring: April, May, and June; Summer: July, August and September; Fall: October, November and December; Winter: January, February and March.

Principle component analysis (PCA) was also used in this study for addressing the possible variables. PCA is one of the factor analysis methods used to reveal the hidden source information from a large ambient measurement. It can simplify the complicated, highly dimensional dataset to a lower dimension. The PCA algorithm usually performs an eigenvector analysis of a correlation matrix (Seinfeld & Pandis, 2016).

3.4 Visible Satellite images

Satellite images for phytoplankton growth are based on environmental data provided by National Aeronautics and Space Administration (NASA) Ocean Color Web database (http://oceancolor.gsfc.nasa.gov/cgi/browse.pl?sen=am) in this study. The NASA Ocean Color Web database is based on data record taken by Visible Infrared Imaging Radiometer Suite (VIIRS) on board the Suomi NPP satellite and Moderate Resolution Imaging Spectroradiometer (MODIS) on board the Terra and Aqua satellites. MODIS satellites observe every point on Earth's surface every 24-48 hours. The instruments can capture cloud cover status, distribution, and size of cloud droplet, aerosol properties, terrestrial and marine biomass activities (e.g. phytoplankton which live in the upper ocean layer). MODIS satellites also measure chlorophyll fluorescence, which can help with monitoring phytoplankton growth ("MODIS Web", 2017; Tassia Owen, 2017). VIIRS satellite is a successor of MODIS satellites, it is a scanning radiometer which has the similar capability as MODIS instruments, but it provides much better spatial resolution ("Visible Infrared Imaging Radiometer Suite (VIIRS)", 2017).

Chlorophyll-a concentration satellite images used in this study were generated from two data systems: the NASA Giovanni data analysis system (https://giovanni.gsfc.nasa.gov/giovanni/) and State of the Oceans (SOTO;

https://podaac-tools.jpl.nasa.gov/soto). Giovanni is an acronym for Goddard Earth Sciences Data and Information Services Center (GES DISC) Interactive Online Visualization and Analysis Infrastructure, it allows researchers to explore and analyze observational data from NASA Earth observation satellites. Current Giovanni uses the Grid Analysis and Display System (GrADS) as fundamental analytical function (Acker & Leptoukh, 2007). Researchers have access to various environmental data visualizations displayed via the plotting of environmental parameters (e.g. rainfall, chlorophyll-a concentration, humidity, temperature, etc.) from several satellite instruments (MSFC, 2009). SOTO is a suite of web-based tools that aid in generating maps and plots that promotes the analysis of the ocean status. It provides access to various ocean satellite-related products such as sea surface temperature and chlorophyll-a concentration, the commonly used proxy for phytoplankton abundance.

For this study, chlorophyll-a monthly mean concentration and maps in the regions of interest were generated in Giovanni. The bounds of regions of interest were determined by air mass back trajectory modelling. Monthly phytoplankton abundance (in the form of *chl a* concentration) was inserted into Google Maps as a layer; HYSPLIT air mass back trajectories were also inserted as a layer on top of *chl a*, thus providing a powerful spatiotemporal visualization of how the modelled air masses may be influenced by passage over biologically active ocean regions. One caveat of this approach is in the temporal mismatch of the 5-day air mass back trajectory and the monthly average *chl a* fields. It is intended, therefore, to be a qualitative, rather than quantitative tool, which allows reasonable hypotheses to be formed on how biogenic emissions may contribute to UFP formation at the Sable Island study site.

In the source apportionment analysis, *chl a* concentration maps on peak days were retreived from the SOTO website. To visualize each daily concentration, daily files were read for last the five days, coincidence pixels of the five days were then averaged, scale and offset were applied linearly from 0.01 to 10 mg/m^3 according to color table, finally global daily phytoplankton abundance would be visualized (NASA Ocean Biology Processing Group, 2015). Sable Island was found in the global phytoplankton abundance map and zoomed in till the region of interest was obtained for more details. These tools can be used to investigate the hypothesis that marine biogenic processes contribute to the formation of UFP and fine PM. Variables mapped on uniform space-time grid scales, usually with some completeness and consistency.

3.5 Air mass back trajectories

The HYSPLIT air mass back trajectory model was accessed via the NOAA web archive (https://ready.arl.noaa.gov/hypub-bin/trajasrc.pl) (Barnett, 2016; Gibson et al., 2013). Five-day normal air mass back trajectories for the Sable Island were generated using the online HYSPLIT archive data. Two back trajectories were obtained for each 24h sampling period (00:00 UTC and 12:00 UTC) to avoid dramatic changes in potential upwind source regions. The air mass arrival height was set to 500 m to reduce the risk of air mass hitting the surface before it arrived at Sable Island.

HYSPLIT air mass back trajectory placemark files (.kmz file) were also generated and used in Google Earth for more detailed information. Timestamps of air mass in last five days were investigated to find potential VOC/marine biogenic organic gases sources that may cause PM spike on Sable Island.

3.6 Positive Matrix Factorization

The US EPA PMF receptor model v5.0.14.21735 was used for source apportionment of PM sampled on Sable Island in 2016. Certain steps should be completed to utilize Base Model in PMF. In Figure 3-10, the order of operations was shown and it was based on how functions are processed in the program (from left to right) (Norris et al., 2014). The model was run using a dataset that consisted of annual daily average $PM_{1/2.5/4/10}$ and UFP number concentrations with temporal resolution of 15 minutes. In order to run, it requires both a species concentration file and species uncertainty file related to the dataset. A concentration file containing daily averages was generated in RStudio and quality controlled for input into the model. For this study, PM source chemical markers information was obtained from Gibson et al (Barnett, 2016; Gibson et al., 2013, 2015; Jabre, 2017). The model will not run if null, or 0 values are present, so all null and 0 values are replaced with a value of -999 to allow the model to run without errors. After concentration files being loaded with successfully into the program, missing value was set to be replaced with species median. After that, the number of the Basic Model runs was set to 20 and the number of factors was set to 4. After the Base Model Runs were executed, the Base Model analysis was run 20 times which gave 20 plots and timeseries for each factor. Among the 20 Basic Model Results, the run with the lowest Q(robust) value was identified as the optimal run (Ramadan et al., 2000). Then fpeak modelling with bootstrapping was performed on Base Run #20 with Fpeak Runs = 0.5, Bootstraps # = 100, minimum $R^2 = 0.6$ and block size = 9.

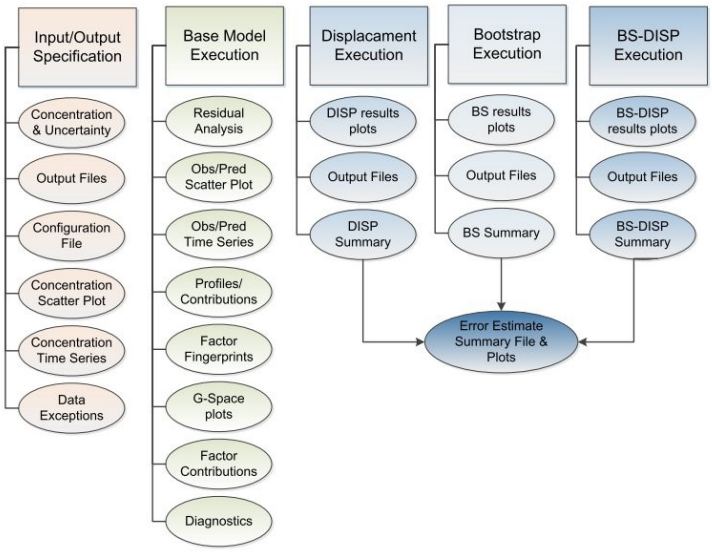

Figure 3-10. Flowchart of PMF base model operation (Norris et al., 2014).

3.7 Instruments malfunction

Table 3-1 summarizes the dates and reasons that instrument malfunctioned in 2016.

Table 3-1. List of Instrument malfunction in 2016

Instrument	Date	Reason
DRX	Apr. 23th – 28th, 2016	Malfunctioning
APS	Jan. 7th - 24th, 2016	Unexpectedly stopped working
	Aug. – Dec. 16th, 2016	Out for service
UFP	Aug 8th – Sep, 2016	Out for service

It can be seen in Table 3-1, DRX Aerosol monitor model 8533 stopped working from due to rain water leaking into instrument through water trap April 23th to April 28th, 2016. APS model 3321 was stopped working unexpectedly on January 7th -24th, 2016; it was sent out for service from August to December. UFP monitor model 3031 was sent

out for service in August. Outage of some instruments do have influence on results. For UFP monitor, the outage in August seems to be significant. Due to the outage, the average of UFP concentration in August was not able to be used for comparison with total VOC trends.

CHAPTER 4. Results and Discussion

Descriptive statistics of all the PM measurements conducted on Sable Island from January 1st, 2016 to December 31st, 2016 was shown. Comprehensive year-long daily, monthly, and seasonal plots, comparison, and correlation plots were also displayed. All daily plots were generated from daily data calculated based on an average of 15-interval measurement.

All measurements taken from Sable Island in 2016 were in UTC, only meteorological data was used in local time, time zone difference can be seen in Figure 4-1. Seasons were defined as follows: Spring: April, May, and June; Summer: July, August and September; Fall: October, November and December; Winter: January, February and March.

Figure 4-1. UTC and local time converter regarding daylight saving time in 2016.

4.1 Descriptive Statistics

4.1.1 Meteorological Condition

The 2016 meteorological data was obtained from the Meteorological Services Canada weather station (ID: 8204703) on Sable Island (Table **4-1**). Data was collected continuously at a temporal resolution of every hour.

Table 4-1. Meteorological data descriptive statistics

Variables	Wind Speed *[km/hr]*	Wind Direction *[°]*	Temperature *[°C]*
n	8535	8441	8346
n missing	249	343	436
Completeness	97.1%	96.1%	95.79%
Min	0	10.0	-9.70
25th Percentile	17.87	140.0	3.80
Median	23.69	220.0	9.30
Mean	**25.34**	**205.8**	**9.21**
75th Percentile	34.00	280.0	15.10
Max	91.00	360.0	23.9
IQR	17.00	14.0	11.30
Standard Deviation	12.79	9.7	6.90

From Table 4-1, it can be seen that the data completeness for temperature, wind direction, and wind speed were 97.1%, 96.1%, and 95.79%, respectively. The mean (min:max *units*) temperature was 9.43±7.36 (-9.70:53.8 *°C*), which is 3 °C warmer than Halifax's 6.49 (-9.1:22.1 *°C*) (Government of Canada, 2016). The maximum temperature of 53.8 °C was due to annual station maintenance in August. The mean wind speed was 25.34 (0:91 *km/h*).

Monthly mean wind speed on Sable Island in 2016 was shown in Figure 4-2.

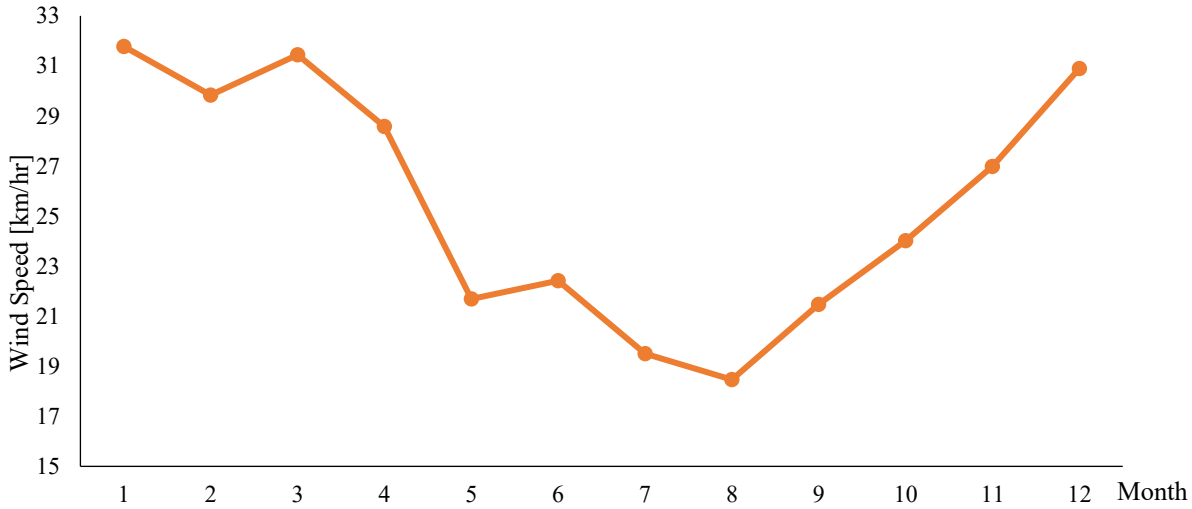

Figure 4-2. Monthly mean wind speed on Sable Island in 2016.

Figure 4-2 shows the monthly mean wind speed in 2016 on Sable Island, winter (January - March) is the windiest season; January is the windiest month of the year (31.78 *km/hr*), with March coming in second place (31.44 *km/hr*). Summer (July - September) is the least windy season; August is the least windy month of the year (18.46 *km/hr*). Most coarse sea sprays are from wind blowing sea surface, and 20-50 nm UFP coagulates more in a silent condition; therefore windy condition can be one of the reasons for high PM concentration (Jones, Harrison, & Baker, 2010; Yoon et al., 2007) and low UFP concentration (Sioutas et al., 2005; Yoon et al., 2007).

4.1.2 PM Mass Concentration

Mass concentration of particulate matter with a size between 1-10 μm on Sable Island was measured at an interval of 15 minutes continuously by TSI DustTrak DRX model 8533 in 2016. Descriptive stats for $PM_{1/2.5/4/10/TSP}$ was shown in Table 4-2.

Table 4-2. Descriptive Statistics for $PM_{1/2.5/4/10/TSP}$

Variables	PM_1 *[mg/m³]*	$PM_{2.5}$ *[mg/m³]*	PM_4 *[mg/m³]*	PM_{10} *[mg/m³]*	Total *[mg/m³]*
n	32866	32866	32866	32866	32866
n missing	739	739	739	739	739
Completeness	97.75%	97.75%	97.75%	97.75%	97.75%
Min	0	0	0	0	0
25th Percentile	0.005	0.006	0.006	0.006	0.006
Median	0.009	0.009	0.009	0.009	0.010
Mean	**0.011**	**0.012**	**0.011**	**0.012**	**0.012**
75th Percentile	0.014	0.015	0.015	0.015	0.015
Max	0.087	0.093	0.124	0.124	0.127
IQR	0.010	0.010	0.011	0.011	0.011
Standard Deviation	0.009	0.01	0.010	0.010	0.010

From Table 4-2, the data completeness for all PM mass concentrations was 97.75%. The mean (min:max *units*) for $PM_{1/2.5/4/10/TSP}$ is PM_1 = 0.011±0.009 (0:0.087 mg/m^3), $PM_{2.5}$ = 0.012±0.010 (0:0.093 mg/m^3), PM_4 = 0.011±0.010 (0:0.124 mg/m^3), PM_{10} = 0.012±0.010 (0:0.124 mg/m^3) and PM_{TSP} = 0.012±0.010 (0:0.127 mg/m^3).

Figure 20 below shows the annual cycle plot of $PM_{1/2.5/4/10/TSP}$ mass concentration (mg/m^3) at a temporal resolution of 15 minutes. TSP here represents PM with diameters below 60 µm.

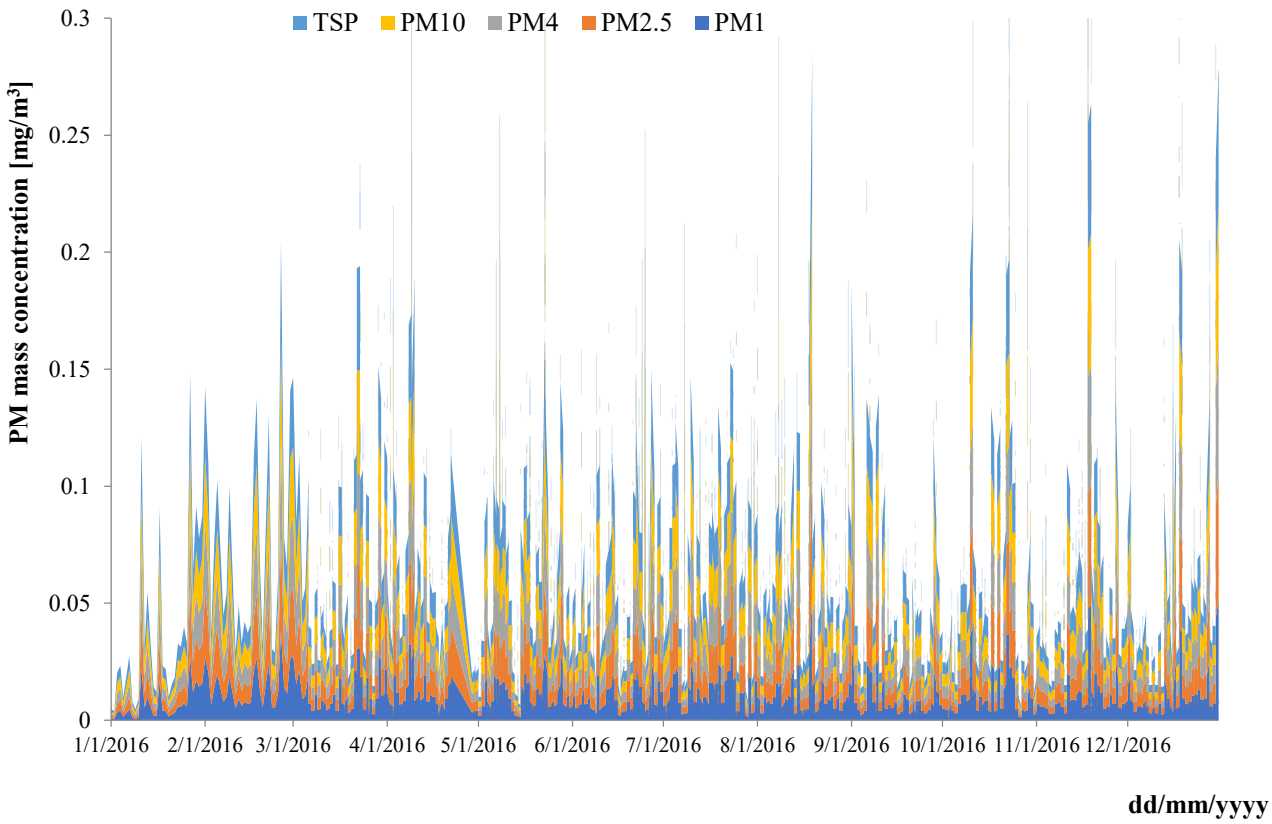

Figure 4-3. Annual cycle of $PM_{1/2.5/4/10/TSP}$ mass concentration (mg/m^3) measured every 15 minutes on Sable Island in 2016.

As can be seen in Figure 4-3, TSP and $PM_{2.5}$ accounts for most of PM mass concentration. TSP has much larger size and therefore mass, $PM_{2.5}$ can last the longest time among PM size fractions. PM mass spike occurred on September 14th, then December 31st came in the second place.

Figure 4-4 below shows the monthly mean $PM_{1/2.5/4/10/TSP}$ mass concentration (mg/m^3) on Sable Island

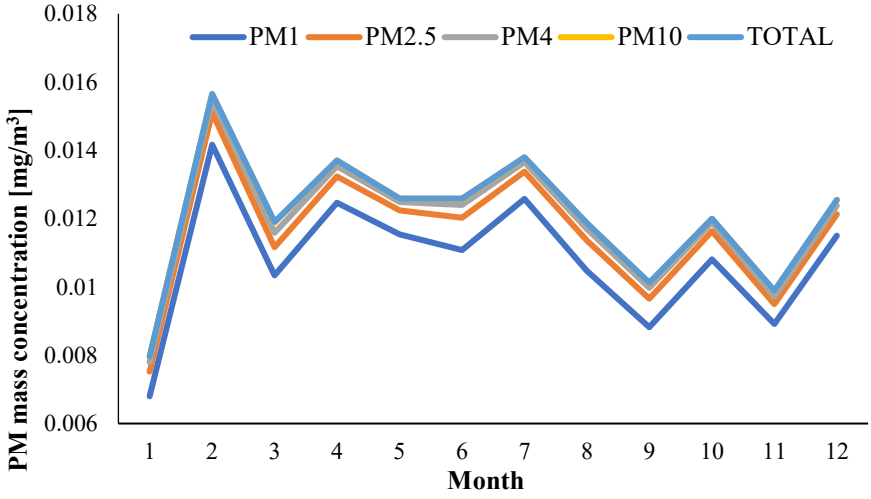

Figure 4-4. Mean monthly $PM_{1/2.5/4/10/TSP}$ mass concentration (mg/m^3) on Sable Island in 2016.

As can be seen in Figure 4-4, February mean concentration reaches the peak value of the year, with July coming in the second place. Mass concentration of each PM sizes were similar to each other due to their small sizes. PM_1 has the least mass concentration due to their small sizes, and TSP has the largest mass concentration all the time which also makes sense. February has the highest mass concentration for all sizes, and July comes in second place.

4.1.3 PM Number Concentration

Number concentration of particulate matter on Sable Island was measured continuously at a temporal resolution of 15 minutes using TSI APS model 3321 in 2016. Particle number concentrations were counted in each of 52 size fractions, also known as channels. For ease of analysis, and data visualization purposes, these 52 size fractions were averaged into the same five size fractions that correspond to PM mass concentration that were measured above by the TSI DRX, i.e. 1, 2.5, 4, 10 and 20 µm. Table 4-3 below shows descriptive statistics number concentration of $PM_{1/2.5/4/10/20}$.

Table 4-3. Descriptive statistics for $PM_{1/2.5/4/10/20}$ number concentration

	PM_1 *[Particle #/cm^3]*	$PM_{2.5}$ *[Particle #/cm^3]*	PM_4 *[Particle #/cm^3]*	PM_{10} *[Particle #/cm^3]*	PM_{20} *[Particle #/cm^3]*
n	35136	35136	35136	35136	35136
n missing	14639	14639	14639	14639	14639
Completeness	58.3%	58.3%	58.3%	58.3%	58.3%
Min.	1879	64	3	1	1
1st Percentile	11480	1565	90	5	1
Median	18360	2578	174	9	1
Mean	**21249**	**2970**	**257**	**20**	**1**
3rd Percentile	27580	3842	323	20	1
Max	79590	20123	3856	491	26
IQR	2932.5	2920.5	2421	486	310
Standard Deviation	19676.6	3496	562	81	3

As been shown in Table 4-3, the data completeness for PM number were 58.3%. The several gaps in annual cycle plot were due to the APS malfunctioning. The first gap occurred on January 7th at 14:45, the instrument was running but stopped recording, it started recoding again on January 24th 00:00. The instrument was removed from the

island in August for repair and was installed again on August 31st but didn't work. The new instrument was not installed until December 16th. The mean (min:max *units*) for $PM_{1/2.5/4/10/20}$ is PM_1 = 21249 ±19677 (1879:79590 *#/cm³*), $PM_{2.5}$ = 20122.8±3496.5 (64.0:20122.8 *#/cm³*), PM_4 = 257.4±562.0 (3.26:3856.33 *#/cm³*), PM_{10} = 19.6±80.8 (1.3:490.8 *#/cm³*) and PM_{20} = 1.5±2.7 (1.0:25.5 *#/cm³*).

Annual cycle analysis (Figure 4-5) investigated the peaks and troughs in the $PM_{1/2.5/4/10/TSP}$ mass concentration to aid in the determination of their sources.

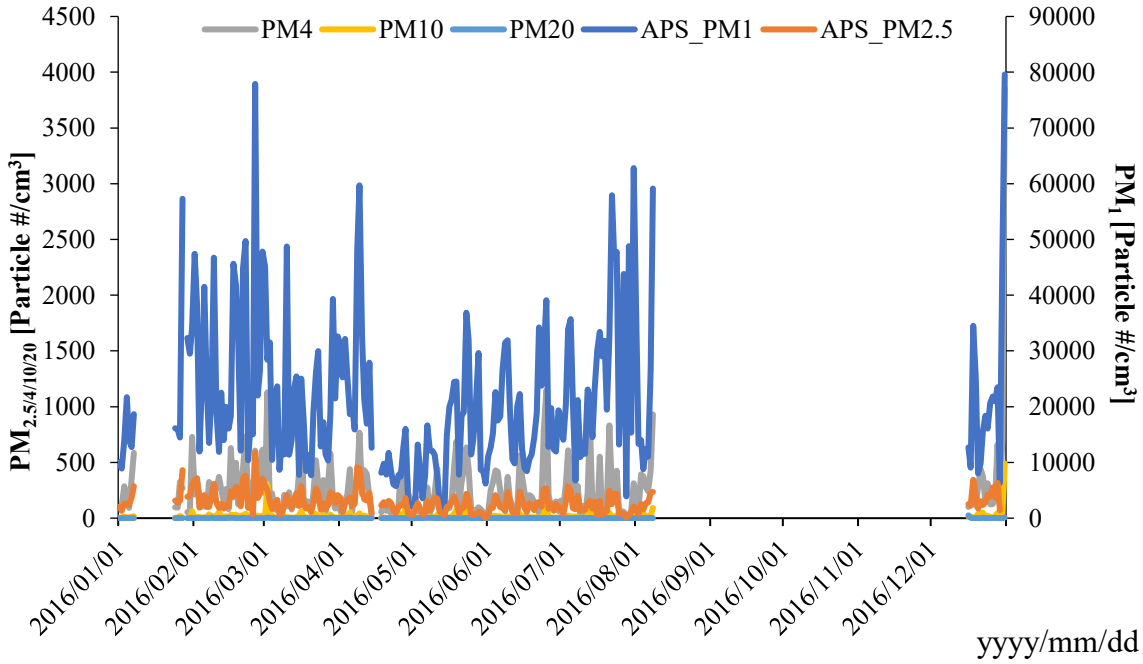

Figure 4-5. $PM_{1/2.5/4/10/20}$ number concentration (particle #/cm³) measured every 15 minutes on Sable Island in 2016.

As can be seen in Figure 4-5, PM_1 accounts for most of number concentration among PM size fractions. It is due to their smaller sizes and easier to move around. PM_{20} has the least number concentration as they are larger and easier to be moved from atmosphere. On December 31st, PM_1 reached the maximum value (79590 /cm³) of the year; then February 26th, it reached the second maximum value (77879 /cm³).

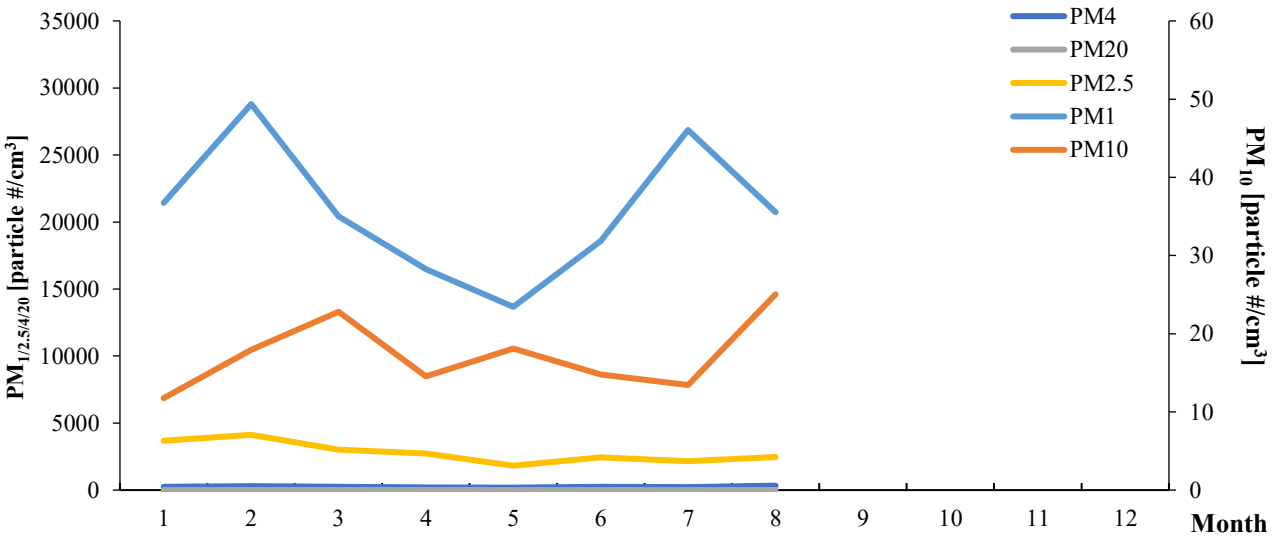

Figure 4-6. Mean monthly $PM_{1/2.5/4/10/20}$ number concentration (particle #/cm^3) on Sable Island in 2016.

From Figure 4-6, it can be observed that PM_1 number concentration (particle #/cm^3) reached maximum monthly mean in February. With July coming in the second place, which is similar to mass concentration trending. Larger amount in February can be due to windy and snowy weather, which was shown in Figure 4-2.

From annual and monthly mean PM number concentrations (Figure 4-3, Figure 4-4, Figure 4-5 & Figure 4-6), peak dates (Jan. 27th, Feb. 26th and Apr. 9th) have been determined and analyzed with HYSPLIT air mass back trajectories and satellite images for source apportionment.

4.1.4 UFP Number Concentration

Number concentrations of UFP on Sable Island was measured continuously at 15-minute intervals via a TSI UFP monitor model 3031 in 2016. Table 4-4 below provides the descriptive statistics from the UFP instrument. The UFP counts particles in 6 size bins ranging from 20 – 800 nm.

Table 4-4. Ultrafine particle descriptive statistics

Variables	20-30 nm *[Particle #/cm^3]*	30-50 nm *[Particle #/cm^3]*	50-70 nm *[Particle #/cm^3]*	70-100 nm *[Particle #/cm^3]*	100-200 nm *[Particle #/cm^3]*	200-800 nm *[Particle #/cm^3]*
n	35136	35136	35136	35136	35136	35136
n missing	2634	2634	2634	2634	2634	2634
Completeness	92.50%	92.50%	92.50%	92.50%	92.50%	92.50%
Min	0	0	0	0	0	0
25th Percentile	34	69	42	42	76	2
Median	185	214	138	129	191	25
Mean	**328**	**360**	**227**	**205**	**252**	**43**
75th Percentile	388	463	308	283	337	59
Max	34766	35441	20213	17333	32469	4261
IQR	354	393	266	241	261	57
Standard Deviation	597	595	339	286	321	66

From Table 4-4, the data completeness for the UFP particles number was 92.50%. The mean (min:max *units*) for UFP in terms of size fractions are (hereafter e.g. UFP 20-30 nm): 20-30 nm = 328 ±597 (0:34766 *#/cm^3*), 30-50 nm = 360±595 (0:35441 *#/cm^3*), 50-70 nm = 227±339 (0:20213 *#/cm^3*), 70-100 nm = 205±286 (0:17333 *#/cm^3*) , 100-200 nm = 252±321 (0:32469 *#/cm^3*) and 200-800 nm = 43±66 (0:4261 *#/cm^3*).

Figure 4-7 below shows the annual cycles of UFP number concentration measured at 15-minute interval. The gap in the plot was due to the UFP instrument being removed from the Island for service.

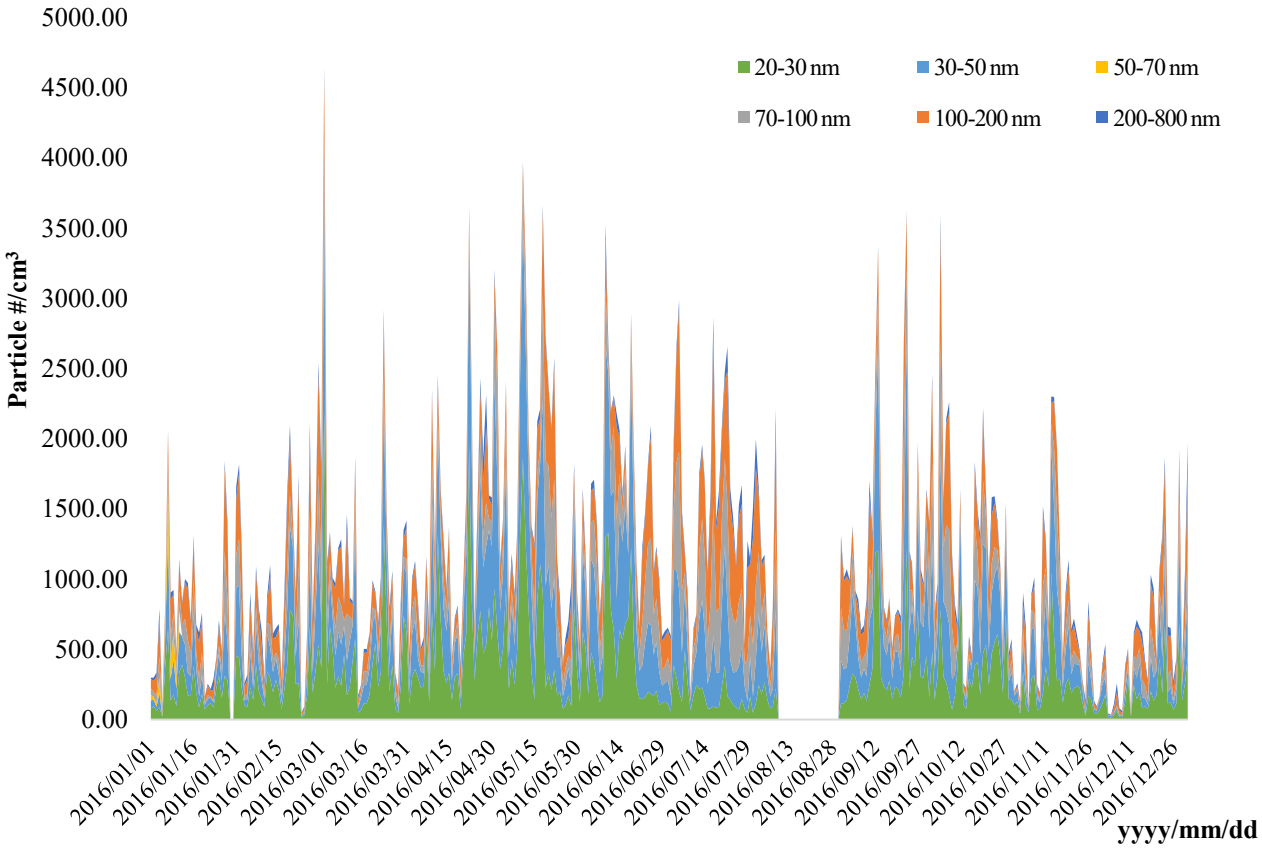

Figure 4-7. Annual cycle of UFP number concentration (particle #/cm^3) on Sable Island in 2016.

It's noticeable from descriptive statistics in Table 4-4 and the annual cycle plot in Figure 4-7 that the 20-30 nm and 30-50 nm size fractions account for most of UFP measurements, whereas 200-800 nm accounts for the least. Also interestingly, the 20-30 nm and 30-50 nm UFP have negative correlation with 100 – 200 nm and 200-800 nm UFP, e.g. 20-50 nm UFP tend to have spikes in May and October, troughs in July, while 100-800 nm UFP tend to have troughs in May and a spike in July; in the meantime, 200-

800 nm size fraction also has a distinct spike in December, which is consistent with a study conducted in East Atlantic coast in Ireland (Yoon et al., 2007). UFP 20-30 nm and UFP 30-50 nm reached their first peak in May and the second peak in October, which was also reported by Barnett (Barnett, 2016). These two peaks correspond with the spring and fall phytoplankton blooms and associated with chlorophyll-a peaks also observed in Craig et al., (2015) (see Chapter 5.1). Monthly mean variance of UFP number counter was shown below in Figure 4-8.

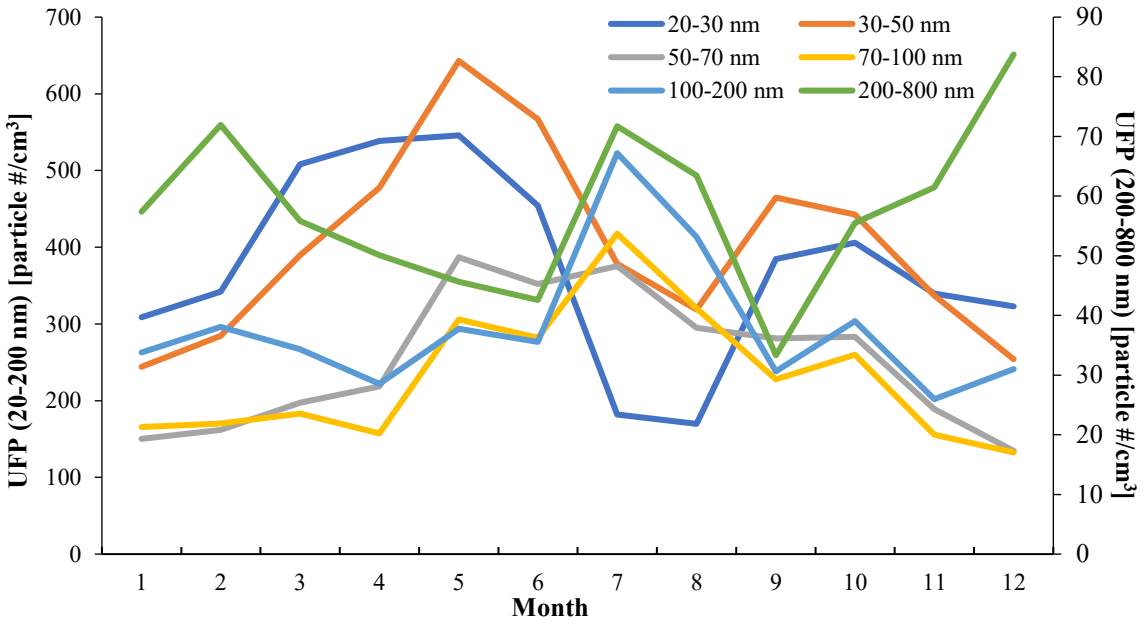

Figure 4-8. Mean monthly UFP number concentration (particle #/cm^3) on Sable Island in 2016.

It can be seen in Figure 4-8, UFP 20-30 nm and 30-50 nm reached their maximum in May and second peak came in October; UFP 50-70 nm reached its maximum in May as well and then began to decrease; UFP 70-100 nm 200-200 nm reached its maximum in July and then began decrease. UFP 200-800 nm reached its maximum in July, and then

began to increase again in October till December it reached another peak, it has three peak through the year: February, July and December.

Closer scrutiny of the two spikes appearing in May and October monthly value is shown in Figure 26 & Figure 27.

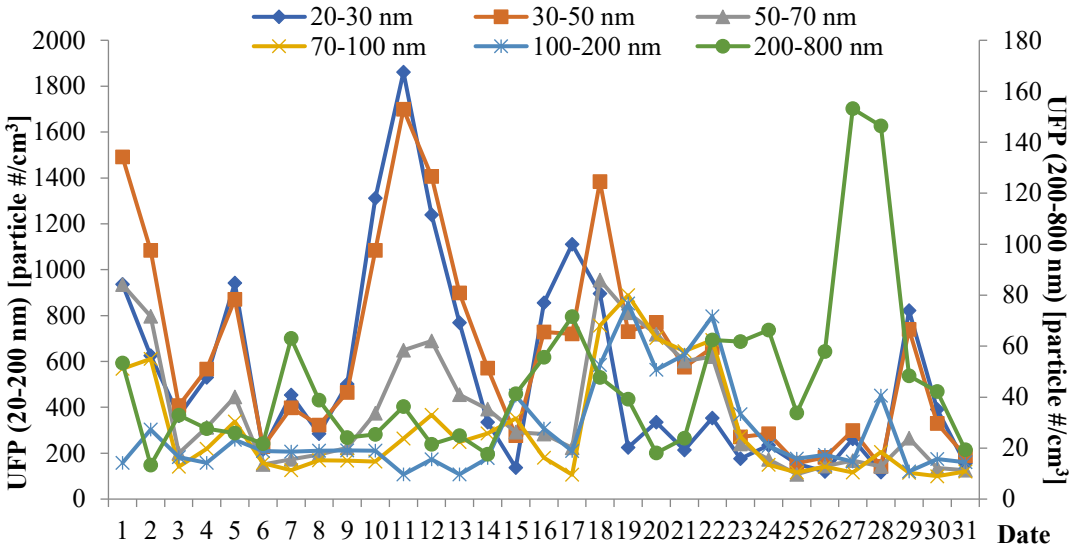

Figure 4-9. Daily mean UFP number concentration (particle #/cm^3) in May 2016.

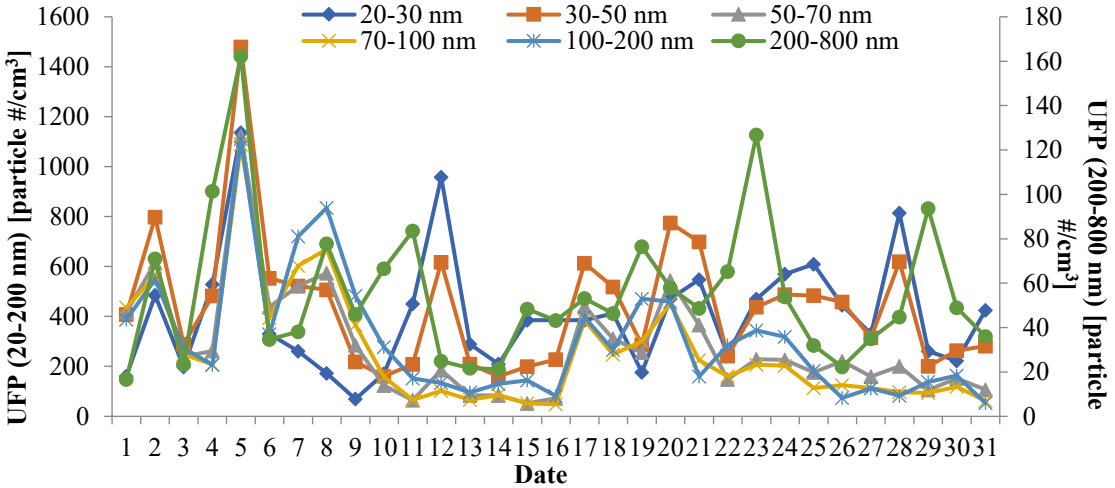

Figure 4-10. Daily mean UFP number concentration (particle #/cm^3) in October 2016.

From Figure 4-9, spike dates of May can be determined: 1st, 11th, 12th,17th, and18th. According to earlier study on phytoplankton and PM studies, May spike is likely to be caused by Atlantic phytoplankton spring bloom (Collins et al., 2017; Craig et al.,

2015). As can be seen in Figure 4-10, 2nd and 5th were two spike days in October. As May spike, October spike is likely to be caused by phytoplankton fall spike. Detailed PM source apportioment analysis would be presented in later sections.

Annual diel average and seasonal diel average will be shown below in Figure 4-11. Diel time-dependent variations of UFP are also assessed in UTC.

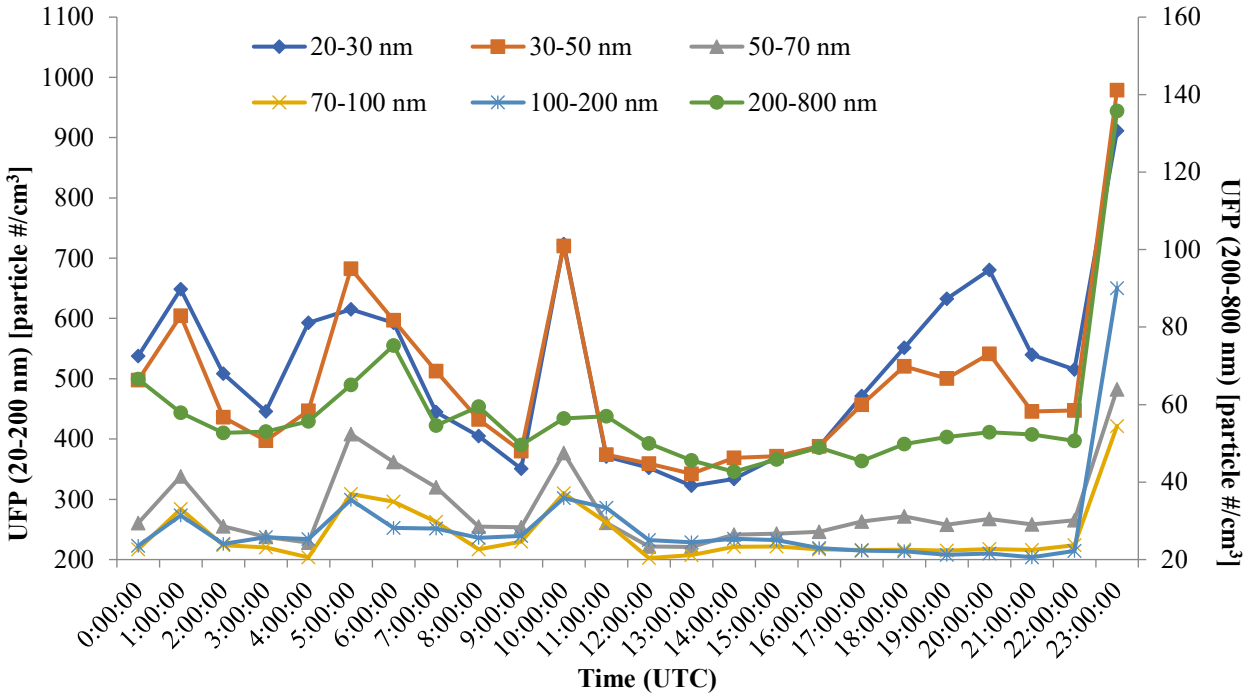

Figure 4-11. Diel average of UFP number concentration (particle #/cm^3) on Sable Island in 2016.

From Figure 4-11, It indicates three peaks for 20-30 nm and 30-50 nm UFP, which occur at 05:00, 10:00, 20:00 and 23:00 UTC and 02:00, 07:00, 17:00 and 20:00 in local time. UFP began to increase at 3 am and 9 am respectively, and reach the first and second peaks at 6 am and 11 am; then they begin to increase at 5 pm and reach the third peak at 8 pm. Among six size fractions, 20-30 nm and 30-50 nm UFP have the largest number concentration.

Figure 4-12 provides the diel UFP number concentrations averaged according to seasons.

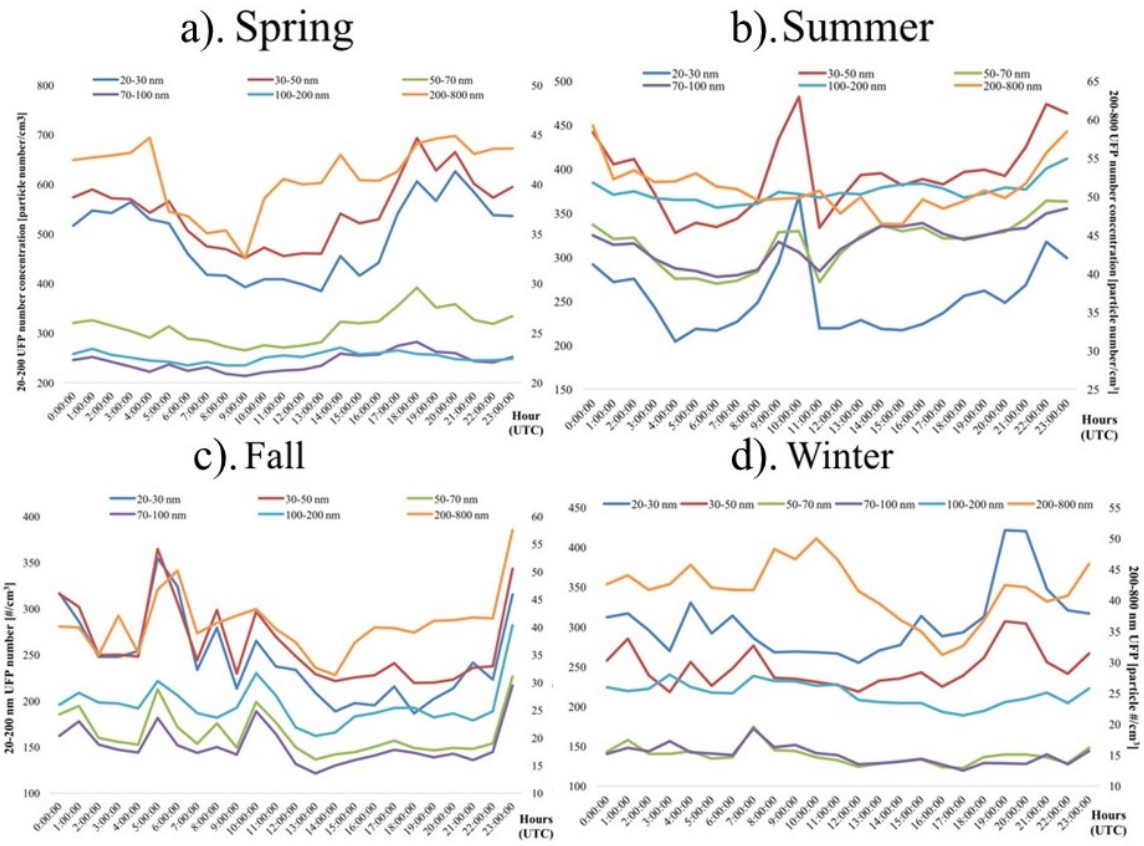

Figure 4-12. Provides four figures of the diel seasonal average of UFP number concentration (particle #/cm^3) on Sable Island in 2016, a). Spring, b). Summer, c). Fall and d). Winter.

From Figure 4-12, it can be observed that in the spring (panel a), the 20-30 nm and 30-50 nm UFP number began to increase at 4 pm. They began to decrease at 3 am and increase at 1 pm. 200-800 nm UFP number concentration increased at 8 am, right after the 20-50 nm UFP peak, which can be assumed that 200 -800 nm UFP were formed from coagulation of 20-50 nm UFP. In the winter, 20-30 nm and 30-50 nm UFP number reached a twin peak during 3-8 am, and a second peak at 7 pm. 200-800 nm UFP number

concentration increases at 8 am, right after the 20-50 nm UFP peak, which can be assumed that 200-800 nm UFP are formed from coagulation of 20-50 nm UFP.

It is likely the spikes in 20-30 nm and 30-50 nm UFP during the day are associated with secondary UFP formed from photochemical induced phytoplankton VOC emissions. Based on a study conducted by Kulmala et al., 2001, an increase of small UFP (<10 nm) concentration was observed during late morning in April; after that they tended to grow into Aitken model and accumulation mode (20-100 nm and 0.1-2.5 μm) particles throughout afternoon and into evening, which matches the UFP tend in Figure 4-12 (Hinds, 1999). Also, in a study investigated by Coe et al., 2000, in a coastal area in England (North East Atlantic Ocean), UFP in accumulation mode (<50 nm) tended to steadily increase in the afternoon and diminish through the evening. In Kulmala's study, it was also mentioned that particle number reached a spike around noon. In diurnal plots for this study, in spring season, it reached a spike at 14:00 UTC which is 11:00 in local time (Coe et al., 2000; Kulmala et al., 2001). Furthermore, in Coe's study, the 20 nm particles did not increase until around 10:00 in the morning, 2 hours later than the increase in the 5 nm size (Coe et al., 2000).

4.2 Source Apportionment analyses and results

4.2.1 Satellite Observations to Aid Source Apportionment

Spikes from PM and UFP annual cycle plots were investigated with the aid of satellite images and air mass back trajectory. NOAA HYSPLIT air mass back trajectory at spike time on spike day was generated to find potential sources for $PM_{1/2.5/4/10/TSP}$ and UFP. Time-averaged maps for selected spikes in UFP annual cycle were generated to identify chlorophyll-a concentration in regions around Sable Island. Giovanni chlorophyll-a concentration maps were blended with air mass back trajectories in Google Earth Pro; graphs were created to aid in identifying potential source regions of UFP on "peak/spike" days. Air mass back trajectories were produced five days before spike day; hourly timestamps were also used to help with identifying potential anthropogenic or natural sources for the formation of UFP.

Figure 4-13 below is monthly HYSPLIT 5-day air mass back trajectory integrated into Google Earth. Each color represents back trajectory for 17th of each month, which is the middle of each month. It can be seen that half of them were coming from the North (which is a clean source); four were from NE US (known for industry, coal combustion, and agriculture) (Gibson et al., 2013; Jeong et al., 2011), and three originated from marine (mostly sea spray, or marine biomass activities if there is phytoplankton bloom detected from satellite).

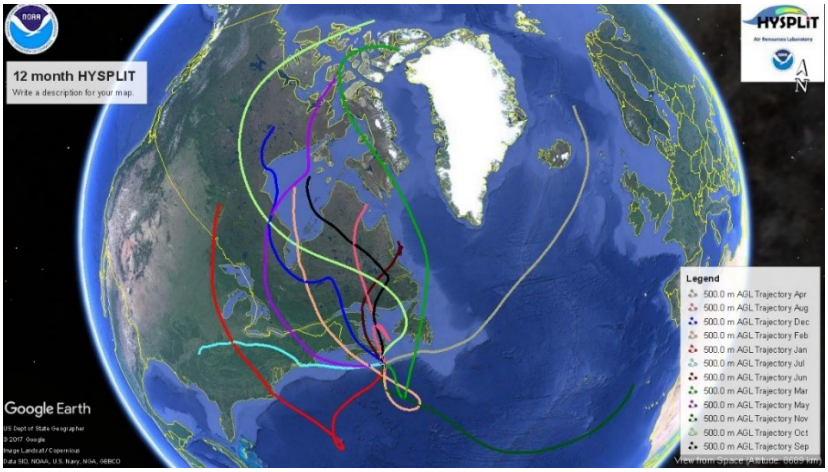

Figure 4-13. Annual cycle HYSPLIT overview.

Annual time averaged map for chlorophyll-a concentration (mg/m^3) from the marine region around Sable Island was also generated and shown in Figure 4-14. As indicated in the legend, the color represents the concentration of chlorophyll-a, from light blue (lowest) to pink purple (median) to yellow (highest). Full details of annual and monthly mean chlorophyll-a concentration satellite images are displayed in Appendix II. Some of them were selected as supplemental information for source apportionment analysis in later sections.

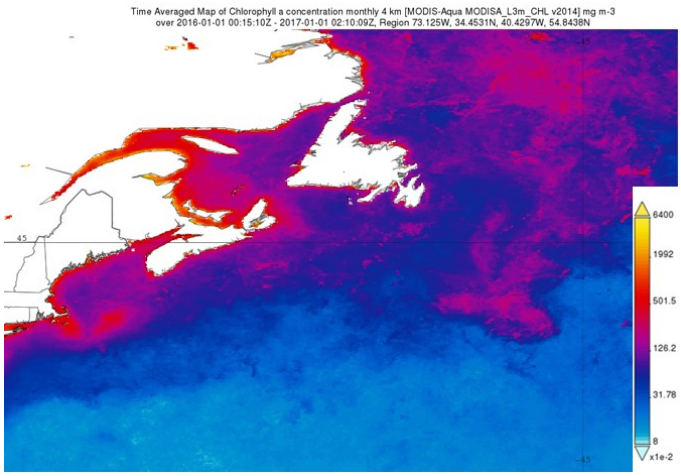

Figure 4-14. Annual mean *chl a* concentration map around Sable Island in 2016 retrieved from Giovanni data system.

4.2.2 Potential Sources and Sinks determination - Principle Component Analysis

Principle component analysis looks for covariance between the underlying latent variables that exist between data in eigen space that cannot be seen in the typical two-dimensional correlation analysis. PCA also allows the identification of the main factors that explain the percentage and primary drivers of the variance within a particular data set. PCA provides columns of correlation values against a certain metric. If the correlation value is above 0.3 or below -0.3 then it has an influence upon that 'factor'. In atmospheric chemistry the 'factor' is the source of an atmospheric component, in our case particle number counts found in a particular size fraction associated with a specific source. Principle Component Analysis on total PM (0.02-20 μm) number measurement has been investigated and shown in Table 4-5 (Full details of PCA table can be obtained in Appendix I).

Table 4-5. Partial summary of PCA on $PM_{0.02-20}$ result

Variable	LRT	Sea spray	Fallout	Coagulation Particles	Freshly formed UFP	Unclassified
20-30 nm					0.801	
30-50 nm					0.645	
50-70 nm				0.917		
70-100 nm				0.942		
100-200 nm				0.869		
200-800 nm						-0.641
1.286 μm	0.964					
5.829 μm		-0.957				
15.96 μm			-0.989			
Variance	20.31	17.22	6.458	4.001	2.195	2.638
% var	0.369	0.313	0.117	0.073	0.04	0.048

In Table 4-5, PCA run on $PM_{0.02-20}$ number concentration were displayed. Applied to the all the UFP and PM daily average number concentration, the PCA revealed 6 factors that accounted for 96% of the variance. Six possible source categories were identified with the knowledge of PM sources and formation. The first factor accounted for 36.9% of the variance and had significant loadings on $PM_{1.286}$, which are typical LRT particles. The second factor has significant negative loadings on $PM_{5.829}$ which is in the range of course particles below 10 μm; this can be categorized into sea spray, it has significant negative correlation with sea spray which is likely to be evaporation of sea spray. Sea spray has high humidity therefore during its quick movement, the water is likely to evaporate which will result in a decrease in particle size. The third factor has the most negative loading in 15.96 μm which is comparatively large in size. It is likely to be windblown particles from surface dust. The loss (negative correlation) of it can result from physical fallout due to relatively large size and mass. The fourth factor has high loadings in 50-200 nm, which are in accumulation mode formed by coagulation. The fifth factor has significant loadings in 20-50 nm UFP, accounting for 4% of the variance. UFP in the range of 20-200 nm are typical freshly formed particle from gas-to-particle conversion. The most probable source being phytoplankton generated VOCs reacting in the atmosphere to form these UFP. Factor 6 has the most negative loading in 200-800 nm, which is still unknown and needed to be investigated.

4.2.3 Potential Sources determination - Positive Matrix Factorization Analysis

The output from EPA PMF model v.5.0.14.21735 run will be presented in this section. The model was run using 20 base runs and 4 factors, with factors representing

the source of the PM number counts. The bootstrap and fpeak were also conducted to check the robustness of the PMF model. The fpeak modelling with bootstrapping was performed on Base Rune #20 with Fpeak Runs = 0.5, Bootstraps # = 100, minimum R^2 = 0.6 and block size = 9. As can be seen in Table 4-6 and Table 4-7, all runs were converged for Q(Robust) and Q (True), the Fpeak run was also converged. Factor contributions, factor variability in the concentration of species, factor time series and pie charts will be provided in this section.

Table 4-6. PMF base run summary

Run Number	Q (Robust)	Q (True)	Converged
1	12177.9	12515.3	Yes
2	12177.9	12515.3	Yes
3	12177.9	12515.3	Yes
4	12177.9	12515.3	Yes
5	12177.9	12515.3	Yes
6	12177.9	12515.3	Yes
7	12177.9	12515.3	Yes
8	12177.9	12515.3	Yes
9	12177.9	12515.3	Yes
10	12177.9	12515.3	Yes
11	12177.9	12515.3	Yes
12	12177.9	12515.3	Yes
13	12177.9	12515.3	Yes
14	12177.9	12515.3	Yes
15	12177.9	12515.3	Yes
16	12177.9	12515.3	Yes
17	12177.9	12515.3	Yes
18	12177.9	12515.3	Yes
19	12177.9	12515.3	Yes
20	12177.9	12515.3	Yes

Table 4-7. Fpeak Model Run Summary

Strength	dQ (Robust)	Q (Robust)	% dQ (Robust)	Q (Aux)	Q (True)	Converged
0.5	45.8	12223.7	0.37	44.3	12516.9	Yes

Q robust and Q true converged for all base runs can be seen in Table 4-6, which demonstrates the stability of the base model run. As described previously, Q value is determined by the total running times, for this study, 218-day data was used and the number of variables = 59, which gives 12862, which is the ideal value for Q (True). The Q value generated from the PMF model was 12516.9 which is close enough to the ideal value, and it is a proof of the stability of this test.

In Figure 4-15 below (top panel), the orange and grey boxes represent the % of that species, from the total species found in the entire data set, associated with this factor (source of PM). The grey boxes are the base model run, and the orange boxes are the fpeak model robustness check. As can be seen, they agree with which provides confidence in the PMF model's performance. The grey bars and green bars represent the concentration of the species associated with this factor (source of PM). Again, the base model and fpeak robustness check agree. The bottom panel shows the concentration of this PM source over the sampling period. The figure panel legend and format descriptions are the same for the remaining three factors (Figure 4-17, and Figure 4-22).

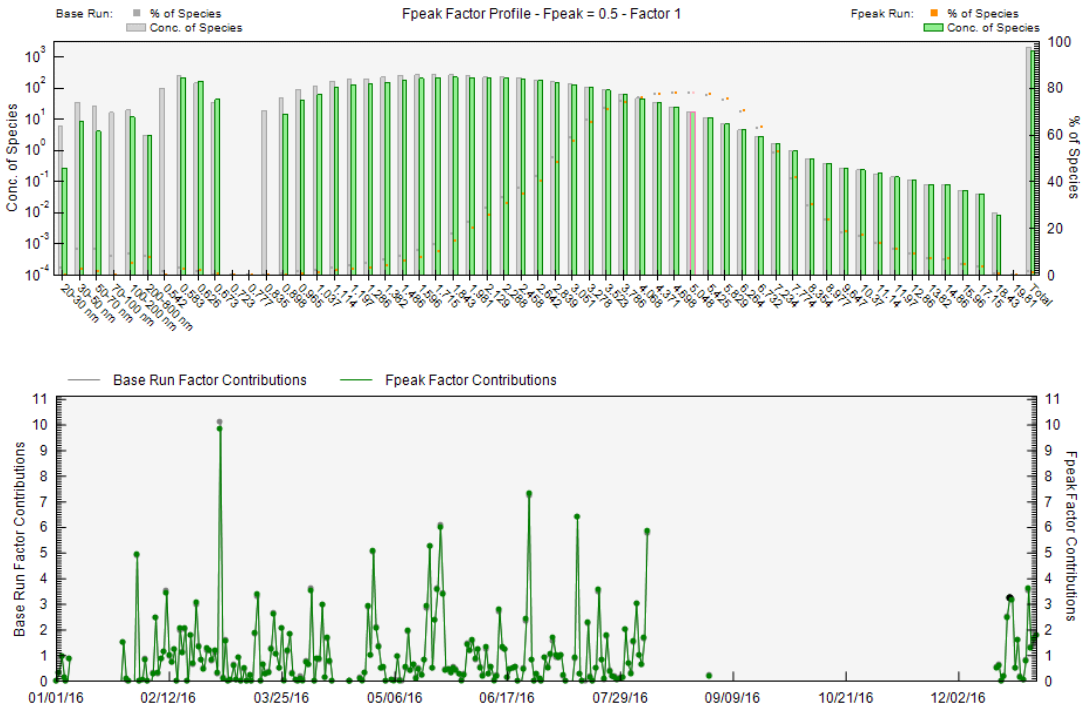

Figure 4-15. Factor 1 source profile (top panel) and mass contribution plot (bottom panel).

From knowledge of the potential source and aerosol theory, Factor 1 was identified as sea spray. In Figure 4-15 percentage profile (top panel), it can be seen that more than 40% of $PM_{2.5-8}$ were found within Factor 1. The source of coarse particles are normally from the break-up of large solids or droplets such as sea spray and mechanical disruptions (Fuzzi et al., 2015; Wilson & Suh, 1997). From factor contribution, four spikes were investigated to help with determining the source. HYSPLIT 5-day air mass back trajectories for spike days (2nd March, 25th June, 13th July, and 23rd May) were generated and shown in Figure 4-16. Three of them originated from the North, which has few anthropogenic sources. Coarse particles do not have a long residence time in the atmosphere, as they are either washed out by precipitation or deposit quickly due to their relatively large mass compared to fine particles and UFP. Because of this, LRT can be

excluded from Factor 1 as this aerosol is typically found below 2.5 µm. For 23rd May air mass back trajectory, the air mass spent its entire 5-day lifetime over the ocean, which leaves sea spray to be the only possible source.

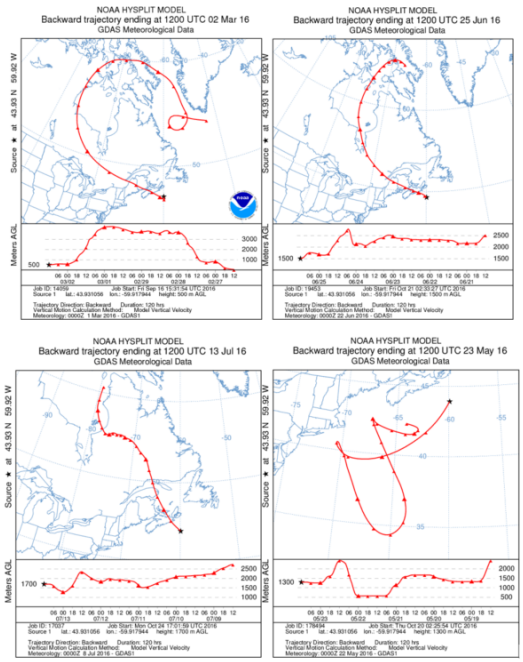

Figure 4-16. HYSPLIT 5-day air mass back trajectory associated with the Factor 1 contribution spikes shown in Figure 4-15.

Figure 4-17 below reveals the Factor 2 source species profile and factor contribution timeseries.

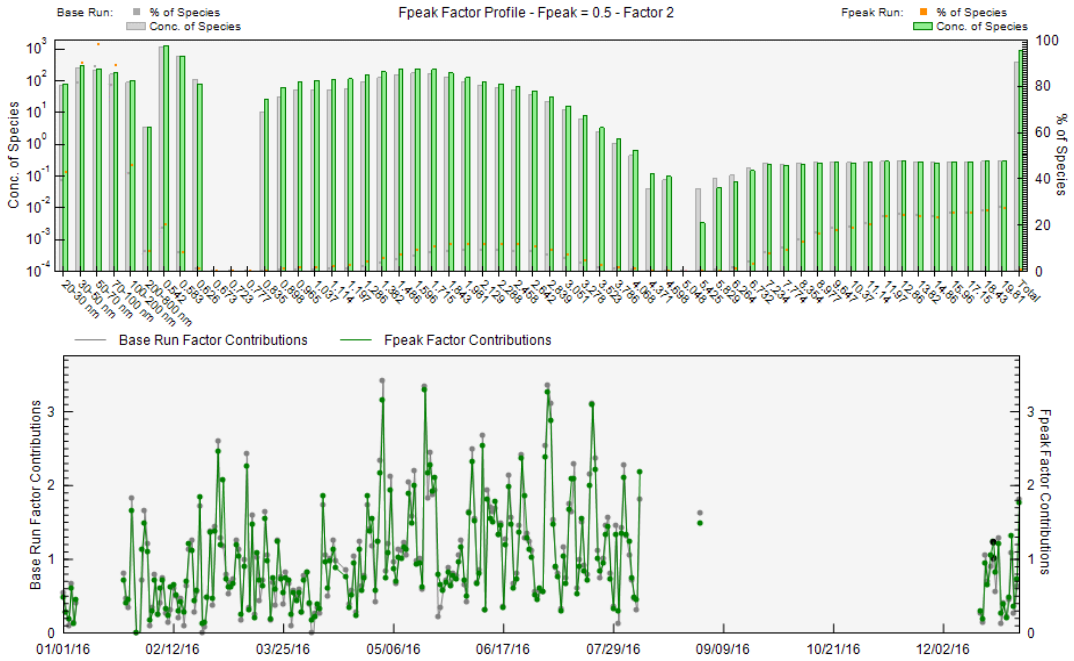

Figure 4-17. Factor 2 source profile (top panel) and mass contribution plot (bottom panel).

From the knowledge of marine sources and ocean-atmosphere chemistry and physics, Factor 2 was chosen as biogenic marine secondary particles. From species percentage in the factor profile and time series in Figure 4-17, it can be determined that Factor 2 is dominated by more than 80% of UFP 20-200 nm, which is known to be only formed from fresh combustion gases or gas-to-particle conversion.

HYSPLIT air mass back trajectory (Figure 4-18) was also generated for spike days (2nd & 18th May, 4th & 21st Jul) in Factor 2 timeseries. There was a phytoplankton bloom in May 1st - 2nd around Sable Island (Figure 4-19), so phytoplankton VOC gas-to-particle conversion is the likely source.

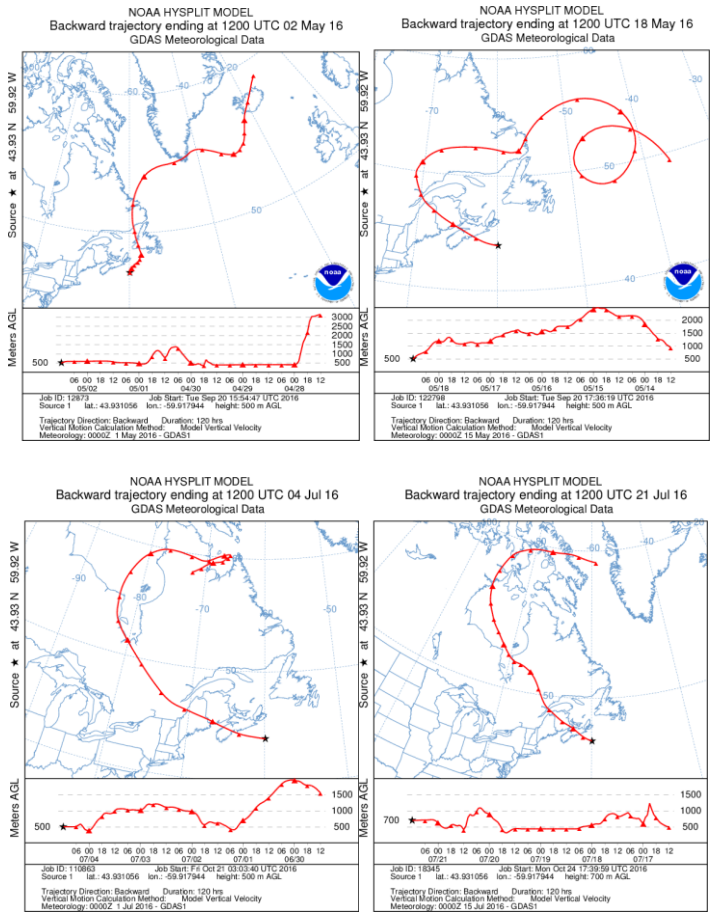

Figure 4-18. HYSPLIT 5-day air mass back trajectory for Factor 2 spikes.

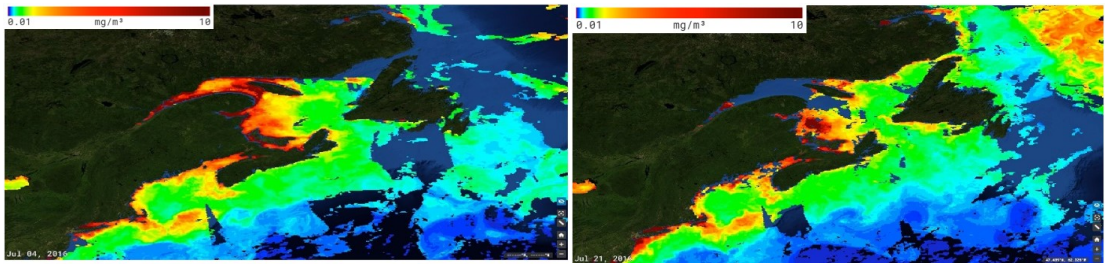

Figure 4-19. SOTO daily chlorophyll a concentration around Sable Island on Jul. 04th (left) and Jul. 21st (right).

Figure 4-20 below reveals the Factor 2 source species profile and factor contribution timeseries.

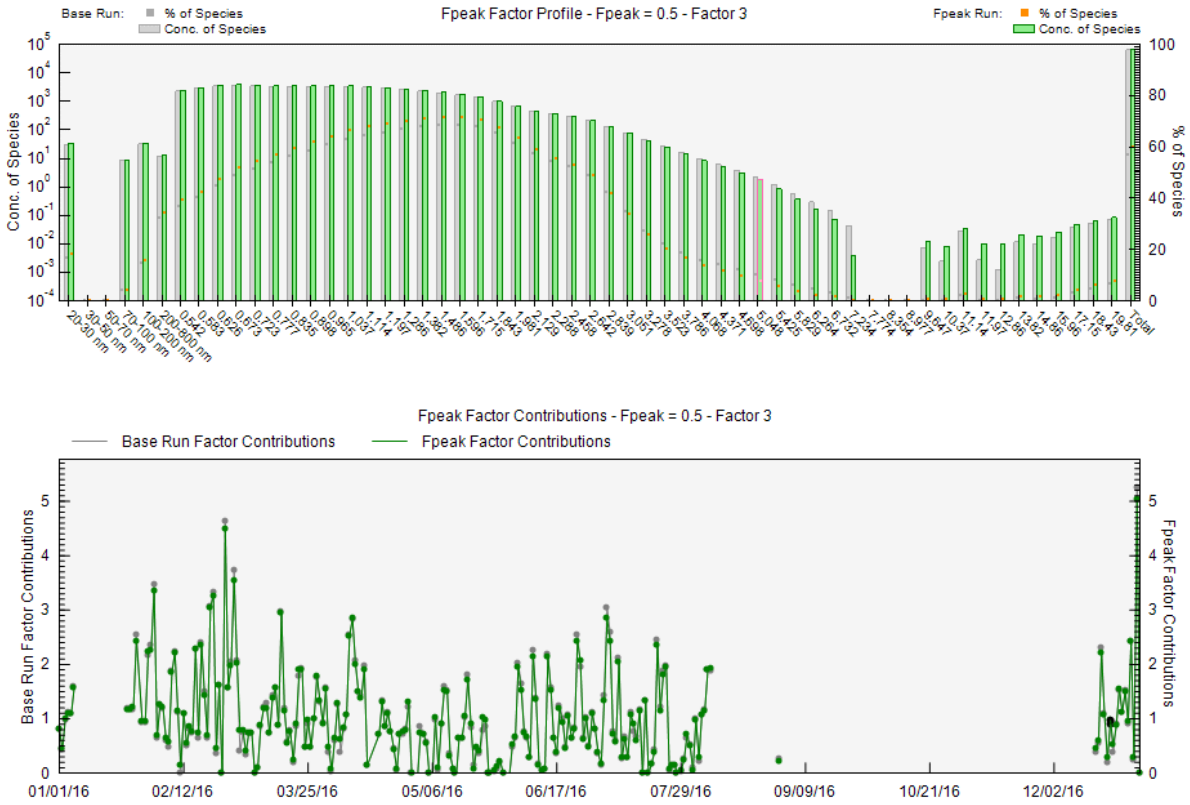

Figure 4-20. Factor 3 source profile (top panel) and mass contribution plot (bottom panel).

With factor profile shown in Figure 4-20 and the knowledge of coarse particles and their potential sources around Halifax, Factor 3 was identified as LRT. From species percentage in factor profile and timeseries in Figure 4-20**,** it can be determined that Factor 3 is dominated by $PM_{0.5\text{-}2.8}$, which are in accumulation mode and can exist in the atmosphere for few days or even weeks.

HYSPLIT air mass back trajectory (Figure 4-21) was also generated for spike days (2nd, 26th & 29th Feb., 16th March, and 8th Jun) in Factor 3 time series. All of them expect Mar 16 originated from west of Canada and they moved along Canada/US boundary from the NE US, which is an industrial source region.

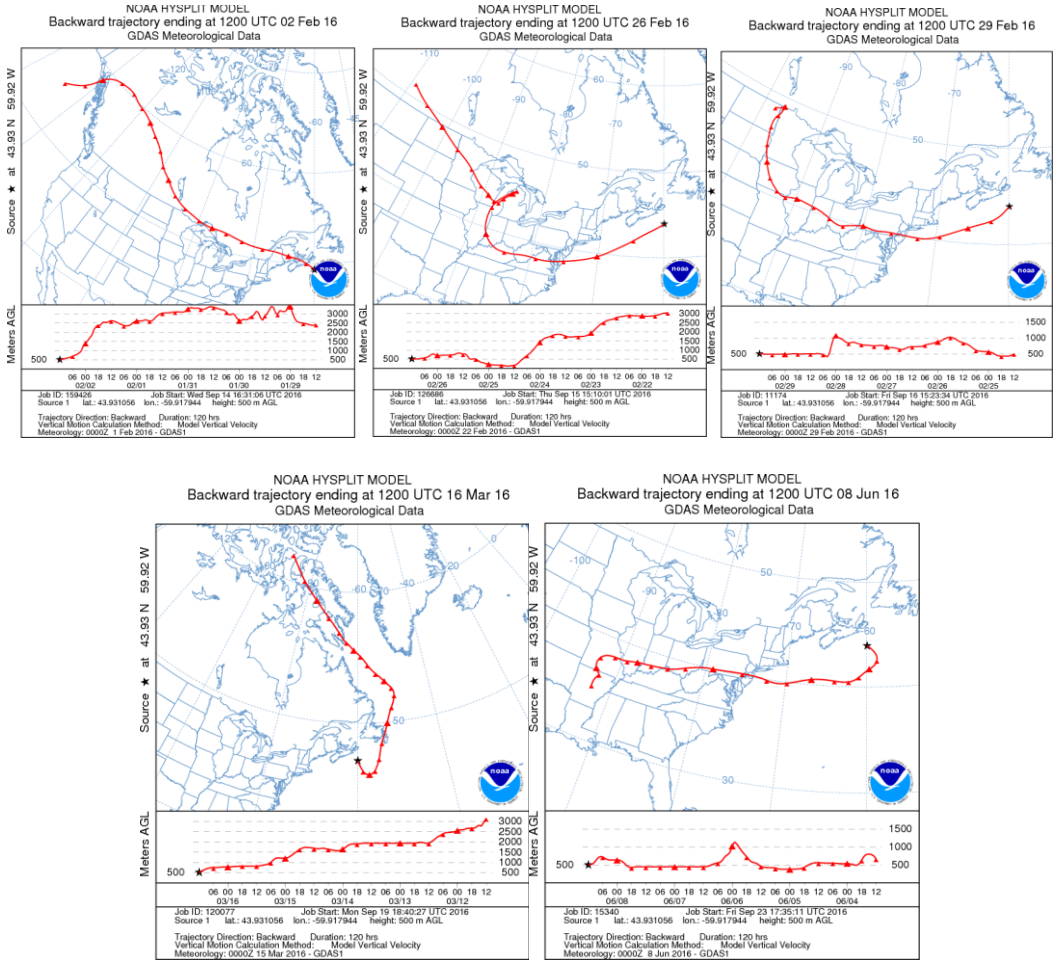

Figure 4-21. HYSPLIT 5-day air mass back trajectories associated with Figure 4-20 for Factor 3 (LRT) spikes.

Figure 4-22 below reveals the Factor 4 source species profile and factor contribution timeseries.

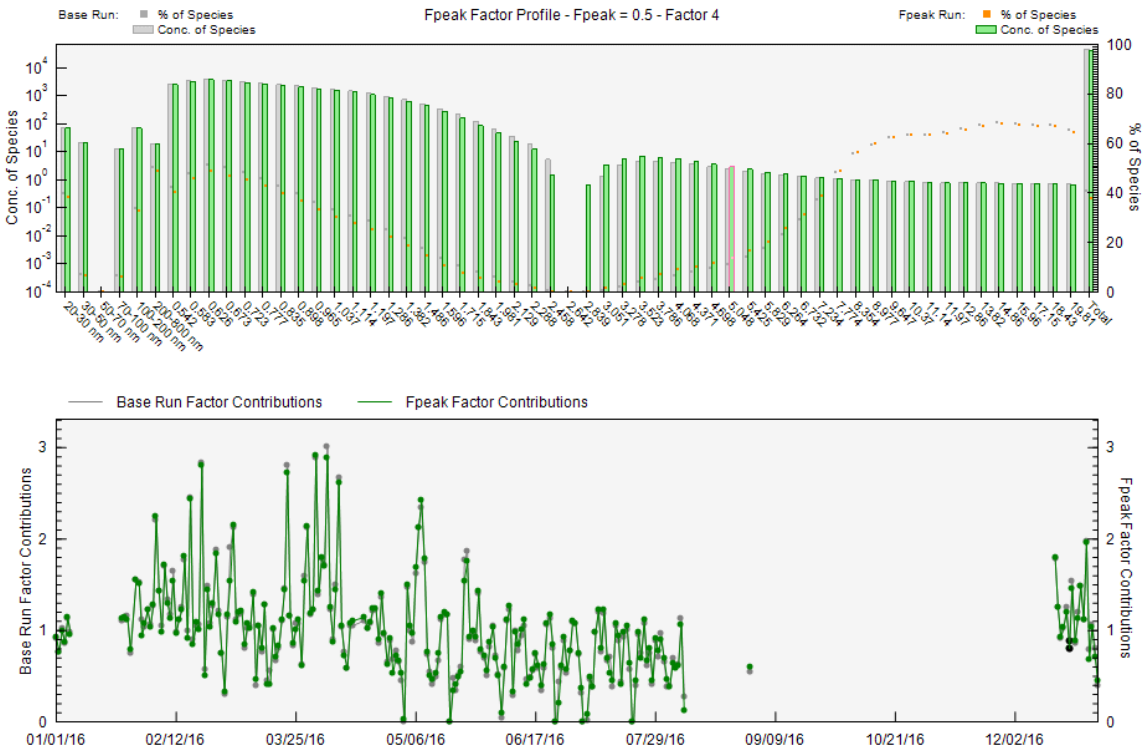

Figure 4-22. Factor 4 source profile (top panel) and mass contribution plot (bottom panel).

As can be seen in Figure 4-22, it can be determined that Factor 4 is characterized by 50% of $PM_{0.2\text{-}1}$ & $PM_{>7.5}$ and UFP 20-30 µm. Therefore, the source of Factor 4 was identified as surface dust with contributions from aging UFP. $PM_{>7.5}$ are mostly from the break-up of large solids or droplets such as windblown dust, UFP 20-30 nm is likely from coagulation of freshly formed UFP.

HYSPLIT air mass back trajectory (Figure 4-23) was also generated for spike days (17th Feb, 21st & 22nd March, 1st & 5th April, and 8th May) in Factor 4 timeseries. Three of them originated from the North part which is known to have relatively clean air (Gibson, Kundu, & Satish, 2013). All of the trajectories do pass the oil and gas field before arriving at Sable Island, which may bring some fresh combustion products to the site and cause a spike in UFP. This would require further exploration to confirm.

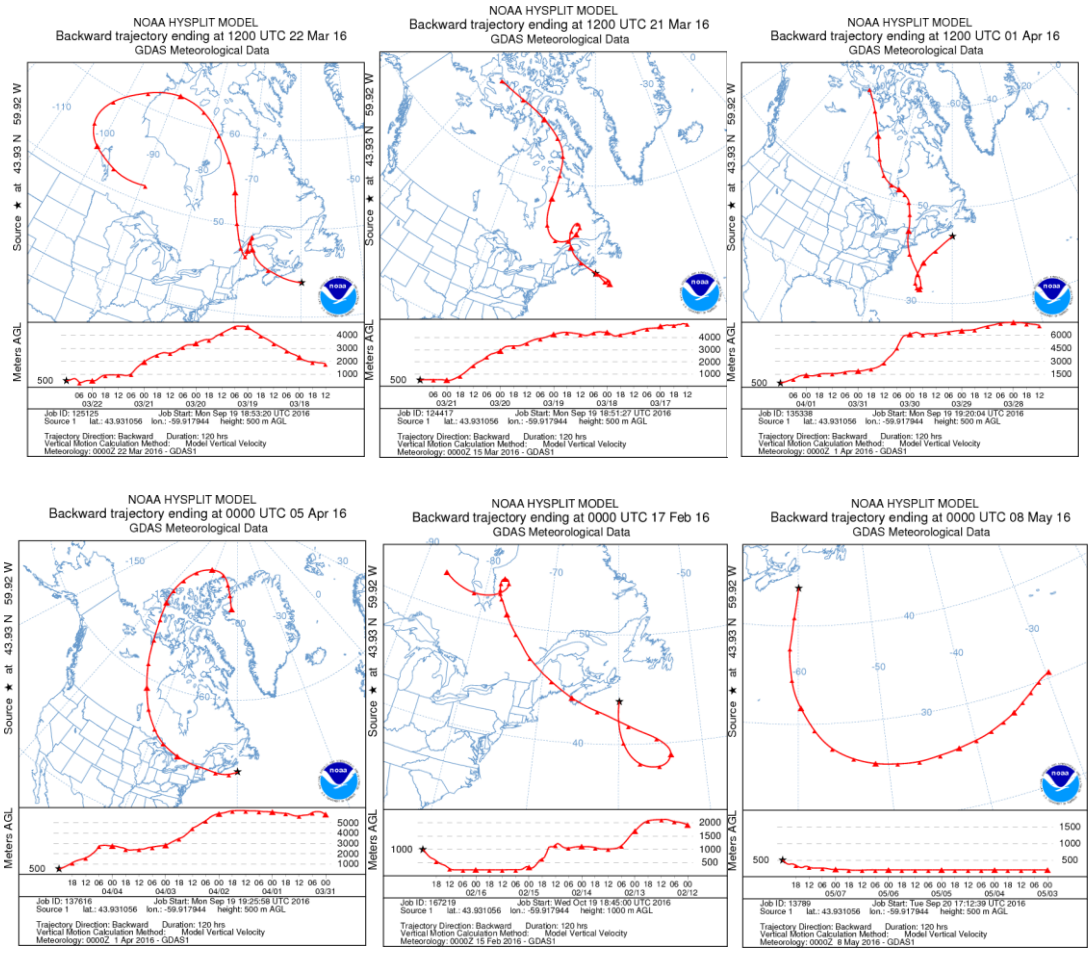

Figure 4-23. HYSPLIT 5-day air mass back trajectory for Factor 4 spikes.

Figure 4-24 below shows factor source attribution for the PM number concentration, and presents the dominant factors for PM in different size fractions (20 nm – 20 µm).

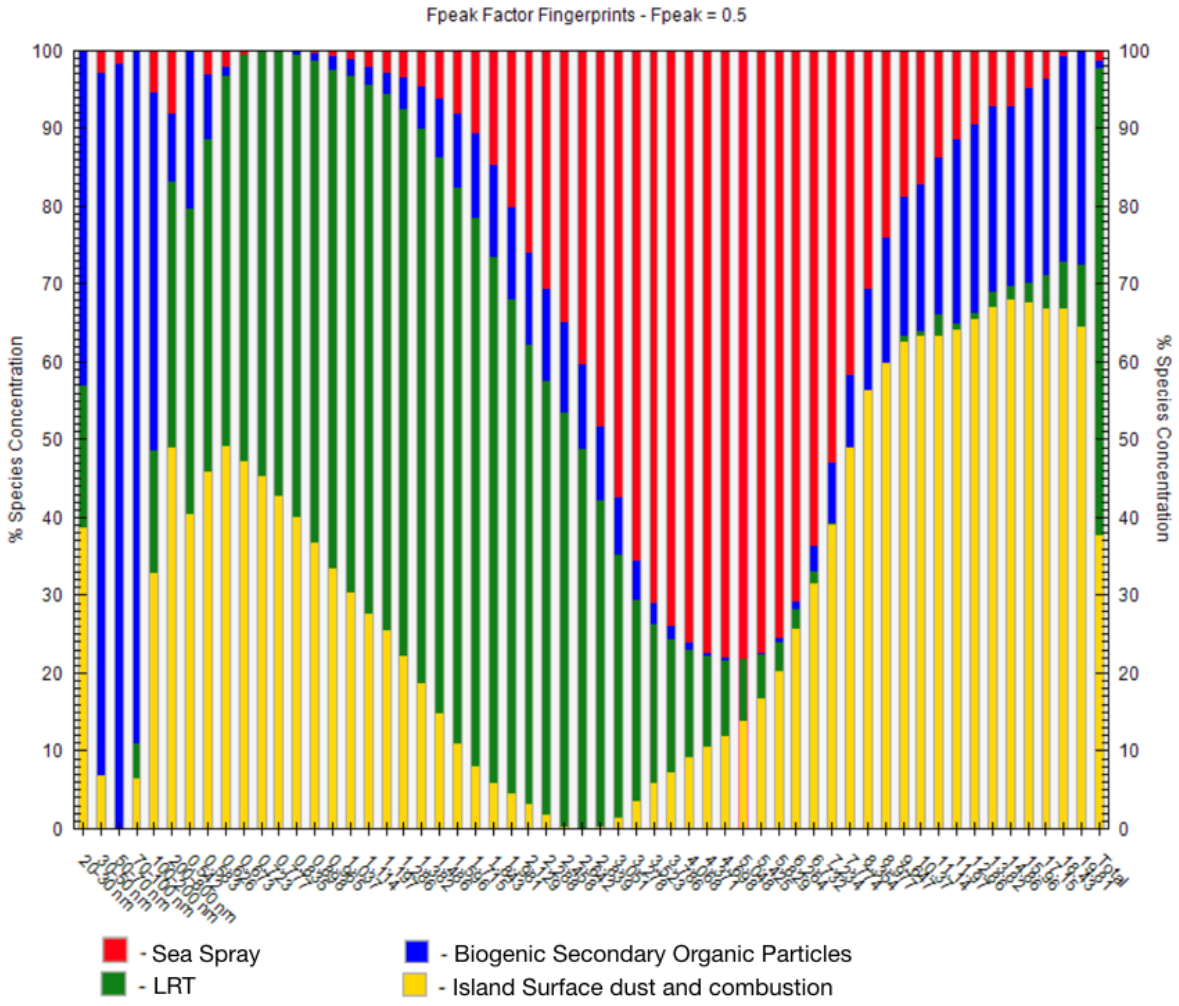

Figure 4-24. Factor (Source) attribution.

Figure 4-24 shows the dominant source of PM number concentration versus size fraction from 20 nm to 20 µm. Coarse PM (2.5 – 10 µm) are dominating factor 1 (sea spray); UFP in the size of 20-200 nm are dominating Factor 2 (secondary marine biogenic particles); fine PM (0.2-4 µm) dominates Factor 3 (LRT); Factor 4 is mostly PM 20-30 nm, 0.1-2 µm and above 7.5 µm, which can be combustion fragments and dust

from island surface and anthropogenic activities. In another point of view, 90% of UFP 30-200 nm are marine secondary biogenic particles, more than 50% of $PM_{0.5-2.5}$ are LRT (the rest are from island surface dust), more than 50% of $PM_{2.5-8}$ are sea salt, and more than 50% of PM_{8-20} are island surface dust and combustion.

Figure 4-25 provides a pie chart of components of total UFP.

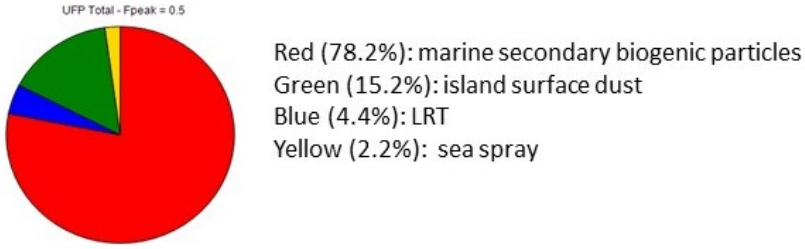

Figure 4-25. Pie chart of total UFP components.

In Figure 4-25 it can be seen that the marine secondary biogenic particles account for 78.2% of total UFP; island surface dust account for 15% of total UFP, according to Figure 4-24, mostly UFP 200-800 nm; LRT and sea spray contribute to the rest 6% of total UFP. Figure 4-26 below provides a source contribution pie chart of total PM number concentration.

Figure 4-26. Pie chart of total PM components.

From Figure 4-26, it can be seen that 60% of total PM (including UFP and $PM_{0.5-20}$) are from LRT, it is reasonable as fine PM have largest number counter; 37.7% of PM are from island surface dust and the rest 2% are attributable to marine.

Table 4-8 below summarized the source attributions of UFP and $PM_{0.5-20}$.

Table 4-8. Summary of sources for UFP and PM

	Sea Spray (%)	Marine Secondary biogenic particles (%)	LRT (%)	Island dust (%)
20 – 30 nm	0.2	42.8	18.4	38.6
30 – 50 nm	2.7	90.3	0	6.9
50 – 70 nm	1.7	98.3	0	0
70 – 100 nm	0	89.1	4.5	6.4
100 – 200 nm	5.4	45.9	15.7	33.0
200 – 800 nm	8.0	8.8	34.2	49.0
UFP Total	2.2	78.2	4.4	15.2
PM Total	1.3	0.8	60.1	37.7

It can be seen in Table 4-8 that LRT accounts for most of the total number concentrations, which makes sense as fine particles exist for the longest time. Secondary marine biogenic particles account for 90% of UFP 30-50 nm, so we can conclude that formation of 30-50 nm UFP are strongly associated with VOCs from phytoplankton or other co-varying biogenic processes. This, agrees with our mean monthly UFP vs *chl a* plot in later sections. The four size-resolved sources were sea spray (2.2% of total UFP, 1.3% of total PM), secondary marine biogenic particles (78.2% of total UFP, 0.8% of total PM), LRT (4.4% of total UFP, 60.1% of total PM) and island surface dusts (15.2% of total UFP, 37.7% of total PM), where secondary marine biogenic particles was the dominant contributor to UFP and LRT was the dominant contributor to PM.

4.2.4 Ultrafine Particle Source Determination

Spikes appeared in annual cycle UFP number concentration plots (May 1st, May 11th, May 17th, Oct. 5th, and Oct 11th) were investigated for source apportionment. For each spike day, the hourly UFP number concentration, air mass back trajectory, *chl a* concentration along air mass pathway and satellite images (if necessary) were studied and gathered. The time that spike occurred in the day was set as arrival time when retrieving HYSPLIT air mass back trajectory from NOAA website. Hourly wind speed on spike days were also provided to assist source apportionment.

May 1st UFP Spike

Figure 4-27 below shows source apportionment analysis (hourly UFP number concentration plot, air mass back trajectory on arrival date and SOTO daily phytoplankton abundance) for UFP spike occurred on May 1st.

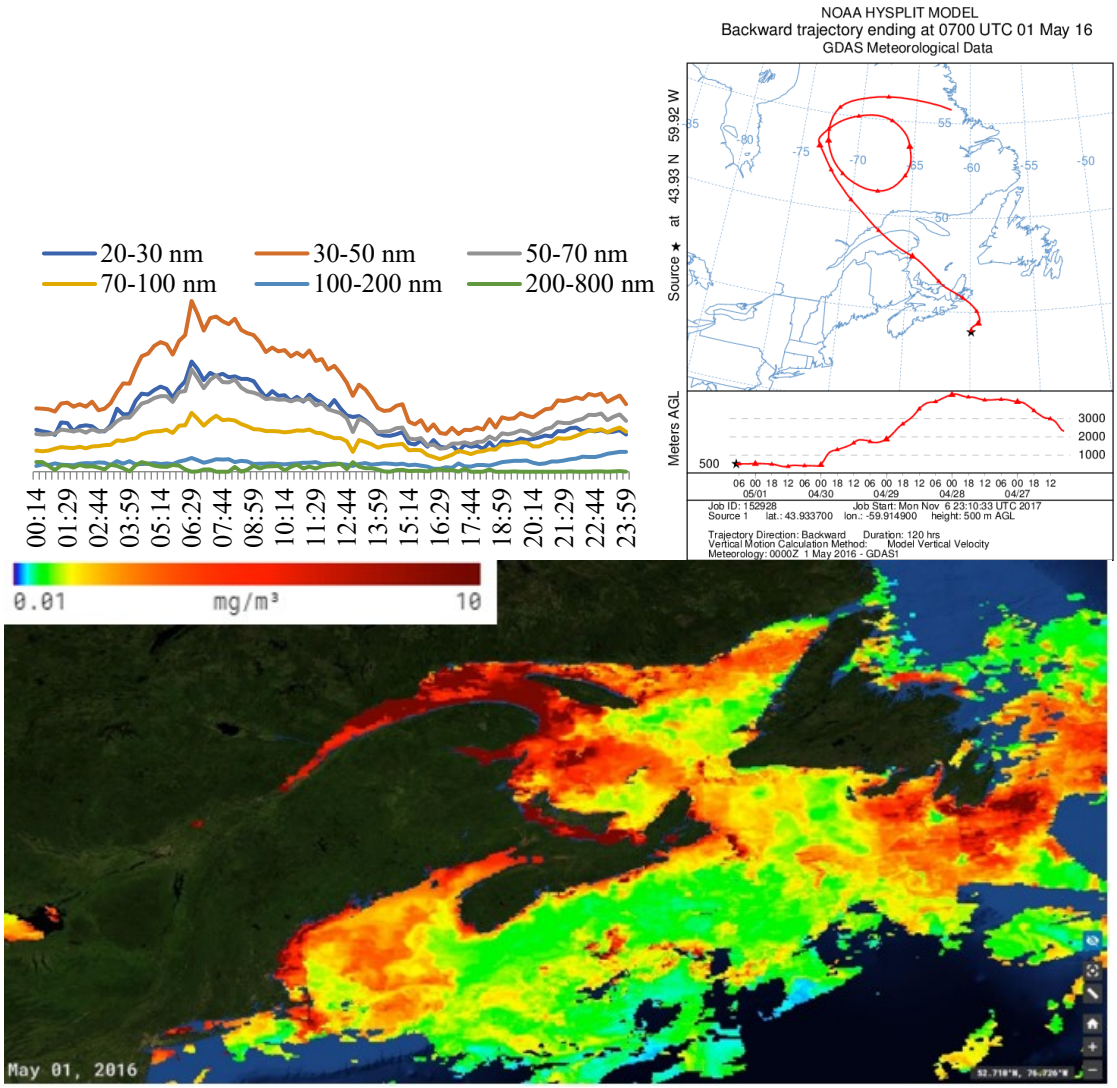

Figure 4-27. May 1st spike: hourly mean UFP plot (top left) and 5-day air mass back trajectory (top right), SOTO daily *chl a* concentration around the region (bottom).

From hourly mean UFP number counter plot shown in Figure 4-27**,** the May 1st UFP spike occurred at 6:30 am UTC where the 20-30, 30-50, 50-70, 70-100, 100-200 and 200-800 nm number counts reached 1913, 2963, 1775, 1022, 239 and 0 particle/cm^3, respectively. Air mass originated from Newfoundland coast and moved above Quebec at an altitude of 3000-4000 km (Figure 4-27), then lowered in altitude on approach to and crossing the St. Lawrence River. It then stayed at an altitude of 500 m until it left NS mainland crossing to Sable Island. The chlorophyll-a concentration in St. Lawrence River and along NS coast were high at that time, implying that VOCs emitted by phytoplankton underwent gas-to-particle reactions forming UFP that generated the spike in number on Sable Island on May 1st.

May 11th UFP Spike

Figure 4-28 below shows source apportionment analysis (hourly UFP number concentration plot, air mass back trajectory on arrival date and SOTO daily phytoplankton abundance) for UFP spike occurred on May 11th – 12th.

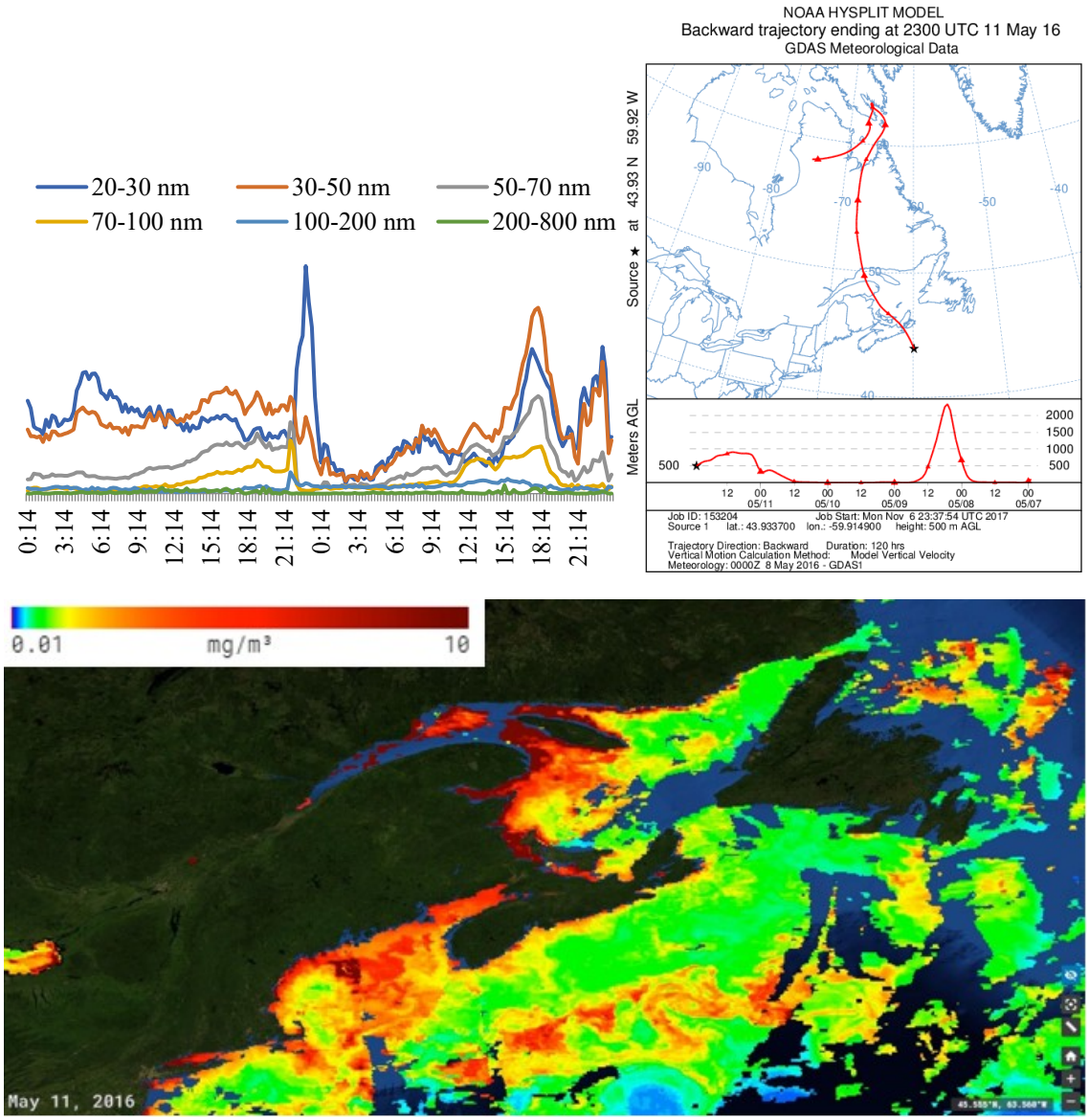

Figure 4-28. May 11th-12th spike: 48-hour hourly mean UFP plot (top left), 5-day air mass back trajectory ending at 23 pm 11th May 2016 (top right) and SOTO daily *chl a* concentration around the region (bottom).

From 48-hour hourly mean UFP plot shown in Figure 4-28**,** the spike on May 11th occurred at 22:30 UTC where the 20-30, 30-50, 50-70, 70-100, 100-200 and 200-800 nm number counts reached 3296, 1138, 91, 96, 191 and 0 particle/cm^3, respectively; the second larger spike on May 12th occurred at 17:45 UTC where the 20-30, 30-50, 50-70, 70-100, 100-200 and 200-800 nm number counts reached 3096, 4120, 2134, 1037, 185 and 117 particle/cm^3, respectively. It can be seen in Figure 4-28, air mass originated from Northern Quebec and moved at low altitude, then lowered in altitude further when approaching and crossing St. Lawrence River, after that it past PEI and went directly to Sable Island from NS mainland. The *chl a* concentration in PEI coastal area, St. Lawrence River and along NS coast were elevated at that time, and therefore phytoplankton VOC emissions reacting in the atmosphere to form aerosols can be considered as the likely source of the UFP spike on Sable Island on May 11-12th.

May 17th UFP Spike

Figure 4-29 below shows source apportionment analysis (hourly UFP number concentration plot, air mass back trajectory on arrival date and SOTO daily phytoplankton abundance) for UFP spike occurred on May 17th – 18th.

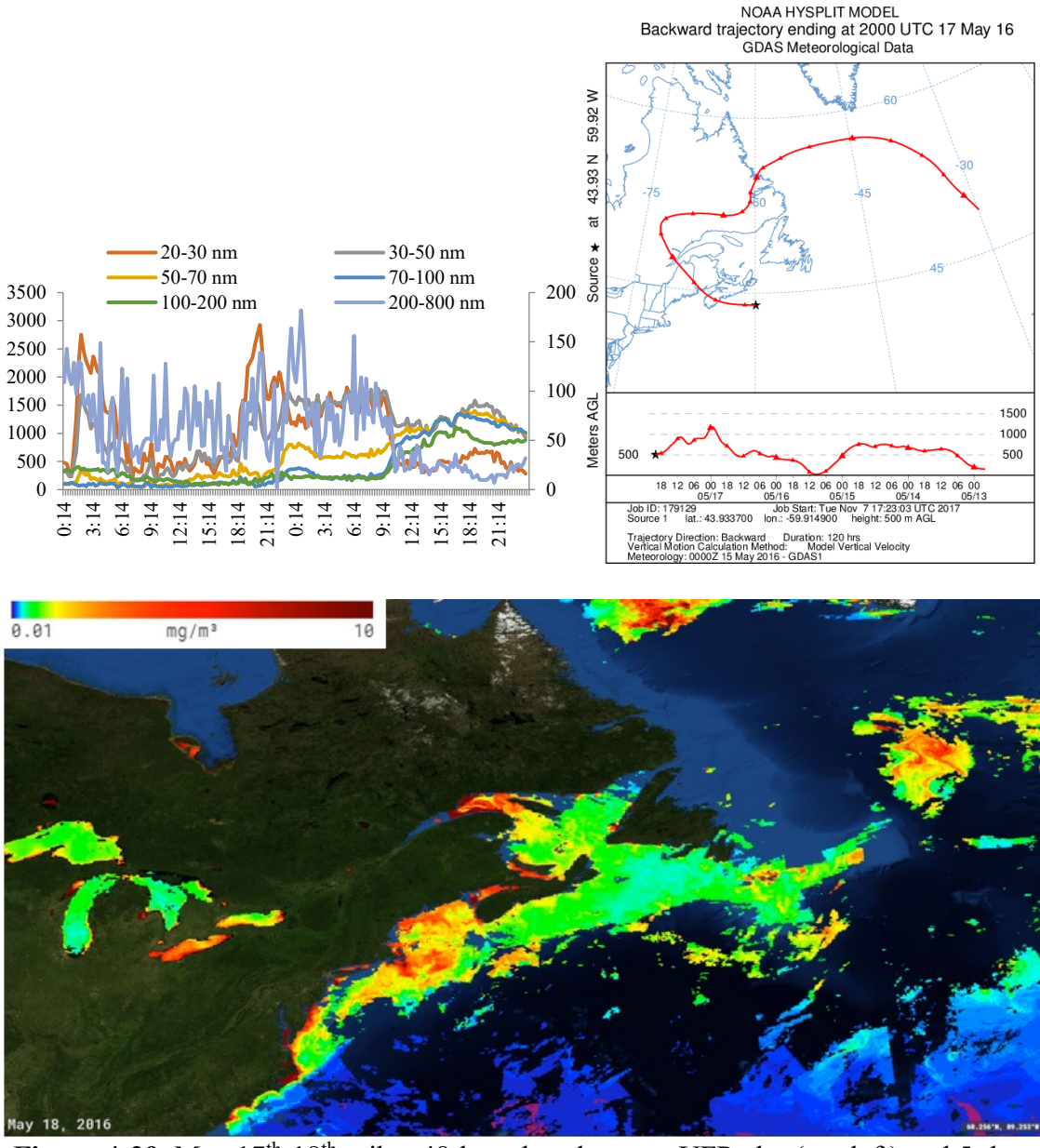

Figure 4-29. May 17th-18th spike: 48-hour hourly mean UFP plot (top left) and 5-day air mass back trajectory ending at 8 pm on 17th May (top right), Chlorophyll-a concentration around the region (bottom).

From 48-hour hourly mean UFP number counter plot shown in Figure 4-29, the UFP number counter spike on May 17-18th occurred at 2:00 and 20:15 UTC on May 17th where the 20-30, 30-50, 50-70, 70-100, 100-200 and 200-800 nm number counts reached 2776, 1535, 290, 67, 125 and 105 particle/cm^3, respectively at 20:15 on May 17th; the second larger spike on May 17th occurred at 17:45 UTC where the 20-30, 30-50, 50-70, 70-100, 100-200 and 200-800 nm number counts reached 2752, 1686, 335, 80, 351 and 128 particle/cm^3, respectively. Air mass originated from middle of Atlantic Ocean (Figure 4-29), moved westward through Newfoundland and Quebec, then went down southward across St. Lawrence River (19 hours before arrival on Sable Island) and Bay of Fundy (10 hours before arriving at Sable Island), after that arrived on Sable Island from NS mainland. The *chl a* concentration in St. Lawrence River, Bay of Fundy and NS coast was around 5.5 mg/m^3, and that can be considered as a source of UFP spike on Sable Island on May 17-18th. Furthermore, PM daily variance in May was also plotted, a spike (PM_1 reaching 24444 particle number/cm^3) was investigated on May 18th, which can be considered to be a result of coagulation of UFPs.

Oct 5th UFP Spike

Figure 4-30 below shows source apportionment analysis (hourly UFP number concentration plot, air mass back trajectory on arrival date and SOTO daily phytoplankton abundance) for UFP spike occurred on Oct 5th.

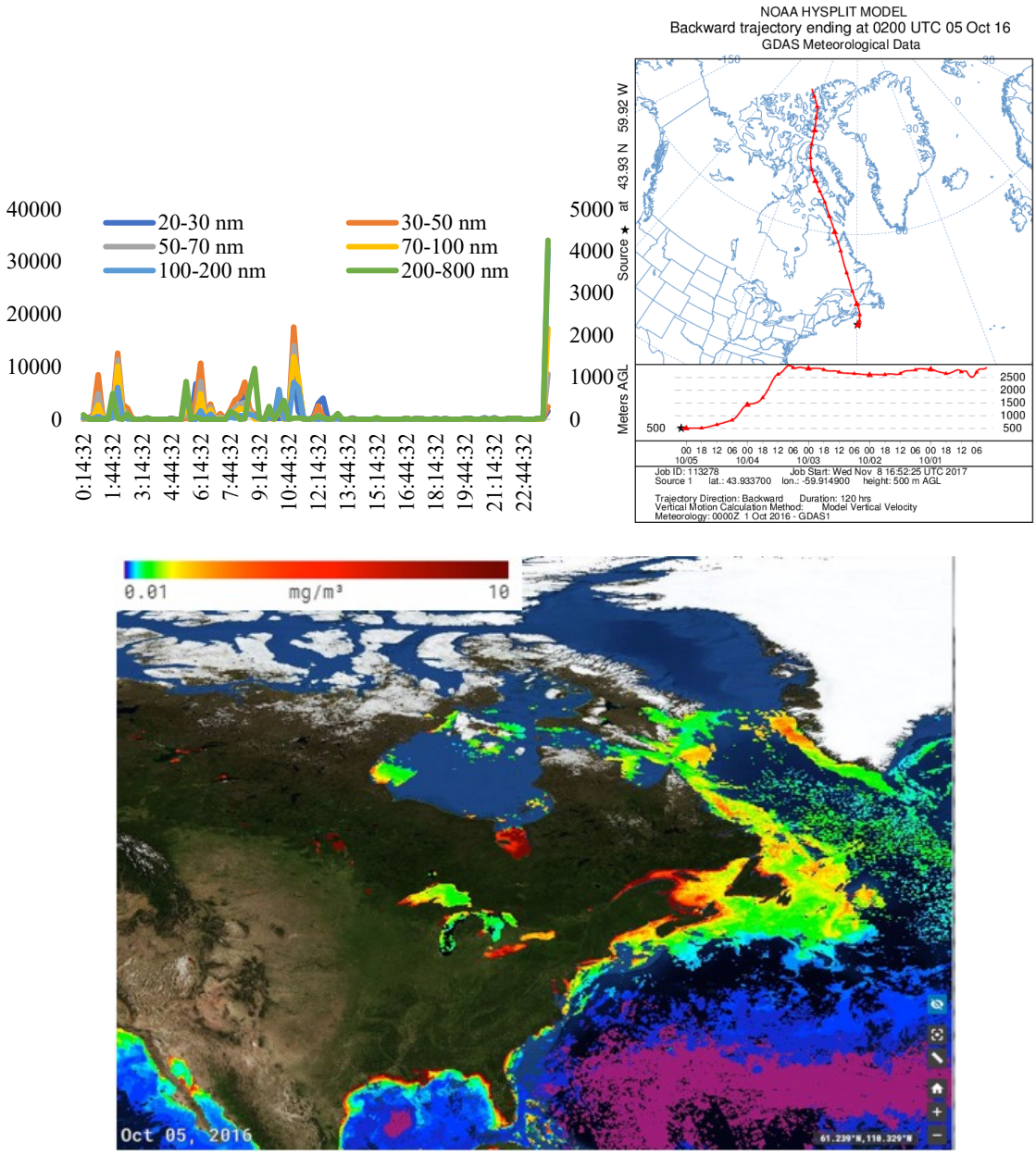

Figure 4-30. Oct 5th spike: hourly mean UFP plot (top left) and 5-day air mass back trajectory (top right), SOTO daily *chl a* concentration around the region (bottom).

From hourly mean UFP number counter plot shown in Figure 4-30, The spike on Oct 5th occurred several times during the morning where the 20-30, 30-50, 50-70, 70-100, 100-200 and 200-800 nm number counts reached 1136, 1480, 1124, 1089, 1111 and 162 particle/cm^3, respectively. Air mass originated from arctic area which does not have many anthropogenic sources. Then it moved straight south to Sable Island passing Gulf of St. Lawrence. The *chl a* concentration on that day was not significantly high enough to bring up a UFP spike; especially the sudden increase at 12 at night which pulls up the average of daily mean concentration for Oct 5th; it can be due to instrumental error adjustment. Figure 4-31 below shows source apportionment analysis (hourly UFP number concentration plot and hourly wind speed plot) for UFP spike occurred on Oct 11th – 13th.

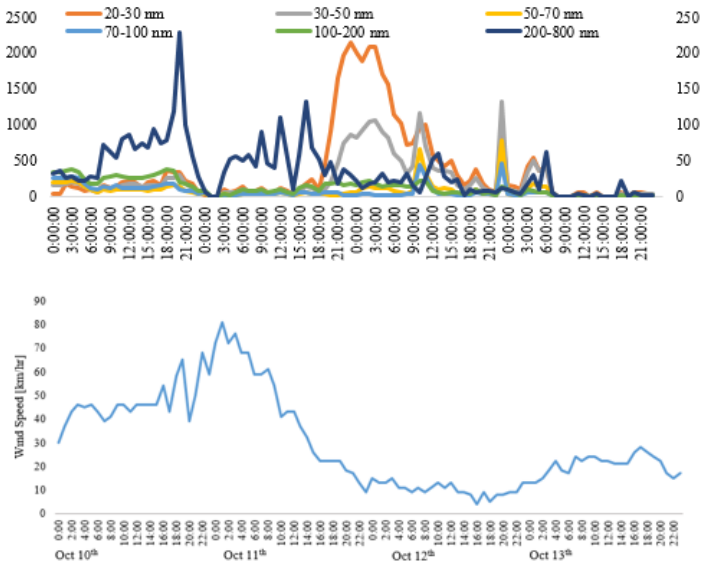

Figure 4-31. Oct 11th spike: Oct 10th – 13th 4-day hourly UFP number concentration [*#/cm^3*] (top), and Oct 10th – 13th 4-day hourly wind speed (bottom).

In hourly mean UFP number counter plot shown in Figure 4-31, the spike on Oct 11th occurred at 23:00 where the 20-30, 30-50, 50-70, 70-100, 100-200 and 200-800 nm

number counts reached 2147, 865, 65, 19, 175 and 31 particle/cm^3, respectively. The hourly mean wind speed during Oct 10th – 13th was also plotted in Figure 4-31 (bottom panel), it can be seen that the wind speed was increasing and maintained in a rather high speed till Oct 11th morning; then few hours later in the afternoon, 20-30 nm and 30-50 nm UFP number counter began to increase.

Oct 11th UFP spike

Figure 4-32 below shows 72-hour HYSPLIT air mass back trajectory on arrival date and SOTO daily phytoplankton abundance for UFP spike source apportionment analysis occurred on Oct 11th – 13th.

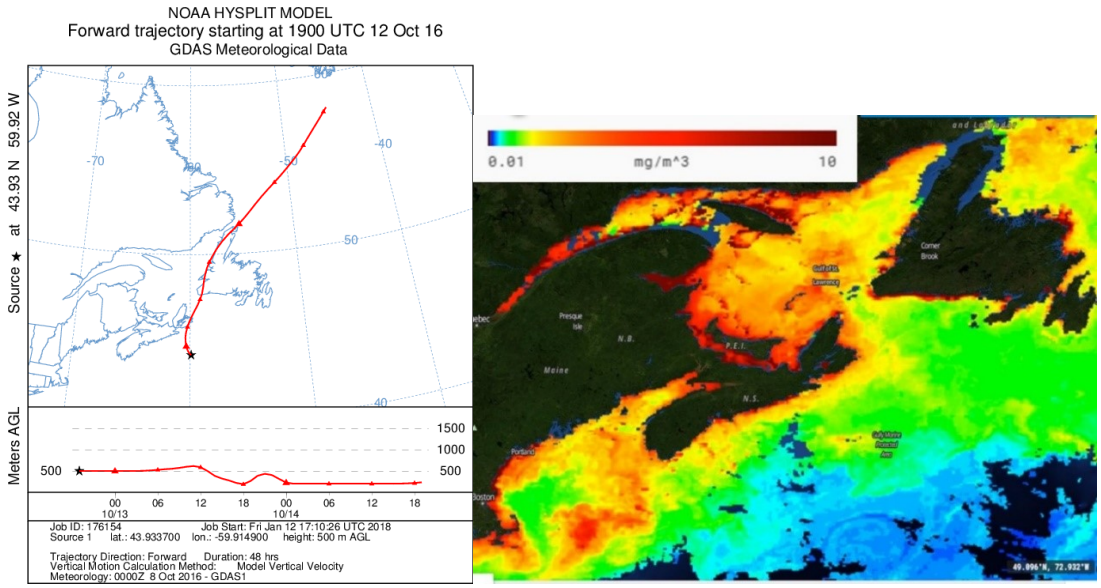

Figure 4-32. Oct 11th spike: 72-hour HYSPLIT 72-hour air mass back trajectory (left), Oct 12th SOTO daily chlorophyll-a concentration (right).

The 72-hr air mass back trajectory was generated for a better view of short-term air mass transport (Figure 4-32 left panel). It originated from Newfoundland and Labrador east coast, moved across Gulf of St. Lawrence and past northeast corner of Cape Breton, not much anthropogenic evidence (about 8 hours before arrival), after that it went directly to Sable Island. The concentration of chlorophyll-a (Figure 4-32 right panel) along the path was approximately 7 (maximum was 10) mg/m^3 along NS coast and 4 mg/m^3 between NS mainland and Sable Island, which indicates phytoplankton growth around Sable Island. So, the spike on Oct 11-12 midnight can be considered as a result of gas-to-particle conversion of phytoplankton emissions as well as other co-varying biogenic emissions. Considering source attribution conducted in PMF, 49% of the 200-800 nm UFP are from island surface dust; in the meantime, the wind speed in Oct 10^{th} daytime was high, therefore the 200-800 nm UFP peak appeared during the daytime on 10^{th} can be from sea spray.

4.2.5 Fine and Course Particulate Matter Source Determination

Spikes appeared in annual cycle PM concentration plots (Jan. 27th, Feb. 26th and Apr. 9th) were investigated via source apportionment analysis. For each spike day, the hourly PM concentration, HYSPLIT air mass back trajectory and satellite images (if necessary) were studied and gathered. Both PM mass concentration and number concentration were presented, the time that spike occurred in the day was set as arrival time when retrieving HYSPLIT air mass back trajectory from NOAA website.

Jan. 27th PM Spike

Figure 4-33 below shows source apportionment analysis (hourly PM number and mass concentration plot and HYSLPIT air mass back trajectory on arrival date) for PM spike occurred on Jan. 27th.

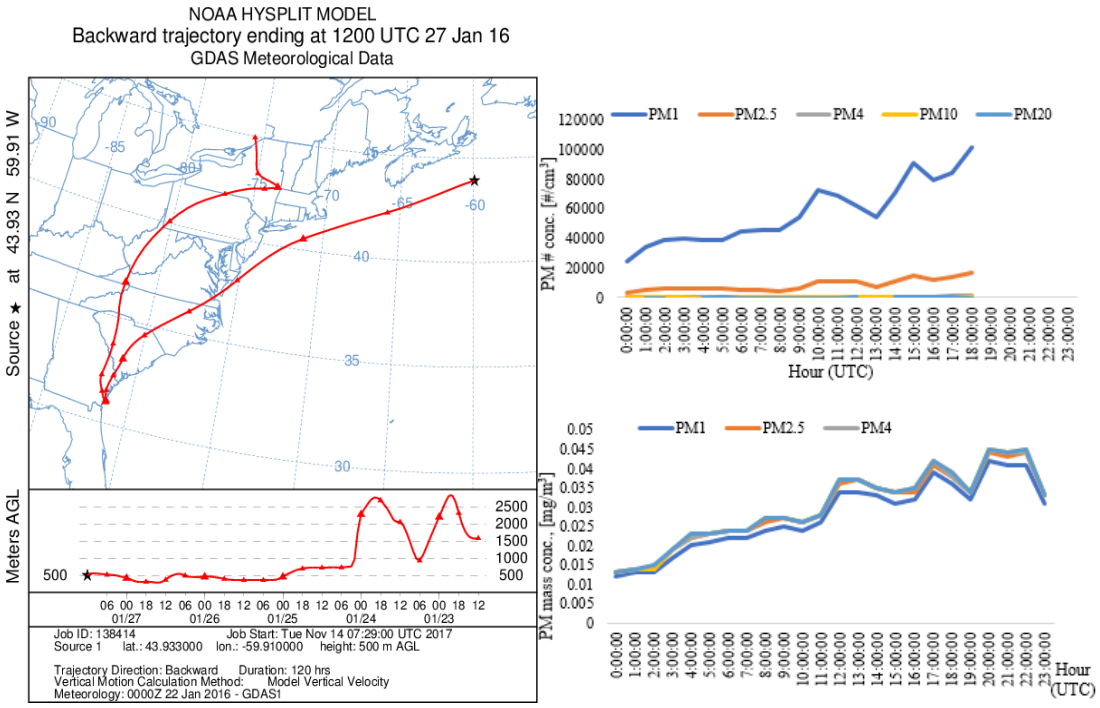

Figure 4-33. Jan. 27th spike: 120-hr air mass back trajectory (left), hourly PM number conc. (right top) and mass concentration (right bottom).

From hourly mean PM concentration plot shown in Figure 4-33, it can be seen that the PM mass and number concentration were increasing through the day till midnight. In 120-hr air mass back trajectory (Figure 4-33 left panel), it shows that the air mass originating in NE US, moving southward and then northeast passing industrial NE US again before landing at Sable Island. Aforementioned, Pennsylvania, New York, and port areas in Maryland have been identified as potential source regions for Halifax by Jeong et al. (2011) and Gibson et al. (2013), and are known to have many coal-fired power stations, which suggests this spike may be due to LRT from the continent. The air mass reaches an elevation of 2 000 m above the continent and drops to below 500 m over the Atlantic Ocean. The air mass appears to pass the Deep Panuke and Thebaud oil and gas (O&G) platforms near Sable Island, indicating O&G as an additional potential source. Locations of the offshore O&G platforms near Sable Island are shown in Error! Reference source not found.

Feb. 26th PM Spike

Figure 4-34 and Figure 4-35 below shows source apportionment analysis (hourly PM number and mass concentration plot, HYSLPIT air mass back trajectory on arrival date and daily phytoplankton abundancec) for PM spike occurred on Feb. 26th.

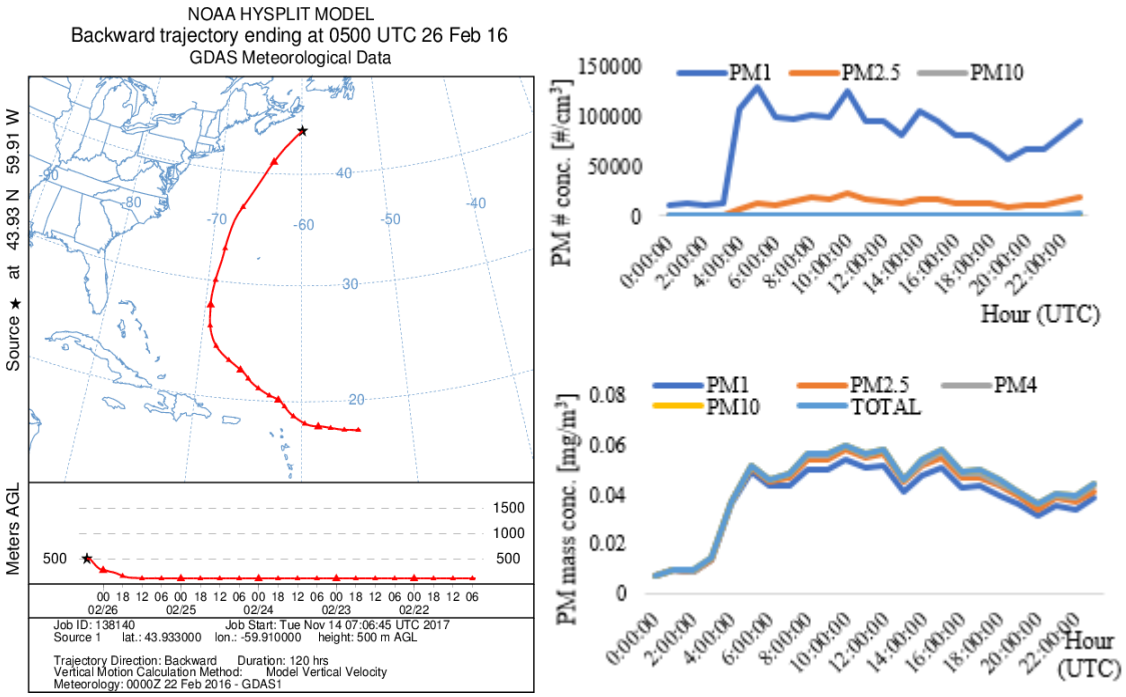

Figure 4-34. Feb. 26th spike: 120-hr air mass back trajectory (left), daily PM number (right top) and mass conc. hourly plot (right bottom).

In 120-hr air mass back trajectory (Figure 4-34 left panel), it shows that the air mass originated in marine area and moved northward to Sable Island. LRT source from industrial NEUS can be excluded. Also, the wind speed was 27.25 km/hr which is around the average level, so little wave action and wave-generated particles. PM_1 number counter was increasing abnormally and growing extremely higher than other size fractions; in the meantime, the mass of PM_1 was also abnormally lower than other size fraction, which indicate that PM_1 was likely to be dominated by UFP on that day. UFP 20-30, 30-50, 50-70, 70-100, 100-200 and 200-800 nm number counts reached 656, 535,

284, 294, 512 and 114 particle/cm^3, respectively, all are much higher than February average: 341, 284, 161, 170, 296 and 71 particle/cm^3, respectively. In addition, phytoplankton abundance in the region was also obtained and shown in Figure 4-35.

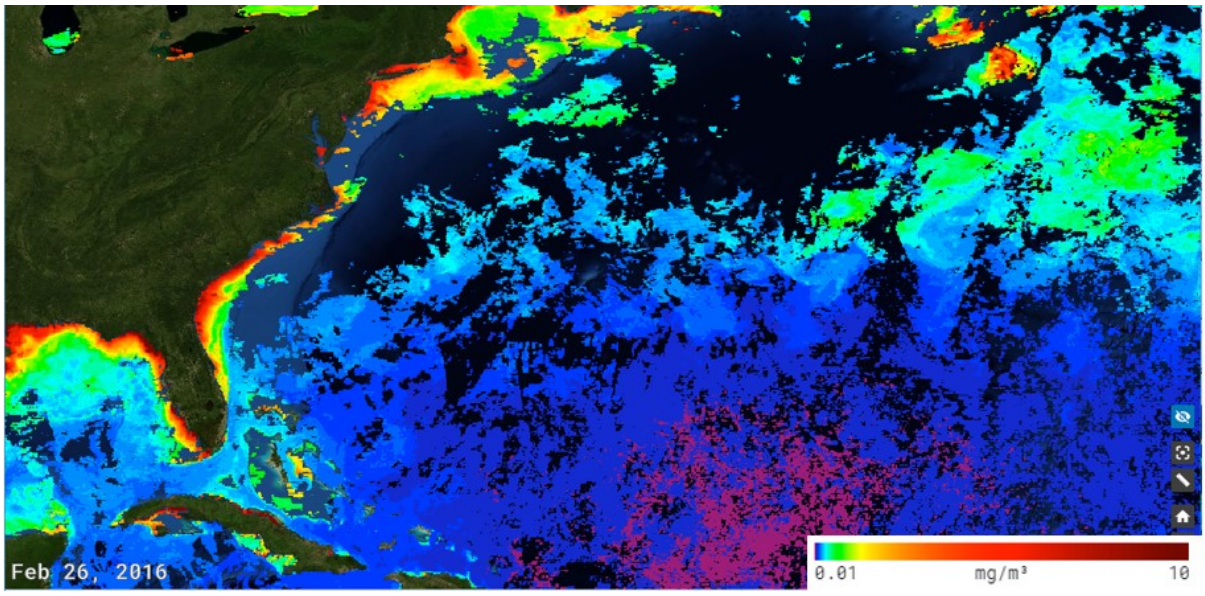

Figure 4-35. SOTO daily *Chl a* concentration in potential source region on February 25, 2016.

From Figure 4-35, it can be observed that daily *chl a* concentration was high along the air mass path to Sable Island, especially the altitude of airmass maintained at 500 m all the way. It is matching well with UFP number concentration shown in Figure 4-34. In this case, it can be assumed that the spike was likely to be the result of coagulation of UFP. based on PMF result, 49% of UFP 200-800 nm was within “Island Dust” factor so that it can be from surface dust too.

Apr. 9th PM Spike

Figure 4-36 below shows source apportionment analysis (hourly PM number and mass concentration plot, HYSLPIT air mass back trajectory on arrival date and daily phytoplankton abundancec) for PM spike occurred on Apr. 9th.

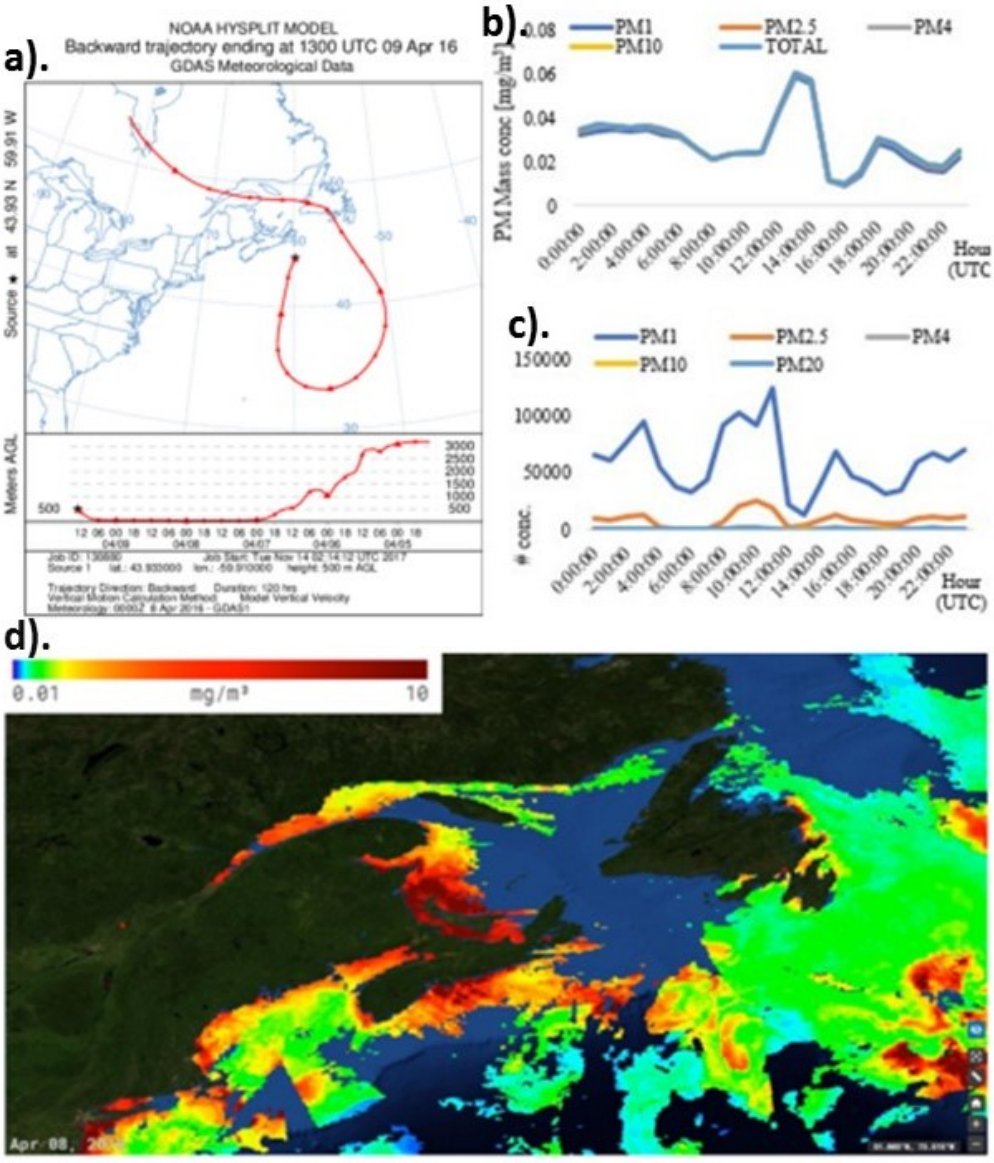

Figure 4-36. April 9th spike: a). 5-day air mass back trajectory; b). hourly PM mass concentration; c). hourly PM number concentration; and d). SOTO daily *chl a* concentration around Sable Island.

In Figure 4-36 a). HYSPLIT 5-day air mass back trajectory shows that the air mass originated from the North area which is a relatively clean area. PM mass concentration (Figure 4-36 b)) shows that PM in each size fraction are consistent with each other, indicating that the source can be from island surface dust or ocean. Weather data was unavailable on that day so, it's hard to determine if it is windy. The air mass on that day was at the latitude of 500 meters, which is low, so it can be from the mixture of ocean emission and surface dust. However, to construct a more accurate conclusion, more details are needed to be specified such as wind speed and weather condition as well as anthropogenic activities on the island.

4.3 Intra-study Comparison & Discussion

4.3.1 Seasonal variation

p-value was investigated for PM in all size fractions (Table 4-9) to determine the seasonal variance in each size fraction with 95% confidence interval. In this study, seasons were divided in the following way: Spring: April, May, and June; Summer: July, August and September; Fall: October, November and December; Winter: January, February and March. p-value < 0.05 means there is a significant difference among four seasons; while p-value > 0.05 means there is no significant difference among four seasons.

Table 4-9. p-value for PM all size fraction seasonal variance

	Size fractions	**p-value**
UFP # concentration	**20-30 nm**	0
	30-50 nm	0
	50-70 nm	0
	70-100 nm	0
	100-200 nm	0
	200-800 nm	0
PM # concentration	**PM_1**	0.01
	$PM_{2.5}$	0
	PM_4	0.053
	PM_{10}	0.086
	PM_{20}	0.023
PM Mass concentration	**PM_1**	0.326
	$PM_{2.5}$	0.266
	PM_4	0.257
	PM_{10}	0.257
	TSP	0.258

As can be seen in Table 4-9, for all UFP size fractions, p = 0, which means all four seasons are different from each other in each size fraction. It is because that UFP have smaller sizes and exist as clusters, so their concentrations change most of the time. While coarse PM are from break-ups of large solids or liquids, therefore they are more stable compared to clusters. Also, for fine particles (accumulation mode particles), they tend to exist longer than other particles as they are harder to be removed from the atmosphere (Seinfeld & Pandis, 2016). Interestingly, p values for PM_1 and $PM_{2.5}$ number concentration are smaller than 0.05 which means they vary seasonally; in the meantime, p values for PM_1 and $PM_{2.5}$ mass concentration are larger than 0.05, which means they didn't have much variation among seasons. This can be due to UFP which were measured as PM_1 in fine particle mass and number concentration measurement. UFP tends to have seasonal variation and they account for most of number concentration in PM_1 and $PM_{2.5}$ (Hinds, 1999), but least of mass concentration (with fine particles accounting for most of mass concentration).

4.3.2 UFP number concentration vs. total VOC concentration

Monthly and seasonal comparison (Figure 4-37 & **Figure 4-38**) were assessed using 15-minute measurements, covering a full annual cycle, between UFP and total VOC concentration obtained by instruments mentioned a priori.

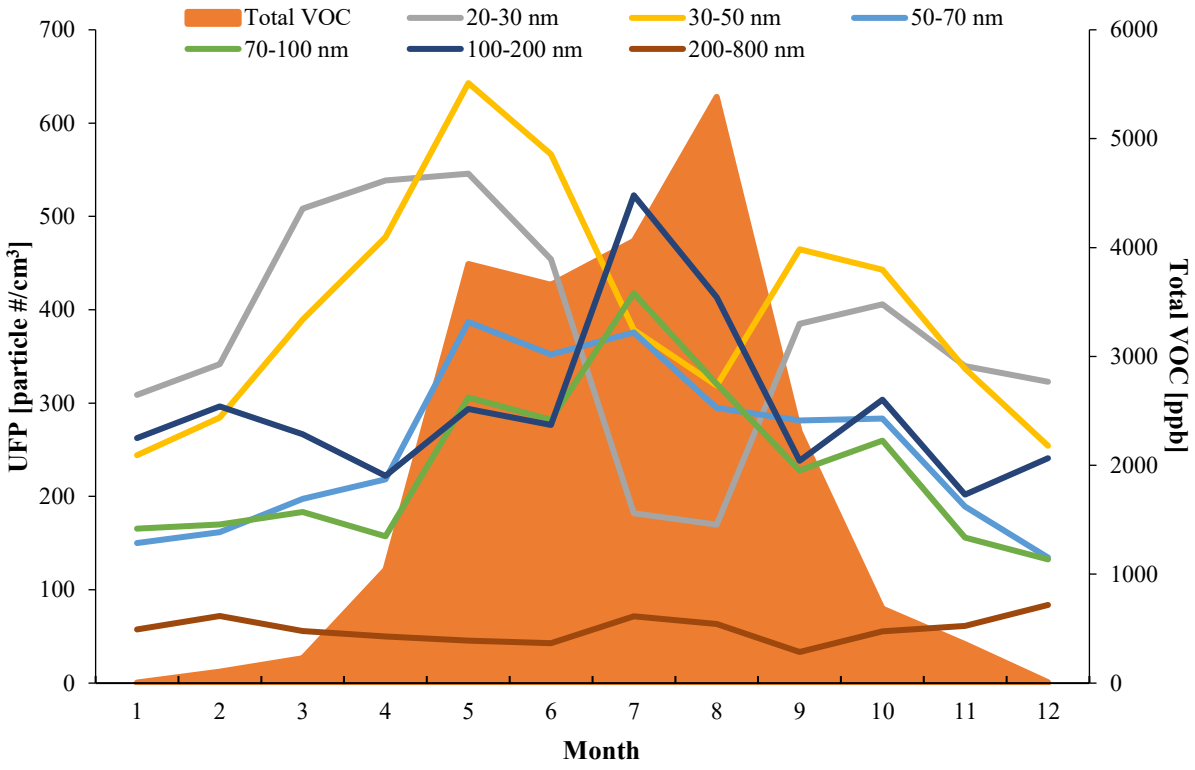

Figure 4-37. Monthly mean UFP number concentration (particle #/cm^3) vs. mean monthly VOC concentration (ppb) on Sable Island in 2016.

Figure 4-37 shows the mean monthly UFP number concentration and VOC concentration. Line represents each UFP size fraction and light orange area indicates VOC concentration. From the chart, it can be seen that 20-30 and 30-50 nm UFP were increasing in April, May, September and October, the two peaks occurred in May and September. 50-70 nm UFP began to increase in April and lasted until August. 70-100 nm UFP began to increase in April and reached peak in May, July and October. 100-200 nm

UFP didn't boost until July and then diminished quickly in August and September, and then reached a minor peak in October. 200-800 nm UFP trend was too low to be seen clearly in this chart but were shown in the following section. The total VOC concentration boosted in April and continued to increase through summer until it reached its maximum in August, then it diminished quickly afterwards. A seasonal overview of seasonal mean UFP number concentration and total VOC concentration was shown below in Figure 4-38. The reason why VOC doesn't match UFP can also be that several studies have shown that (Coe et al., 2000; Vaattovaara et al., 2006) particles smaller than 10 nm have been detected frequently in marine air mass, so this particle can be associated with VOC as they followed the trend of VOC concentration in the daytime, 30 - 90 min after the UV solar flux increased, their concentration increased sharply, then by early afternoon, concentration returned to background concentration.

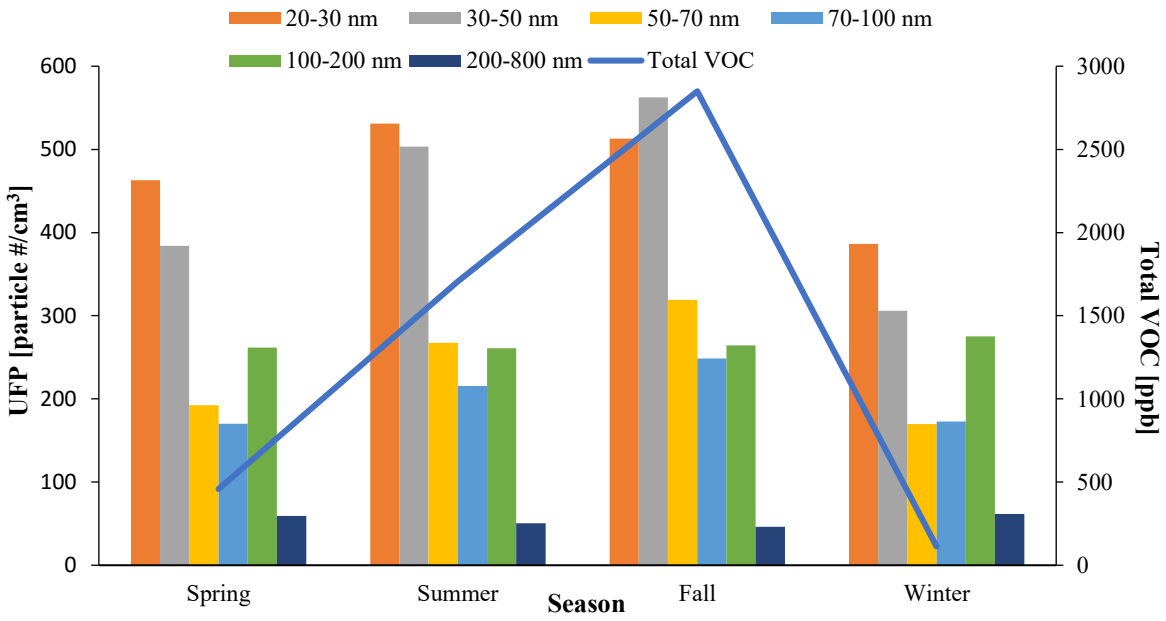

Figure 4-38. Seasonal mean UFP number concentration (particle #/cm^3) vs. mean seasonal total VOC concentration (ppb) on Sable Island in 2016.

Figure 4-38 reveals the mean seasonal trends of UFP number counter and total VOC concentration calculated at a temporal resolution of 15 minutes. It can be seen that total VOC seasonal mean concentration matches well with UFP seasonal trends. The overall seasonal growth of total VOC and UFP number matches, total VOC concentration began to increase in February and decrease in November which is the same as UFP number concentration. In particular, VOC matches well with UFP 100-200 nm. It is likely that UFP 100-200 nm is the coagulation products of both 20-30 nm and 30-50 nm UFP which is assumed to be the gas-to-particle conversion product from VOCs. However, when looking at a monthly variance, the total VOC concentration and UFP number does not match very well, it can be due to several reasons; firstly, there are still other VOCs coming out from either marine (halocarbons or isoprene) area or continental flows; secondly, due to instrument malfunctioning in August, which is the month that VOC reaches the maximum, UFP data is not available, resulting in a relatively low and inaccurate average value for August. Because of reasons above, chlorophyll-a concentration was investigated and used to run correlation test with UFP concentration in the following section.

4.3.3 UFP number concentration vs chlorophyll-a concentration

Correlation between UFP and chlorophyll-a concentration was also assessed. Monthly mean UFP number concentration was calculated from 15-minute measurement on Sable Island in 2016; the monthly mean chlorophyll-a concentration was retrieved from MODIS satellite observation via Giovanni data analysis system. Pearson's correlation test was also conducted in RStudio to show how they correlate with each other statistically. Figure 4-39 provides the comparison of monthly mean *chl a* concentration and UFP number concentration trends.

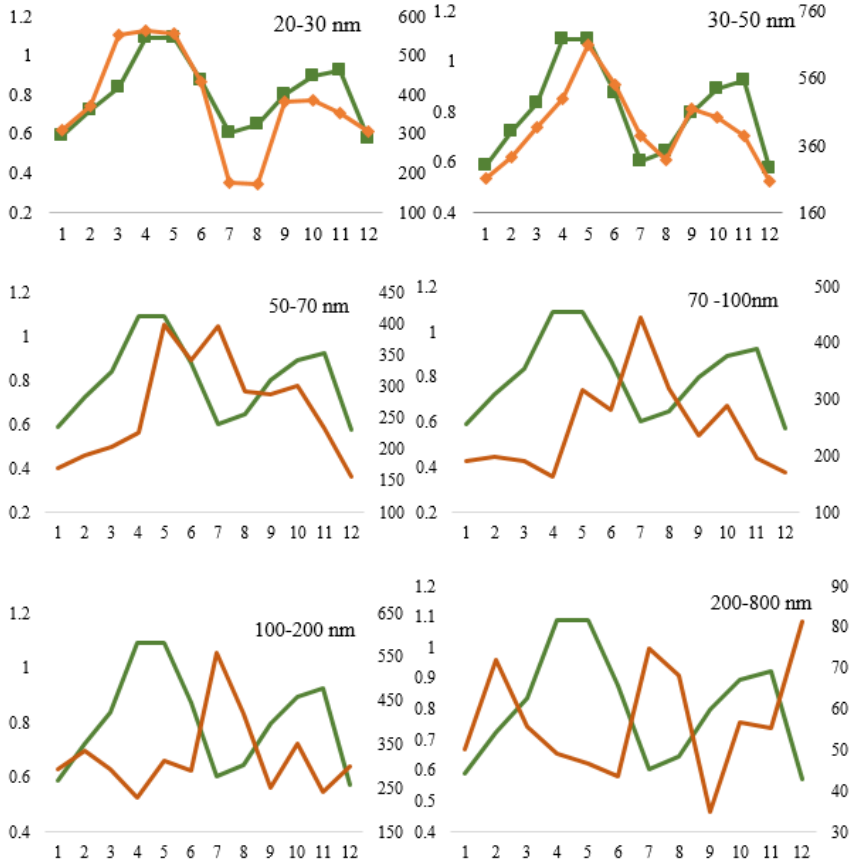

Figure 4-39. Comparison of monthly mean chlorophyll-a concentration and UFP (20-800 nm). Green line represents chlorophyll-a concentration, orange line represents different UFP sizes. Left vertical axis is chl a concentration [mg/m^3], right vertical axis is UFP number counter [$\#/cm^3$], horizontal axis shows month in number.

In Figure 4-39, it reveals that 20-30 nm and 30-50 nm UFP number concentration trend matches very well with *chl a* concentration. They both have a major bloom in April and May and a second peak in October. Also interestingly, 100-200 nm and 200-800 nm UFP have very different trend to *chl a* concentration. In August, when *chl a* reached the trough the 100-800 UFP number counter had a bloom. A correlation test was run between *chl a* concentration and each UFP size fraction number concentration and shown in Figure 4-40.

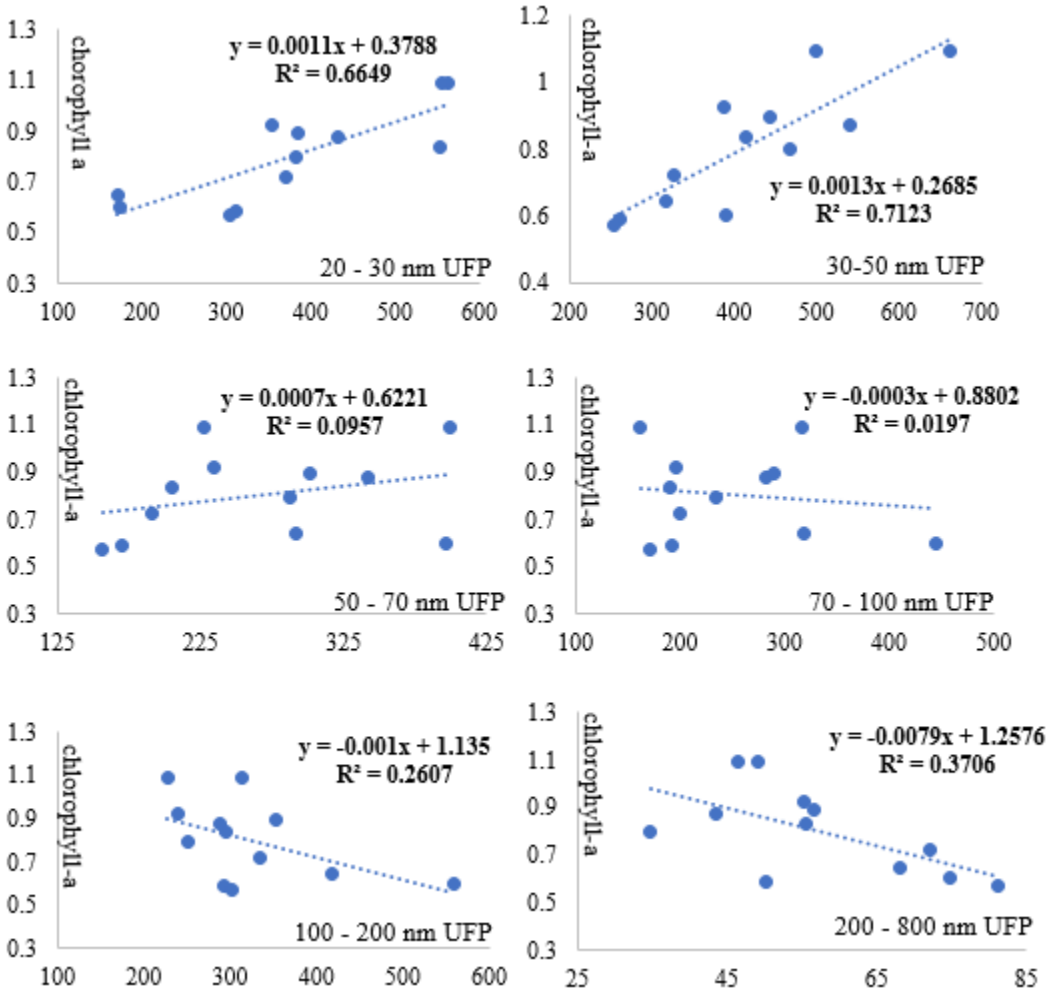

Figure 4-40. Correlation tests between UFP number concentration for default size fractions versus chlorophyll-a monthly mean concentration.

It can be seen in Figure 4-40 that 20-30 nm and 30-50 nm UFP have the two highest R^2 value among six size fractions (0.6649 and 0.7123, respectively). In this case, 20-50 nm UFP are highly positively correlated to *chl a* concentration, and 200-800 nm UFP are negatively correlated to *chl a* concentration. This test result agrees with Pearson correlation test results shown in Table 4-10.

Table 4-10. Summary of correlation tests for UFP all size fractions and chlorophyll-a

Size fractions	Pearson correlation	p-value	R^2 value
20-30nm	0.815	0.01	0.6649
30-50 nm	0.844	0.01	0.7123
50-70 nm	0.309	0.328	0.0957
70-100 nm	-0.140	0.664	0.0197
100-200 nm	-0.511	0.09	0.2607
200-800 nm	-0.609	0.036	0.3706

Pearson test shown in Table 4-10 reveals good agreements with correlation tests shown in Figure 4-40**,** 20-30 nm and 30-50 nm UFP had the highest Pearson coefficient (0.815 and 0.844), showing the strong positive correlation between 20-50 nm UFP and phytoplankton abundance; in the meantime, 200-800 nm UFP has the most negative Pearson coefficient (-0.609), showing the strong negative correlation between 200-800 nm UFP and *chl a* concentration.

To sum up, Figure 4-39 presents the visual comparison of monthly chlorophyll-a concentration and UFP number concentration trend in 12 months. It shows good agreement between the *chl a* concentration and UFP (20-30 nm and 30-50 nm) number

concentration, with significant correlation between the two variables (R^2 = 0.815 and 0.844) (Figure 4-39). Apart from these two size fractions, other UFP size fractions show weak correlation with chlorophyll-a concentration; but interestingly, UFP 200-800 nm has a quite strong negative correlation with chlorophyll-a concentration. (Figure 4-40 & Table 4-10), this can be result of coagulation of smaller size UFP (20-50 nm) which are from VOC from phytoplankton. This result shows some similarity to previous studies (Craig et al., 2015; Shadwick et al., 2011), shown in Figure 4-41.

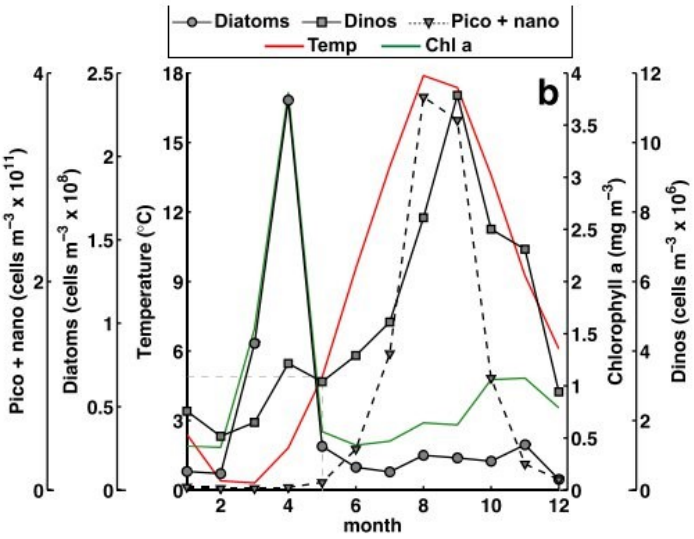

Figure 4-41. Seasonal cycle of temperature, *chl a*, diatoms, pico- & nanophytoplankton (Craig et al., 2015).

Figure 4-41 provides the annual cycle of diatoms, nanophytoplankton (nano), picophytoplankton (pico), pico and nano combined (pico+ nano) and dinoflagellates (dinos) concentrations measured in Bedford Basin (Craig et al., 2015). In the plot, it can be seen that diatoms concentration began to boost in March and reached the peak in April, then diminished after that; pico+nano phytoplankton didn't grow until July and June, then reached the peak in August and September. There is a variation in peak month between this study and Craig et al., 2015 study. This may be caused by the fact that

monthly mean *chl a* concentration used in this study was calculated over a large area (including the Labrador Sea and Gulf of St. Lawrence) that extends into northern waters where the spring bloom occurs later in the season. The spatial averaging may have resulted in a peak that occurred later in the season and may, in large part, explain the disparity in spring peaks compared with the coastal and shelf sites studied by Craig et al., 2015. Visual comparison between total VOC and *chl a* was shown in Figure 4-42.

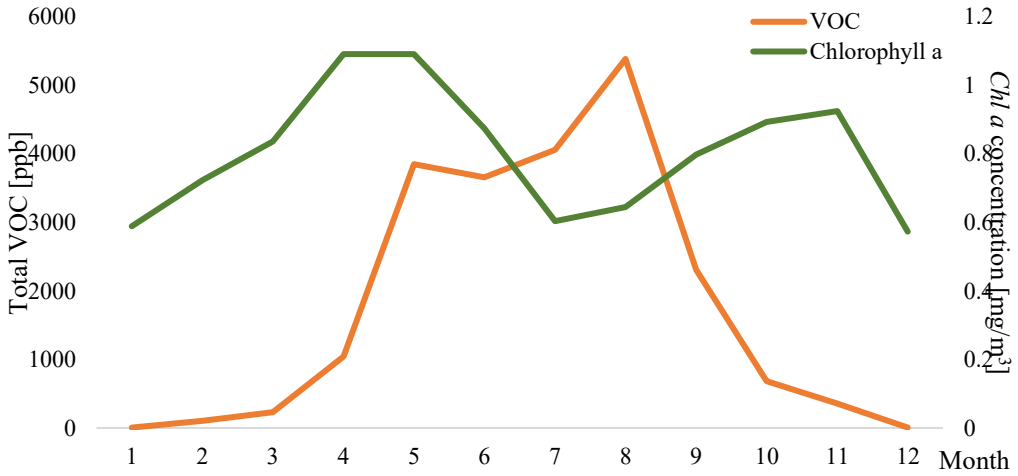

Figure 4-42. Monthly mean *chl a* concentration (mg/m^3) in marine around Sable Island vs. mean monthly VOC concentration (ppb).

As can be seen in Figure 4-42, the monthly trends are not matching well. However, both of them began to increase in March. It is because that chlorophyll-a is the representative of phytoplankton but total VOC can be from almost everything in the sea. Not only phytoplankton are releasing VOC but also other biomass such as zooplankton and fish. To summarize, UFP 20-50 nm trends coincided with *chl a* concentration, but the total VOC concentration did not; it can be due to VOC released from phytoplankton (DMS) is a major contributor to gas-to-particle conversion but some other marine VOCs are not.

4.4 Comparison with other ultrafine particle studies

Brace et al., 2014 found outdoor Halifax UFP number concentrations ranging from 7902 to 14,105 #/cm^3. This compares with the UFP range observed on Sable Island of 666 #/cm^3. The huge difference is because Brace conducted the measurement in Halifax urban area where has high population and anthropogenic activities while Sable Island barely has anthropogenic activities.

PM10 mass concentration on Sable Island was compared with a PM characteristic study conducted at Cape Verde atmospheric station in 2007. During 14th May – 14th July, 2016, on Sable Island, PM10 = 12.8±6.1 (4.2:34.1 μg/m^3); during 14th May – 14th July, 2007, at Cape Verde station, PM10 mass ranging from 15 to 332 μg/m^3. The maximum PM10 mass concentration in Cape Verde is much higher, it happened during windy days large amount of dust was brought in from desert Sahara. Apart from mineral dust, 60% of 0.05-0.14 μm particles were organic matter, 10% were sulfate, they were both from ocean biogenic emissions. On Sable Island, 90% of 0.05-0.2 μm particles were from ocean biogenic emissions. The higher percentage from ocean on Sable Island is because, compared to Cape Verde, it is more isolated and clean.

Another study conducted by Yoon et al. in 2007 showed the same interest and similar results that marine secondary biogenic organic compounds dominate PM in nucleation modes. In Yoon et al., 2007 study, particles in Aitken mode was <0.1 μm and accumulation mode was 0.1-0.5 μm; while in thesis, particles in Aitken mode was 20-50 μm and accumulation mode was 50-200 μm. Seasonal variation for size distribution, the Aitken mode particles increased from 0.031 μm in winter to 0.049 μm in summer, particle number increased from 137 /cm^3 to 327 /cm^3; the accumulation mode increased

from 0.103 μm in winter to 0.177 μm in summer, particle number increase from 117 /cm^3 to 142 /cm^3 (Yoon et al., 2007). In this study, the Aitken mode particles increased from 0.045 μm in winter to 0.053 μm in summer, particle number increased from 609 /cm^3 to 674 /cm^3, the accumulation mode increased from 0.193 μm in winter to 0.214 μm in summer, particle number increased from 669 /cm^3 to 1113 /cm^3. Values vary due to different year, location and instruments, but the trends remain the same. Moreover, in the study conducted by Yoon et al., the seasonal variation in phytoplankton bloom from NW to NE was revealed, as well as the significant correlation between marine particles with the size below 0.5 μm and phytoplankton activities.

Figure 60 below shows another ultrafine particle variation study conducted in Mace Head during May 17th – May 20th, 1994. The relationships between UFP and UVA radiation and tides were investigated in the study. UFP number concentration and diurnal variation in Mace Head and Sable Island were compared.

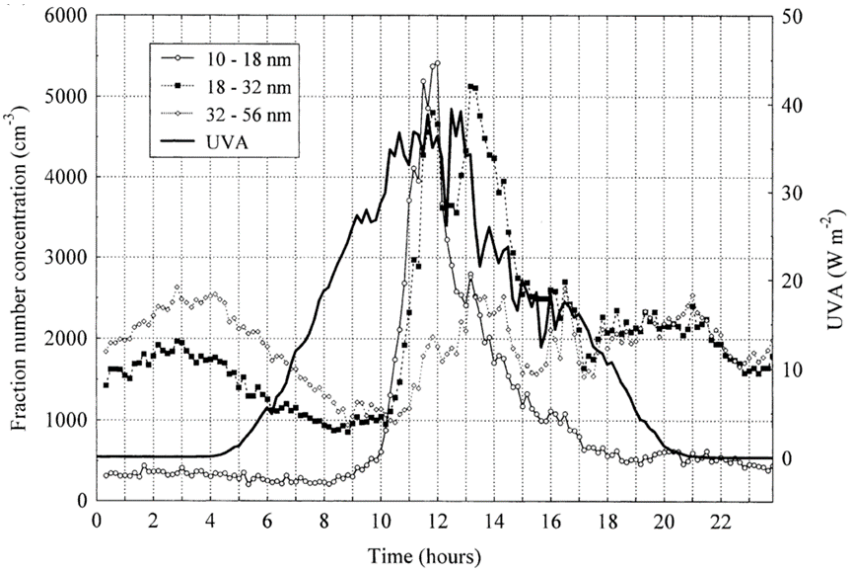

Figure 4-43. Mean fraction number concentrations, UVA radiation, and tide height categorized by time of day over May 17th – May 20th, 1994 (Vana, Jennings, Kleefeld, Mirme, & Tamm, 2002).

It can be seen from Figure 4-43 that UVA didn't increase until 5 am, which is earlier than the time of sunrise; five hours after UVA increase, 10-18 nm particles began to increase and reached maximum (5500 /cm^3) in 4 hours and maintained for one hour; then half hour after 10-18 nm began to increase, 18-32 nm particles began to increase and reached maximum (5000 /cm^3) about an hour after 18-32 nm peak; 2 hours after 18-32 nm began to increase, 32-56 nm particles began to increase and reached maximum (2750 /cm^3) in two hours. 4-day period mean particle number concentration during May 17th – May 20th on Sable Island was shown in Figure 4-44.

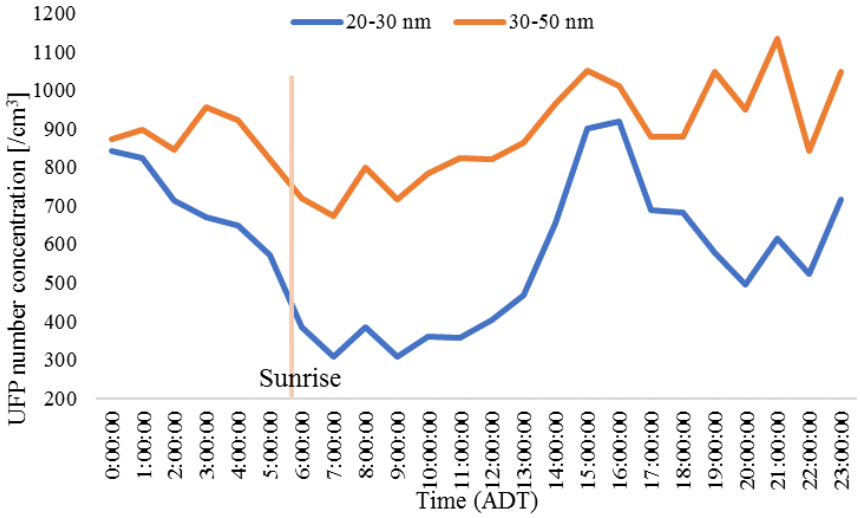

Figure 4-44. Mean fraction number concentration by time of day during May 17-20.

It can be seen in Figure 4-44 that the sunrise time on Sable Island was around 5:45 am, almost same as Mace Head. Then, 5 hours later around 11 am, 20-30 nm and 30-50 nm particles began to increase until 15:00 they reached maximum (901 and 1050 /cm^3, respectively). The time difference between sunrise and spike time were similar, but UFP number on Sable Island was much less than UFP at Mace Head. Firstly, it can be due to that Sable Island is a more isolated island while Mace Head is closer to living area.

Secondly, it was phytoplankton bloom season, freshly formed particles concentration is likely to be high. Last but not least, Mace Head had more active tide than Sable Island, which means tide fluctuated a lot in Mace Head, while water level around Sable Island didn't have much variation. The hourly mean water level in Halifax and Mace Head was calculated on the same period of time (May 17-20) in 2017, water level in Halifax ranged from 0.2 to 1 m, while Mace Head had water level ranged from -1.27 to 1.36 m. Low tide can stimulate the particle concentration events (Vana et al., 2002). Overall, the result of this study conducted on Sable Island in NW Atlantic Ocean matches well with results from some of study conducted in NE Atlantic Ocean, which proves the consistency of the study.

CHAPTER 5. Conclusion

5.1 Conclusion

The study found that the seasons were significantly different from each other in ultrafine and fine PM number concentrations; with the increase of sizes, p-value for seasonal variation increased: $p_{(UFP)} = 0$, $0 < p_{(PM1\text{-}2.5)} < 0.05$, $p_{(PM2.5\text{-}20)} > 0.05$. PM_1 and $PM_{2.5}$ number concentrations vary among seasons but interestingly, their mass concentration did not show much variation. This can be caused by UFP seasonal and diurnal variation. UFP was counted as PM_1 in PM measurement. When UFP number counters reach spike, their number concentration contributes the most to PM_1 number concentration, however, due to their much smaller sizes, they didn't contribute as much to PM_1 mass concentration as fine or coarse particles.

The chlorophyll-a and UFP concentrations were highly correlated but total VOCs were not correlating with UFP, therefore phytoplankton emissions as well as other biogenic emissions in the ocean can be the source of the UFP 20-50 nm. In this study, UFP 20-30 nm can be the coagulation products from nuclei mode UFP (<10 nm) which was freshly formed from VOC.

This study tentatively identified and quantified four main sources of size-resolved PM number concentration on Sable Island in 2016. The four size-resolved sources were apportioned: sea spray (2.2% of total UFP, 1.3% of total PM), secondary marine biogenic particles (78.2% of total UFP, 0.8% of total PM), LRT (4.4% of total UFP, 60.1% of total PM) and island surface dusts (15.2% of total UFP, 37.7% of total PM), where secondary marine biogenic particles were the dominant contributor to UFP and LRT was the dominant contributor to PM. The discovery of the close correlation between UFP (20-30

nm and 30-50 nm) and *chl a* ($R^2 = 0.815$ and $R^2 = 0.815$, respectively) is a significant enhancement in research of ocean-atmosphere cloud condensation nuclei formation and atmospheric modelling.

5.2 Recommendations

It is recommended that further study be conducted to gather data to investigate multi-year associations between phytoplankton VOC emissions and their influence on the formation of freshly formed UFP in the 20-30nm size range. It is recommended that future research incorporates both particle species and gaseous species to better understand the ocean-atmosphere interactions and formation of UFP that act as cloud condensation nuclei that are so import in terms of mediating climate. The results of this study will help with the analysis and interpretation of the NASA, NAAMES data collected during 2016.

References

Acker, J. G., & Leptoukh, G. (2007). Online analysis enhances use of NASA Earth science data. *Eos, Transactions American Geophysical Union*, *88*(2), 14–17. https://doi.org/10.1029/2007EO020003

Adventure Canada | Sable Island. (2017). Retrieved November 23, 2017, from http://www.adventurecanada.com/trip/sable-island-2017/

Barnett, T. C. (2016). *The Source Apportionment of Airborne Particulate Matter Composition on Sable Island, Nova Scotia, Canada*. Dalhousie University.

Bell, J. N. B., & Treshow, M. (2002). *Air pollution and plant life* (2nd ed. .). Chichester: Chichester : Wiley.

Beranek, J., Imre, D., & Zelenyuk, A. (2012). Real-time shape-based particle separation and detailed in situ particle shape characterization. *Analytical Chemistry*, *84*(3), 1459–1465. https://doi.org/10.1021/ac202235z

Beusse, R., Dunlap, C., Good, K., Hauck, E., Mcghee-lenart, R., & Narimatsu, J. (2013). *EPA Needs to Improve Air Emissions Data for the Oil and Natural Gas Production Sector* (Vol. P-0161). https://doi.org/13-P-0161

Boney, A. D. (Arthur D. (1989). *Phytoplankton* (2nd ed. .). London: London : Edward Arnold.

Brace, M. D., Stevens, E., Taylor, S., Butt, S., Sun, Z., Hu, L., … Gibson, M. D. (2014). `The air that we breathe?: assessment of laser and electrosurgical dissection devices on operating theater air quality. *Journal of Otolaryngology - Head & Neck Surgery = Le Journal D'oto-Rhino-Laryngologie et de Chirurgie Cervico-Faciale*, *43*(1), 39. https://doi.org/10.1186/PREACCEPT-7454522201323814

Brimblecombe, P. (1996). *Air composition and chemistry*. *Cambridge* (2nd ed. ., Vol. 11). Cambridge [Cambridgeshire] ; New York: Cambridge Cambridgeshire ; New York : Cambridge University Press. https://doi.org/10.1016/0160-9327(87)90266-3

Brook, R. D., Urch, B., Dvonch, J. T., Bard, R. L., Speck, M., Keeler, G., … Brook, J. R. (2009). Insights into the mechanisms and mediators of the effects of air pollution exposure on blood pressure and vascular function in healthy humans. *Hypertension (Dallas, Tex. : 1979)*, *54*(3), 659–667. https://doi.org/10.1161/HYPERTENSIONAHA.109.130237

Burkart, J., Willis, M. D., Bozem, H., Thomas, J. L., Law, K., Hoor, P., … Richard Leaitch, W. (2017). Summertime observations of elevated levels of ultrafine particles in the high Arctic marine boundary layer. *Atmospheric Chemistry and Physics*, *17*(8), 5515–5535. https://doi.org/10.5194/acp-17-5515-2017

Calde On-garcidu Nas, L., Reed, W., Maronpot, R. R., Hen Iquez-rol, C. A., Delgado-chavez, R., Calde, A., … Swenberg, J. A. (2004). Brain Inflammation and Alzheimer's-Like Pathology in Individuals Exposed to Severe Air Pollution. *Toxicologic Pathology*, *32*, 650–658. https://doi.org/10.1080/01926230490520232

Canada NS offshore Petroleum Board. (2013). Venture Thebaud. Retrieved November 8, 2017, from https://www.cnsopb.ns.ca/pdfs/sable_area_platforms.pdf

Charlson, M. E., Pompei, P., Ales, K. L., & MacKenzie, C. R. (1987). A new method of classifying prognostic comorbidity in longitudinal studies: Development and validation. *Journal of Chronic Diseases*, *40*(5), 373–383. https://doi.org/10.1016/0021-9681(87)90171-8

Coe, H., Williams, P. I., McFiggans, G., Gallagher, M. W., Beswick, K. M., Bower, K. N., & Choularton, T. W. (2000). Behavior of ultrafine particles in continental and marine air masses at a rural site in the United Kingdom. *Journal of Geophysical Research-Atmospheres*, *105*(D22), 26891–26905. https://doi.org/10.1029/2000jd900234

Cohen, A. J., Anderson, H. R., Ostro, B., Pandey, K. D., Krzyzanowski, M., Künzli, N., … Smith, K. (2005). The global burden of disease due to outdoor air pollution. *Journal of Toxicology and Environmental Health - Part A*, *68*(13–14), 1301–1307. https://doi.org/10.1080/15287390590936166

Collins, D. B., Burkart, J., Chang, R. Y.-W., Lizotte, M., Boivin-Rioux, A., Blais, M., … Abbatt, J. P. D. (2017). Frequent Ultrafine Particle Formation and Growth in the Canadian Arctic Marine Environment. *Atmospheric Chemistry and Physics Discussions*, (June), 1–31. https://doi.org/10.5194/acp-2017-411

Comero, S., Capitani, L., & Gawlik, B. M. (2009). *Positive Matrix Factorisation (PMF) An introduction to the chemometric evaluation of environmental monitoring data using PMF*. https://doi.org/10.2788/2497

Compounds, V. O., Devices, C., Sources, P., & Sources, N. (2007). *Characterization of Greenhouse Gas Emissions Involved in Oil and Gas Exploration and Production Operations*.

Craig, S. E., Thomas, H., Jones, C. T., Li, W. K. W., Greenan, B. J. W., Shadwick, E. H., & Burt, W. J. (2015). The effect of seasonality in phytoplankton community composition on CO 2 uptake on the Scotian Shelf. *Journal of Marine Systems*, *147*, 52–60. https://doi.org/10.1016/j.jmarsys.2014.07.006

Davidson, C. I., Phalen, R. F., & Solomon, P. A. (2005). Airborne particulate matter and human health: A review. *Aerosol Science and Technology*, *39*(8), 737–749. https://doi.org/10.1080/02786820500191348

Dockery, D. W. (2009). Health Effects of Particulate Air Pollution. *Annals of Epidemiology*, *19*(4), 257–263. https://doi.org/10.1016/j.annepidem.2009.01.018

Dockery, D. W., Pope, C. A., Xu, X., Spengler, J. D., Ware, J. H., Fay, M. E., … Speizer, F. E. (1993). An Association between Air Pollution and Mortality in Six U.S. Cities. *New England Journal of Medicine*, *329*(24), 1753–1759. https://doi.org/10.1056/NEJM199312093292401

Dohoo, C., Guernsey, J. R., Gibson, M. D., & Vanleeuwen, J. (2013). Impact of biogas digesters on cookhouse volatile organic compound exposure for rural Kenyan farmwomen. *Journal of Exposure Science and Environmental Epidemiology Advance Online Publication July*, *31*. https://doi.org/10.1038/jes.2013.42

Dohoo, C., Read Guernsey, J., Gibson, M. D., & Van Leeuwen, J. (2015). Impact of biogas digesters on cookhouse volatile organic compound exposure for rural Kenyan farmwomen. *Journal of Exposure Science and Environmental Epidemiology*, *25*(2), 167–174. https://doi.org/10.1038/jes.2013.42

Dominici, F., Peng, R., Bell, M., Pham, L., McDermott, A., Zeger, S., & Samet, J. (2006). Fine particulate air pollution and hospital admission for cardiovascular and respiratory diseases. *JAMA (Journal of the American Medical Association)*, *295*(10), 1127–1134. https://doi.org/10.1001/jama.295.10.1127.Fine

Duderstadt, K. A., Carroll, M. A., Sillman, S., Wang, T., Albercook, G. M., Feng, L., … Forbes, G. (1998). Photochemical production and loss rates of ozone at Sable Island, Nova Scotia during the North Atlantic Regional Experiment (NARE) 1993 summer intensive. *Journal of Geophysical Research-Atmospheres*, *103*(D11), 13531–13555. https://doi.org/10.1029/98JD00397

EPA. (2016). Health and Environmental Effects of Particulate Matter (PM). Retrieved November 4, 2017, from https://www.epa.gov/pm-pollution/health-and-environmental-effects-particulate-matter-pm

Fountoukis, C., Riipinen, I., Denier Van Der Gon, H. A. C., Charalampidis, P. E., Pilinis, C., Wiedensohler, A., … Pandis, S. N. (2012). Simulating ultrafine particle formation in Europe using a regional CTM: Contribution of primary emissions versus secondary formation to aerosol number concentrations. *Atmospheric Chemistry and Physics*, *12*(18), 8663–8677. https://doi.org/10.5194/acp-12-8663-2012

Fournier, R. O., Marra, J., Bohrer, R., & Det, M. Van. (1977). Plankton Dynamics and Nutrient Enrichment of the Scotian Shelf. *Journal of the Fisheries Research Board of Canada*, *34*(7), 1004–1018. https://doi.org/10.1139/f77-153

Friends of Sable Island Society | A Brief History of Sable Island. (2012). Retrieved November 21, 2017, from http://sableislandfriends.ca/?p=148

Fuzzi, S., Baltensperger, U., Carslaw, K., Decesari, S., Denier Van Der Gon, H., Facchini, M. C., … Gilardoni, S. (2015). Particulate matter, air quality and climate: Lessons learned and future needs. *Atmospheric Chemistry and Physics*, *15*(14), 8217–8299. https://doi.org/10.5194/acp-15-8217-2015

Gibson, M. D., Guernsey, J. R., Beauchamp, S., Waugh, D., Heal, M. R., Brook, J. R., … Terashima, M. (2009). Journal of the Air & Waste Management Association Quantifying the Spatial and Temporal Variation of Ground-Level Ozone in the Rural Annapolis Valley, Nova Scotia, Canada Using Nitrite-Impregnated Passive Samplers Quantifying the Spatial and Temporal V. *Journal of the Air & Waste Management Association*, *593*, 310–320. https://doi.org/10.3155/1047-3289.59.3.310

Gibson, M. D., Haelssig, J., Pierce, J. R., Parrington, M., Franklin, J. E., Hopper, J. T., … Ward, T. J. (2015). A comparison of four receptor models used to quantify the boreal wildfire smoke contribution to surface PM2.5 in Halifax, Nova Scotia during the BORTAS-B experiment. *Atmospheric Chemistry and Physics*, *15*(2), 815–827. https://doi.org/10.5194/acp-15-815-2015

Gibson, M. D., Heal, M. R., Bache, D. H., Hursthouse, A. S., Beverland, I. J., Craig, S. E., … Jones, C. (2009). Using Mass Reconstruction along a Four-Site Transect as a Method to Interpret PM10 in West-Central Scotland,United Kingdom. *Journal of the Air & Waste Management Association*, *59*(12), 1429–1436. https://doi.org/10.3155/1047-3289.59.12.1429

Gibson, M. D., Heal, M. R., Li, Z., Kuchta, J., King, G. H., Hayes, A., & Lambert, S. (2013). The spatial and seasonal variation of nitrogen dioxide and sulfur dioxide in Cape Breton Highlands National Park, Canada, and the association with lichen abundance. *Atmospheric Environment*, *64*, 303–311. https://doi.org/10.1016/j.atmosenv.2012.09.068

Gibson, M. D., Kundu, S., & Satish, M. (2013). Dispersion model evaluation of PM2.5, NOx and SO2 from point and major line sources in Nova Scotia, Canada using AERMOD Gaussian plume air dispersion model. *Atmospheric Pollution Research*, *4*(2), 157–167. https://doi.org/10.5094/APR.2013.016

Gibson, M. D., Pierce, J. R., Waugh, D., Kuchta, J. S., Chisholm, L., Duck, T. J., … Palmer, P. I. (2013). Identifying the sources driving observed PM2.5 temporal variability over Halifax, Nova Scotia, during BORTAS-B. *Atmospheric Chemistry and Physics*, *13*(14), 7199–7213. https://doi.org/10.5194/acp-13-7199-2013

Government of Canada. (2016). Environment and Climate Change Canada. Retrieved November 3, 2017, from https://ec.gc.ca/meteoaloeil-skywatchers/default.asp?lang=En&n=7884CDEA-1

Government of Canada, P. C. A.-S. A. P. (2014). Parks Canada - Internal Audit and Evaluation Documents. Retrieved from https://www.pc.gc.ca/leg/docs/pc/rpts/rve-par/88/index_e.asp

Ha, S., Sundaram, R., Louis, G. M. B., Nobles, C., Seeni, I., Sherman, S., & Mendola, P. (2017). Ambient air pollution and the risk of pregnancy loss: a prospective cohort study. https://doi.org/10.1016/j.fertnstert.2017.09.037

Hader, D., & Schafer, J. (1995). Photosynthetic Oxygen Production in Macroalgae and Phytoplankton under Solar Irradiation.

Halsey, K. H., Giovannoni, S. J., Graus, M., Zhao, Y., Landry, Z., Thrash, J. C., … de Gouw, J. (2017). Biological cycling of volatile organic carbon by phytoplankton and bacterioplankton. *Limnology and Oceanography*, *62*(6), 2650–2661. https://doi.org/10.1002/lno.10596

Hansen, J., Sato, M., Kharecha, P., & Von Schuckmann, K. (2011). Earth's energy imbalance and implications. *Atmospheric Chemistry and Physics*, *11*(24), 13421–13449. https://doi.org/10.5194/acp-11-13421-2011

Harrison, R. M. (1990). *Pollution : causes, effects, and control.* (3rd ed. .). Cambridge: Cambridge : Royal Society of Chemistry Information Services. Retrieved from http://silk.library.umass.edu/login?url=http://search.ebscohost.com/login.aspx?direct=true&db=cat06087a&AN=umass.000759019&site=eds-live&scope=site

Hayes, A. (2014). *Source Apportionment of the Air Quality on Sable Island*. Dalhousie University.

Henson, S. A., Dunne, J. P., & Sarmiento, J. L. (2009). Decadal variability in North Atlantic phytoplankton blooms. *Journal of Geophysical Research: Oceans*, *114*(4), 1–11. https://doi.org/10.1029/2008JC005139

Hillemann, L., Zschoppe, A., & Caldow, R. (2007). *Aerosol mobility spectrometry based on diffusion charging*. Retrieved from http://www.tsi.com/uploadedFiles/_Site_Root/Products/Literature/Posters/UFIPOLNET_EAC07_Hillemann_lecture.pdf

Hinds, W. C. (1999). *Aerosol technology: Properties, Behavior, and Measurement of Airborne Particles. Wiley-Interscience Publication* (2nd ed. ., Vol. 70). New York: New York : Wiley. https://doi.org/10.1016/0021-8502(83)90049-6

Hobbs, P. V. (1993). *Aerosol--cloud--climate interactions*. San Diego: San Diego : Academic Press.

Hondula, D. M., Sitka, L., Davis, R. E., Knight, D. B., Gawtry, S. D., Deaton, M. L., … Stenger, P. J. (2010). A back-trajectory and air mass climatology for the Northern Shenandoah Valley, USA. *International Journal of Climatology*, *30*(4), 569–581. https://doi.org/10.1002/joc.1896

Huang, Y., Shen, H., Chen, H., Wang, R., Zhang, Y., Su, S., … Tao, S. (2014). Quantification of global primary emissions of PM<inf>2.5</inf>, PM<inf>10</inf>, and TSP from combustion and industrial process sources. *Environmental Science and Technology*, *48*(23), 13834–13843. https://doi.org/10.1021/es503696k

IPCC. (2014). *Climate Change 2013 - The Physical Science Basis*. *Climate Change 2013: The Physical Science Basis. Contribution of Working Group I to the Fifth Assessment Report of the Intergovernmental Panel on Climate Change*. https://doi.org/10.1017/CBO9781107415324

Jabre, L. (2017). *Source Sector Analysis of Marine and Other Volatile Organic Compounds on Sable Island, Nova Scotia, Canada*. Dalhousie University.

Jacob, C., Field, B. D., Jin, E. M., Bey, I., Li, Q., Logan, J. A., … Jacob, D. J. (2002). Atmospheric budget of acetone. *Journal of Geophysical Research*, *107*(D10). https://doi.org/10.1029/2001JD000694

Jeong, C., McGuire, M. L., Herod, D., Dann, T., Dabek–Zlotorzynska, E., Wang, D., … Evans, G. (2011). Receptor model based identification of PM2.5 sources in Canadian cities. *Atmospheric Pollution Research*, *2*(2), 158–171. https://doi.org/10.5094/APR.2011.021

Jones, A. M., Harrison, R. M., & Baker, J. (2010). The wind speed dependence of the concentrations of airborne particulate matter and NOx. *Atmospheric Environment*, *44*(13), 1682–1690. https://doi.org/10.1016/j.atmosenv.2010.01.007

Kearns, J. (BHP P., Armstrong, K. (Chevron), Shirvill, L. (Shell), Garland, E. (Elf), Simon, C. (Texaco), & Monopolis, J. (Exxon). (2000). *Flaring & venting in the oil & gas exploration & production industry*. *IOGP Publications*. https://doi.org/Report No. 2.79/288

Kim, K. D., & Lee, E. J. (2005). Potential tree species for use in the restoration of unsanitary landfills. *Environmental Management*, *36*(1), 1–14. https://doi.org/10.1007/s00267-004-1089-3

Kulmala, M., Dal Maso, M., Mäkelä, J. M., Pirjola, L., Väkevä, M., Aalto, P., … O'Dowd, C. D. (2001). On the formation, growth and composition of nucleation mode particles. *Tellus, Series B: Chemical and Physical Meteorology*, *53*(4), 479–490. https://doi.org/10.3402/tellusb.v53i4.16622

Kulmala, M., Vehkamäki, H., Petäjä, T., Dal Maso, M., Lauri, A., Kerminen, V. M., … McMurry, P. H. Formation and growth rates of ultrafine atmospheric particles: A review of observations, 35 Journal of Aerosol Science § (2004). Pergamon. https://doi.org/10.1016/j.jaerosci.2003.10.003

Mahowald, N., Ward, D. S., Kloster, S., Flanner, M. G., Heald, C. L., Heavens, N. G., … Chuang, P. Y. (2011). Aerosol Impacts on Climate and Biogeochemistry. *Annual Review of Environment and Resources*, *36*(1), 45–74. https://doi.org/10.1146/annurev-environ-042009-094507

McNeilly, J. D., Heal, M. R., Beverland, I. J., Howe, A., Gibson, M. D., Hibbs, L. R., … Donaldson, K. (2004). Soluble transition metals cause the pro-inflammatory effects of welding fumes in vitro. *Toxicology and Applied Pharmacology*, *196*(1), 95–107. https://doi.org/10.1016/j.taap.2003.11.021

MODIS Web. (2015). Retrieved August 1, 2017, from http://modis.gsfc.nasa.gov/sci_team/pubs/abstract_new.php?id=19776

Monitoring, A. Q. (2014). *Model 3031200 Environmental Sampling System Field Setup with Model 3031 Ultrafine Particle Monitor*. Retrieved from http://www.tsi.com/uploadedFiles/_Site_Root/Products/Literature/Application_Notes/UFP-002_Model_3031200_Env_Samp_Sys.pdf

Monks, P. S., Granier, C., Fuzzi, S., Stohl, A., Williams, M. L., Akimoto, H., … von Glasow, R. (2009). Atmospheric composition change - global and regional air quality. *Atmospheric Environment*, *43*(33), 5268–5350. https://doi.org/10.1016/j.atmosenv.2009.08.021

Moore, R. M., Oram, D. E., & Penkett, S. A. (1994). Production of isoprene by marine phytoplankton cultures. *Geophysical Research Letters*, *21*(23), 2507–2510. https://doi.org/10.1029/94GL02363

MSFC, J. W. : (2009). NASA - Giovanni: An Easier Way to Visualize Earth Science Data. Retrieved November 7, 2017, from http://www.nasa.gov/audience/foreducators/9-12/features/giovanni-an-easier-way.html

NASA Ocean Biology Processing Group. (2015). MODIS-Aqua Level 3 Binned Chlorophyll Data Version 2014. Greenbelt, MD, USA: NASA Ocean Biology DAAC. https://doi.org/10.5067/AQUA/MODIS/L3B/CHL/2014

NOAA. (2017). Visible Infrared Imaging Radiometer Suite (VIIRS). Retrieved August 1, 2017, from https://ncc.nesdis.noaa.gov/VIIRS/

Norris, G., Duvall, R., Brown, S., & Bai, S. (2014). EPA Positive M atrix Factorization (PMF) 5.0 Fundamentals and User Guide, 136. https://doi.org/EPA/600/R-14/108

O'Dowd, C., Ceburnis, D., Ovadnevaite, J., Vaishya, A., Rinaldi, M., & Facchini, M. C. (2014). Do anthropogenic, continental or coastal aerosol sources impact on a marine aerosol signature at Mace Head? *Atmospheric Chemistry and Physics*, *14*(19), 10687–10704. https://doi.org/10.5194/acp-14-10687-2014

Palmer, P. I., Parrington, M., Lee, J. D., Lewis, A. C., Rickard, A. R., Bernath, P. F., … Young, J. C. (2013). Quantifying the impact of BOReal forest fires on Tropospheric oxidants over the Atlantic using Aircraft and Satellites (BORTAS) experiment: Design, execution and science overview. *Atmospheric Chemistry and Physics*, *13*(13), 6239–6261. https://doi.org/10.5194/acp-13-6239-2013

Pelucchi, C., Negri, E., Gallus, S., Boffetta, P., Tramacere, I., & La Vecchia, C. (2009). Long-term particulate matter exposure and mortality: a review of European epidemiological studies. *BMC Public Health*, *9*, 453. https://doi.org/10.1186/1471-2458-9-453

Pope III, C. A., Burnett, R. T., Thun, M. J., Calle, E. E., Krewski, D., Ito, K., & Thurston, G. D. (2002). Lung Cancer, Cardiopulmonary Mortality, and Long-term Exposure to Fine Particulate Air Pollution. *JAMA*, *287*(9), 1132. https://doi.org/10.1001/jama.287.9.1132

Querol, X., Alastuey, A., Ruiz, C. R., Artinãno, B., Hansson, H. C., Harrison, R. M., … Schneider, J. (2004). Speciation and origin of PM10 and PM2.5 in selected European cities ARTICLE IN PRESS. *Atmospheric Environment*, *38*, 6547–6555. https://doi.org/10.1016/j.atmosenv.2004.08.037

Quinn, P. K., & Bates, T. S. (2011). The case against climate regulation via oceanic phytoplankton sulphur emissions. *Nature*, *480*(7375), 51–56. https://doi.org/10.1038/nature10580

Ramadan, Z., Song, X. H., & Hopke, P. K. (2000). Identification of sources of phoenix aerosol by positive matrix factorization. *Journal of the Air and Waste Management Association*, *50*(8), 1308–1320. https://doi.org/10.1080/10473289.2000.10464173

Rosselli, R., Fiamma, M., Deligios, M., Pintus, G., Pellizzaro, G., Canu, A., … Cappuccinelli, P. (2015). Microbial immigration across the Mediterranean via airborne dust. *Scientific Reports*, *5*(1), 16306. https://doi.org/10.1038/srep16306

Sable Aviation - Aircraft Charter to Sable Island. (2017). Retrieved November 23, 2017, from http://www.sableaviation.ca/

Saltzman, E. S., & Cooper, W. J. (1989). *Biogenic Sulfur in the Environment*. *Environmental Chemistry*. Washington, DC: Washington, DC : American Chemical Society. https://doi.org/10.1021/bk-1989-0393

Seinfeld, J., & Pandis, S. (2016). *Atmospheric Chemistry and Physics: From Air Pollution to Climate Change* (Third edit). Hoboken, New Jersey: John Wiley & Sons, Inc. Retrieved from Chemistry%5Cnand%5CnPhysics-1709322496/Atmospheric%5CnPhysics.pdf

Shadwick, E. H., Thomas, H., Azetsu-Scott, K., Greenan, B. J. W., Head, E., & Horne, E. (2011). Seasonal variability of dissolved inorganic carbon and surface water pCO2 in the Scotian Shelf region of the Northwestern Atlantic. *Marine Chemistry*, *124*(1–4), 23–37. https://doi.org/10.1016/j.marchem.2010.11.004

Siegel, D. A., Doney, S. C., & Yoder, J. A. (2002). The North Atlantic Spring Phytoplankton Bloom and Sverdrup's Critical Depth Hypothesis. *Science*, *296*(5568), 730 LP-733. Retrieved from http://science.sciencemag.org/content/296/5568/730.abstract

Singh, H. B., Kanakidou, M., Crutzen, P. J., & Jacob, D. J. (1995). High concentrations and photochemical fate of oxygenated hydrocarbons in the global troposphere. *Nature*, *378*(6552), 50–54. https://doi.org/10.1038/378050a0

Sioutas, C., Delfino, R. J., & Singh, M. (2005). Exposure assessment for atmospheric Ultrafine Particles (UFPs) and implications in epidemiologic research. *Environmental Health Perspectives*. https://doi.org/10.1289/ehp.7939

Slingo, A. (1990). Sensitivity of the Earth's radiation budget to changes in low clouds. *Nature*, *343*(6253), 49–51. https://doi.org/10.1038/343049a0

Slowik, J. G., Stainken, K., Davidovits, P., Williams, L. R., Jayne, J. T., Kolb, C. E., … Jimenez, J. L. (2004). Particle morphology and density characterization by combined mobility and aerodynamic diameter measurements. Part 2: Application to combustion-generated soot aerosols as a function of fuel equivalence ratio. *Aerosol Science and Technology*, *38*(12), 1206–1222. https://doi.org/10.1080/027868290903916

Snider, G., Weagle, C. L., Murdymootoo, K. K., Ring, A., Ritchie, Y., Stone, E., … Martin, R. V. (2016). Variation in global chemical composition of PM2.5: emerging results from SPARTAN. *Atmospheric Chemistry and Physics*, *16*(15), 9629–9653. https://doi.org/10.5194/acp-16-9629-2016

Solomon, P. a., & Hopke, P. K. (2008). The U . S . Environmental Protection Agency ' s Particulate Matter Supersites Program : An Integrated Synthesis of Scientific Findings and Policy- and Health-Relevant Insights. *Journal of the Air & Waste Management Association*, *58*, 1–2. https://doi.org/10.3155/1047-3289.58.13.S-1

Stohl, A. (2002). Chapter 21 Computation, accuracy and applications of trajectories- a review and bibliography. *Developments in Environmental Science*, *1*(C), 615–654. https://doi.org/10.1016/S1474-8177(02)80024-9

Stohl, A., Haimberger, L., Scheele, M. P., & Wernli, H. (2001). An intercomparison of results from three trajectory models. *Meteorological Applications*, *8*(2), 127–135. https://doi.org/10.1017/S1350482701002018

Targino, A. C., Gibson, M. D., Krecl, P., Rodrigues, M. V. C., dos Santos, M. M., & de Paula Corrêa, M. (2016). Hotspots of black carbon and PM2.5 in an urban area and relationships to traffic characteristics. *Environmental Pollution*, *218*, 475–486. https://doi.org/10.1016/j.envpol.2016.07.027

Tassia Owen. (2017). MODIS | Terra. Retrieved August 1, 2017, from https://terra.nasa.gov/about/terra-instruments/modis

Teather, K., Hogan, N., Critchley, K., Gibson, M. D., Craig, S., & Hill, J. (2013). Examining the links between air quality, climate change and respiratory health in Qatar. *Avicenna*, *2013*(1). https://doi.org/10.5339/avi.2013.9

TSI Incorporated. (2012a). *Aerodynamic ParTicle sizer® model 3321*. USA. Retrieved from http://www.tsi.com/uploadedFiles/_Site_Root/Products/Literature/Brochures/3321 Operation brochure US-5001468_WEB.pdf

TSI Incorporated. (2012b). *DustTrak DRX Aerosol Monitor Theory of Operation*. Retrieved from http://www.tsi.com/uploadedFiles/_Site_Root/Products/Literature/Application_Notes/EXPMN-002_DustTrak_DRX_Theory_of_Operation.pdf

TSI Incorporated. (2015). FAST MOBILITY PARTICLE SIZER ™ SPECTROMETER MODEL 3091 AEROSOL PARTICLES IN REAL-TIME IDEAL FOR A WIDE RANGE OF. Retrieved from http://www.tsi.com/uploadedFiles/_Site_Root/Products/Literature/Spec_Sheets/3091FMPS.pdf

Vaattovaara, P., Huttunen, P. E., Yoon, Y. J., Joutsensaari, J., Lehtinen, K. E. J., O'Dowd, C. D., & Laaksonen, A. (2006). The composition of nucleation and Aitken modes particles during coastal nucleation events: evidence for marine secondary organic contribution. *Atmospheric Chemistry and Physics Discussions*, *6*(2), 3337–3379. https://doi.org/10.5194/acpd-6-3337-2006

Wang, S., Nan, J., Shi, C., Fu, Q., Gao, S., Wang, D., … Zhou, B. (2015). Atmospheric ammonia and its impacts on regional air quality over the megacity of Shanghai, China. *Scientific Reports*, *5*(1), 15842. https://doi.org/10.1038/srep15842

Wark, K., Warner, C. F., & Davis, W. T. (1977). *Air pollution. Its origin and control*. *Environmental Pollution (1970)* (3rd ed., Vol. 13). https://doi.org/10.1016/0013-9327(77)90079-9

Waugh, D., Inkpen, T., Hingston, M., Keast, S., Mcpherson, J., Worthy, D., & Forbes, G. (2003). *Sable Island Air Monitoring Program Report: 2003-2006*. *Environmental Studies Research Funds Report* (Vol. 56). Retrieved from http://publications.gc.ca/collections/collection_2016/one-neb/NE22-4-181-eng.pdf

Wheeler, A. J., Gibson, M. D., MacNeill, M., Ward, T. J., Wallace, L. A., Kuchta, J., … Stieb, D. M. (2014). Impacts of air cleaners on indoor air quality in residences impacted by wood smoke. *Environmental Science and Technology*, *48*(20), 12157–12163. https://doi.org/10.1021/es503144h

WHO. (2013). *Health Effects of Particulate Matter*. https://doi.org/10.5124/jkma.2007.50.2.175

Wilson, W. E., & Suh, H. H. (1997). Fine particles and coarse particles: Concentration relationships relevant to epidemiologic studies. *Journal of the Air and Waste Management Association*, *47*(12), 1238–1249. https://doi.org/10.1080/10473289.1997.10464074

World Health Organization. (2013). Health Effects of Particulate Matter: Policy implications for countries in eastern Europe, Caucasus and central Asia. *Journal of the Korean Medical Association*, *50*(2), 20. https://doi.org/10.5124/jkma.2007.50.2.175

Yoon, Y. J., Ceburnis, D., Cavalli, F., Jourdan, O., Putaud, J. P., Facchini, M. C., … O'Dowd, C. D. (2007). Seasonal characteristics of the physicochemical properties of North Atlantic marine atmospheric aerosols. *Journal of Geophysical Research Atmospheres*, *112*(4), 1–14. https://doi.org/10.1029/2005JD007044

Appendix I

Appendix I shows the full detail of principle component analysis for $PM_{0.5-20}$ and UFP run in Minitab: (including unrotated factor loadings, rotated factor loadings and unsorted rotated factor loadings)

Principal Component Factor Analysis of the Correlation Matrix

Unrotated Factor Loadings and Communalities
88 cases used 278 cases contain missing values

Variable	Factor1	Factor2	Factor3	Factor4	Factor5	Factor6	Communality
20-30 nm	0.314	-0.353	0.100	-0.300	-0.356	0.619	0.834
30-50 nm	0.298	-0.315	0.455	0.230	-0.167	0.677	0.934
50-70 nm	0.148	-0.192	0.577	0.645	0.014	0.358	0.936
70-100 nm	0.083	-0.109	0.542	0.767	0.022	0.142	0.921
100-200 nm	0.137	0.012	0.452	0.817	-0.122	-0.102	0.916
200-800 nm	0.280	0.148	0.148	0.410	-0.318	-0.581	0.729
<0.523	0.220	0.293	0.235	0.646	-0.448	-0.223	0.857
0.542	0.515	0.513	-0.095	0.223	-0.543	0.009	0.881
0.583	0.626	0.516	-0.171	0.087	-0.468	0.026	0.914
0.626	0.743	0.492	-0.213	0.005	-0.350	-0.011	0.962
0.673	0.825	0.434	-0.231	-0.038	-0.209	-0.072	0.973
0.723	0.847	0.375	-0.250	-0.053	-0.106	-0.107	0.946
0.777	0.847	0.349	-0.272	-0.053	-0.058	-0.106	0.932
0.835	0.852	0.355	-0.271	-0.053	-0.044	-0.086	0.937
0.898	0.858	0.375	-0.254	-0.055	-0.041	-0.055	0.950
0.965	0.861	0.398	-0.244	-0.056	-0.048	-0.009	0.964
1.037	0.854	0.425	-0.244	-0.056	-0.063	0.053	0.978
1.114	0.846	0.439	-0.241	-0.059	-0.067	0.108	0.985
1.197	0.855	0.433	-0.221	-0.058	-0.039	0.125	0.988
1.286	0.872	0.419	-0.183	-0.033	0.001	0.131	0.988
1.382	0.873	0.413	-0.145	0.003	0.024	0.162	0.981
1.486	0.885	0.384	-0.091	0.035	0.080	0.157	0.972
1.596	0.879	0.362	-0.047	0.071	0.116	0.192	0.961
1.715	0.871	0.341	-0.023	0.075	0.137	0.233	0.953
1.843	0.900	0.271	0.028	0.067	0.215	0.186	0.970
1.981	0.926	0.186	0.063	0.038	0.278	0.082	0.982
2.129	0.929	0.118	0.102	0.038	0.307	-0.008	0.982
2.288	0.937	0.097	0.114	0.044	0.291	-0.003	0.987
2.458	0.937	0.064	0.136	0.053	0.293	-0.001	0.990
2.642	0.931	0.035	0.153	0.057	0.289	0.018	0.979
2.839	0.925	-0.016	0.174	0.041	0.298	-0.008	0.976
3.051	0.920	-0.079	0.203	0.043	0.286	-0.080	0.984
3.278	0.909	-0.139	0.227	0.052	0.260	-0.119	0.982
3.523	0.908	-0.187	0.232	0.036	0.220	-0.130	0.981
3.786	0.910	-0.227	0.221	0.003	0.179	-0.149	0.982
4.068	0.905	-0.267	0.215	-0.023	0.143	-0.165	0.984
4.371	0.898	-0.307	0.215	-0.043	0.106	-0.164	0.987
4.698	0.891	-0.348	0.219	-0.062	0.058	-0.147	0.991
5.048	0.870	-0.406	0.228	-0.073	-0.003	-0.119	0.994
5.425	0.848	-0.453	0.223	-0.089	-0.061	-0.092	0.995
5.829	0.821	-0.493	0.211	-0.116	-0.125	-0.063	0.994
6.264	0.794	-0.523	0.186	-0.140	-0.179	-0.042	0.992
6.732	0.773	-0.538	0.170	-0.151	-0.216	-0.034	0.986

7.234	0.766	-0.542	0.143	-0.153	-0.243	-0.020	0.985
7.774	0.755	-0.556	0.103	-0.156	-0.268	-0.003	0.986
8.354	0.786	-0.540	0.025	-0.133	-0.244	-0.030	0.988
8.977	0.770	-0.556	-0.026	-0.124	-0.258	-0.009	0.985
9.647	0.740	-0.562	-0.117	-0.084	-0.286	0.021	0.966
11.14	0.574	-0.612	-0.466	0.083	-0.173	0.051	0.960
12.86	0.363	-0.570	-0.687	0.201	0.004	0.045	0.970
13.82	0.195	-0.511	-0.781	0.264	0.063	0.029	0.984
14.86	0.127	-0.455	-0.813	0.284	0.094	0.028	0.975
15.96	0.070	-0.410	-0.833	0.318	0.124	0.007	0.985
18.43	0.023	-0.375	-0.833	0.339	0.128	0.039	0.967
19.81	0.013	-0.382	-0.822	0.315	0.188	0.022	0.957
Variance	30.471	8.182	6.544	3.196	2.594	1.832	52.819
% Var	0.554	0.149	0.119	0.058	0.047	0.033	0.960

Rotated Factor Loadings and Communalities
Varimax Rotation

Variable	Factor1	Factor2	Factor3	Factor4	Factor5	Factor6	Communality
20-30 nm	0.055	-0.424	0.017	-0.046	0.087	0.801	0.834
30-50 nm	0.020	-0.364	0.108	0.592	0.153	0.645	0.934
50-70 nm	-0.070	-0.192	0.120	0.917	0.057	0.191	0.936
70-100 nm	-0.087	-0.104	0.097	0.942	-0.072	-0.029	0.921
100-200 nm	0.002	-0.084	0.079	0.869	-0.335	-0.187	0.916
200-800 nm	0.168	-0.190	0.072	0.257	-0.641	-0.428	0.729
<0.523	0.239	0.023	0.114	0.560	-0.675	-0.130	0.857
0.542	0.684	0.021	0.068	0.119	-0.606	0.164	0.881
0.583	0.790	-0.045	0.042	-0.009	-0.508	0.167	0.914
0.626	0.874	-0.139	0.012	-0.083	-0.403	0.098	0.962
0.673	0.904	-0.235	-0.026	-0.118	-0.292	-0.006	0.973
0.723	0.891	-0.283	-0.070	-0.134	-0.209	-0.075	0.946
0.777	0.884	-0.291	-0.103	-0.138	-0.166	-0.094	0.932
0.835	0.894	-0.285	-0.102	-0.131	-0.146	-0.085	0.937
0.898	0.912	-0.276	-0.082	-0.117	-0.132	-0.063	0.950
0.965	0.931	-0.257	-0.065	-0.104	-0.120	-0.025	0.964
1.037	0.950	-0.225	-0.056	-0.092	-0.111	0.031	0.978
1.114	0.960	-0.201	-0.049	-0.081	-0.091	0.077	0.985
1.197	0.963	-0.211	-0.039	-0.063	-0.059	0.078	0.988
1.286	0.964	-0.233	-0.029	-0.017	-0.025	0.060	0.988
1.382	0.959	-0.235	-0.017	0.040	0.002	0.068	0.981
1.486	0.942	-0.267	-0.002	0.098	0.048	0.034	0.972
1.596	0.923	-0.273	0.006	0.161	0.090	0.041	0.961
1.715	0.905	-0.278	0.012	0.188	0.128	0.066	0.953
1.843	0.872	-0.361	0.021	0.205	0.190	-0.000	0.970
1.981	0.821	-0.464	0.023	0.182	0.220	-0.101	0.982
2.129	0.762	-0.535	0.028	0.183	0.220	-0.181	0.982
2.288	0.753	-0.556	0.027	0.196	0.210	-0.167	0.987
2.458	0.729	-0.582	0.027	0.215	0.216	-0.164	0.990
2.642	0.705	-0.597	0.027	0.231	0.225	-0.143	0.979
2.839	0.661	-0.639	0.030	0.224	0.235	-0.159	0.976
3.051	0.602	-0.698	0.031	0.222	0.204	-0.205	0.984
3.278	0.545	-0.744	0.027	0.230	0.174	-0.219	0.982
3.523	0.509	-0.784	0.021	0.214	0.146	-0.198	0.981
3.786	0.482	-0.820	0.012	0.174	0.117	-0.181	0.982
4.068	0.450	-0.852	0.003	0.143	0.091	-0.167	0.984
4.371	0.417	-0.879	-0.002	0.124	0.071	-0.138	0.987
4.698	0.385	-0.906	-0.005	0.111	0.048	-0.091	0.991
5.048	0.332	-0.933	-0.014	0.108	0.020	-0.026	0.994
5.425	0.287	-0.949	-0.027	0.093	-0.007	0.034	0.995

5.829	0.245	-0.957	-0.038	0.065	-0.037	0.101	0.994
6.264	0.211	-0.957	-0.057	0.033	-0.065	0.154	0.992
6.732	0.188	-0.951	-0.068	0.014	-0.089	0.183	0.986
7.234	0.187	-0.942	-0.089	0.000	-0.107	0.210	0.985
7.774	0.179	-0.931	-0.125	-0.019	-0.121	0.239	0.986
8.354	0.227	-0.918	-0.193	-0.036	-0.126	0.199	0.988
8.977	0.220	-0.898	-0.243	-0.048	-0.132	0.224	0.985
9.647	0.218	-0.845	-0.333	-0.052	-0.159	0.257	0.966
11.14	0.157	-0.624	-0.700	-0.059	-0.108	0.204	0.960
12.86	0.090	-0.362	-0.906	-0.063	-0.007	0.084	0.970
13.82	0.024	-0.174	-0.974	-0.068	0.008	0.021	0.984
14.86	0.018	-0.078	-0.981	-0.070	0.020	-0.007	0.975
15.96	0.007	-0.002	-0.989	-0.060	0.021	-0.051	0.985
18.43	-0.002	0.062	-0.980	-0.040	0.030	-0.036	0.967
19.81	-0.014	0.057	-0.969	-0.054	0.081	-0.075	0.957
Variance	20.311	17.218	6.458	4.001	2.638	2.195	52.819
% Var	0.369	0.313	0.117	0.073	0.048	0.040	0.960

Sorted Rotated Factor Loadings and Communalities

Variable	Factor1	Factor2	Factor3	Factor4	Factor5	Factor6	Communality
1.286	0.964	0.000	0.000	0.000	0.000	0.000	0.988
1.197	0.963	0.000	0.000	0.000	0.000	0.000	0.988
1.114	0.960	0.000	0.000	0.000	0.000	0.000	0.985
1.382	0.959	0.000	0.000	0.000	0.000	0.000	0.981
1.037	0.950	0.000	0.000	0.000	0.000	0.000	0.978
1.486	0.942	0.000	0.000	0.000	0.000	0.000	0.972
0.965	0.931	0.000	0.000	0.000	0.000	0.000	0.964
1.596	0.923	0.000	0.000	0.000	0.000	0.000	0.961
0.898	0.912	0.000	0.000	0.000	0.000	0.000	0.950
1.715	0.905	0.000	0.000	0.000	0.000	0.000	0.953
0.673	0.904	0.000	0.000	0.000	0.000	0.000	0.973
0.835	0.894	0.000	0.000	0.000	0.000	0.000	0.937
0.723	0.891	0.000	0.000	0.000	0.000	0.000	0.946
0.777	0.884	0.000	0.000	0.000	0.000	0.000	0.932
0.626	0.874	0.000	0.000	0.000	0.000	0.000	0.962
1.843	0.872	0.000	0.000	0.000	0.000	0.000	0.970
1.981	0.821	0.000	0.000	0.000	0.000	0.000	0.982
0.583	0.790	0.000	0.000	0.000	0.000	0.000	0.914
2.129	0.762	0.000	0.000	0.000	0.000	0.000	0.982
2.288	0.753	0.000	0.000	0.000	0.000	0.000	0.987
2.458	0.729	0.000	0.000	0.000	0.000	0.000	0.990
2.642	0.705	0.000	0.000	0.000	0.000	0.000	0.979
0.542	0.684	0.000	0.000	0.000	-0.606	0.000	0.881
2.839	0.661	-0.639	0.000	0.000	0.000	0.000	0.976
5.829	0.000	-0.957	0.000	0.000	0.000	0.000	0.994
6.264	0.000	-0.957	0.000	0.000	0.000	0.000	0.992
6.732	0.000	-0.951	0.000	0.000	0.000	0.000	0.986
5.425	0.000	-0.949	0.000	0.000	0.000	0.000	0.995
7.234	0.000	-0.942	0.000	0.000	0.000	0.000	0.985
5.048	0.000	-0.933	0.000	0.000	0.000	0.000	0.994
7.774	0.000	-0.931	0.000	0.000	0.000	0.000	0.986
8.354	0.000	-0.918	0.000	0.000	0.000	0.000	0.988
4.698	0.000	-0.906	0.000	0.000	0.000	0.000	0.991
8.977	0.000	-0.898	0.000	0.000	0.000	0.000	0.985
4.371	0.000	-0.879	0.000	0.000	0.000	0.000	0.987
4.068	0.000	-0.852	0.000	0.000	0.000	0.000	0.984

9.647	0.000	-0.845	0.000	0.000	0.000	0.000	0.966
3.786	0.000	-0.820	0.000	0.000	0.000	0.000	0.982
3.523	0.000	-0.784	0.000	0.000	0.000	0.000	0.981
3.278	0.000	-0.744	0.000	0.000	0.000	0.000	0.982
3.051	0.602	-0.698	0.000	0.000	0.000	0.000	0.984
15.96	0.000	0.000	-0.989	0.000	0.000	0.000	0.985
14.86	0.000	0.000	-0.981	0.000	0.000	0.000	0.975
18.43	0.000	0.000	-0.980	0.000	0.000	0.000	0.967
13.82	0.000	0.000	-0.974	0.000	0.000	0.000	0.984
19.81	0.000	0.000	-0.969	0.000	0.000	0.000	0.957
12.86	0.000	0.000	-0.906	0.000	0.000	0.000	0.970
11.14	0.000	-0.624	-0.700	0.000	0.000	0.000	0.960
70-100 nm	0.000	0.000	0.000	0.942	0.000	0.000	0.921
50-70 nm	0.000	0.000	0.000	0.917	0.000	0.000	0.936
100-200 nm	0.000	0.000	0.000	0.869	0.000	0.000	0.916
<0.523	0.000	0.000	0.000	0.000	-0.675	0.000	0.857
200-800 nm	0.000	0.000	0.000	0.000	-0.641	0.000	0.729
20-30 nm	0.000	0.000	0.000	0.000	0.000	0.801	0.834
30-50 nm	0.000	0.000	0.000	0.000	0.000	0.645	0.934
Variance	20.311	17.218	6.458	4.001	2.638	2.195	52.819
% Var	0.369	0.313	0.117	0.073	0.048	0.040	0.960

Factor Score Coefficients

Variable	Factor1	Factor2	Factor3	Factor4	Factor5	Factor6
20-30 nm	0.015	-0.001	0.021	0.001	0.057	0.374
30-50 nm	0.019	0.030	-0.002	0.180	0.093	0.331
50-70 nm	0.002	0.033	-0.024	0.261	0.043	0.124
70-100 nm	-0.008	0.027	-0.032	0.261	-0.016	0.016
100-200 nm	-0.017	0.013	-0.031	0.230	-0.126	-0.073
200-800 nm	-0.039	-0.047	0.006	0.028	-0.274	-0.231
<0.523	-0.006	0.010	-0.009	0.139	-0.255	-0.060
0.542	0.041	0.032	0.006	0.032	-0.205	0.086
0.583	0.049	0.029	0.009	-0.004	-0.166	0.087
0.626	0.052	0.021	0.009	-0.028	-0.129	0.054
0.673	0.049	0.010	0.005	-0.043	-0.093	0.003
0.723	0.045	0.005	-0.001	-0.049	-0.065	-0.031
0.777	0.046	0.005	-0.006	-0.049	-0.049	-0.040
0.835	0.048	0.008	-0.007	-0.045	-0.039	-0.033
0.898	0.052	0.012	-0.005	-0.041	-0.031	-0.020
0.965	0.056	0.017	-0.003	-0.034	-0.023	0.002
1.037	0.063	0.026	-0.003	-0.027	-0.014	0.033
1.114	0.068	0.033	-0.004	-0.020	-0.003	0.058
1.197	0.069	0.034	-0.003	-0.015	0.010	0.061
1.286	0.069	0.034	-0.003	-0.003	0.024	0.055
1.382	0.070	0.038	-0.005	0.014	0.036	0.062
1.486	0.068	0.036	-0.005	0.028	0.052	0.048
1.596	0.069	0.039	-0.007	0.047	0.069	0.055
1.715	0.070	0.042	-0.007	0.056	0.086	0.070
1.843	0.062	0.030	-0.005	0.054	0.103	0.035
1.981	0.049	0.011	-0.001	0.037	0.104	-0.021
2.129	0.036	-0.005	0.002	0.029	0.094	-0.067
2.288	0.034	-0.007	0.002	0.032	0.090	-0.061
2.458	0.031	-0.010	0.002	0.036	0.091	-0.061

2.642	0.030	-0.010	0.002	0.041	0.095	-0.051
2.839	0.023	-0.019	0.004	0.036	0.094	-0.063
3.051	0.012	-0.033	0.007	0.028	0.075	-0.092
3.278	0.002	-0.042	0.008	0.026	0.058	-0.105
3.523	-0.004	-0.050	0.010	0.020	0.044	-0.101
3.786	-0.009	-0.057	0.012	0.006	0.030	-0.099
4.068	-0.014	-0.064	0.014	-0.004	0.017	-0.097
4.371	-0.018	-0.070	0.015	-0.011	0.007	-0.087
4.698	-0.022	-0.073	0.017	-0.015	-0.002	-0.069
5.048	-0.027	-0.077	0.017	-0.015	-0.014	-0.042
5.425	-0.030	-0.080	0.018	-0.018	-0.025	-0.017
5.829	-0.033	-0.082	0.018	-0.024	-0.036	0.011
6.264	-0.035	-0.084	0.018	-0.032	-0.047	0.032
6.732	-0.036	-0.085	0.017	-0.036	-0.056	0.044
7.234	-0.036	-0.083	0.014	-0.037	-0.062	0.056
7.774	-0.035	-0.081	0.009	-0.039	-0.066	0.069
8.354	-0.032	-0.078	-0.002	-0.041	-0.067	0.050
8.977	-0.030	-0.074	-0.011	-0.040	-0.068	0.062
9.647	-0.026	-0.066	-0.027	-0.032	-0.074	0.079
11.14	-0.016	-0.035	-0.097	-0.004	-0.047	0.063
12.86	-0.005	-0.006	-0.141	0.017	-0.003	0.019
13.82	-0.001	0.010	-0.158	0.027	0.006	-0.005
14.86	0.004	0.019	-0.162	0.031	0.013	-0.013
15.96	0.006	0.026	-0.167	0.036	0.014	-0.031
18.43	0.010	0.034	-0.168	0.046	0.021	-0.020
19.81	0.009	0.032	-0.166	0.040	0.038	-0.037

Appendix II

Appendix II below shows the monthly mean *chl a* concentration [$*10^{-2}$ mg/m^3] at a resolution of 4 km taken by MODIS. They were retrieved from NASA Giovanni data system. It can be seen that phytoplankton bloom varies by locations.

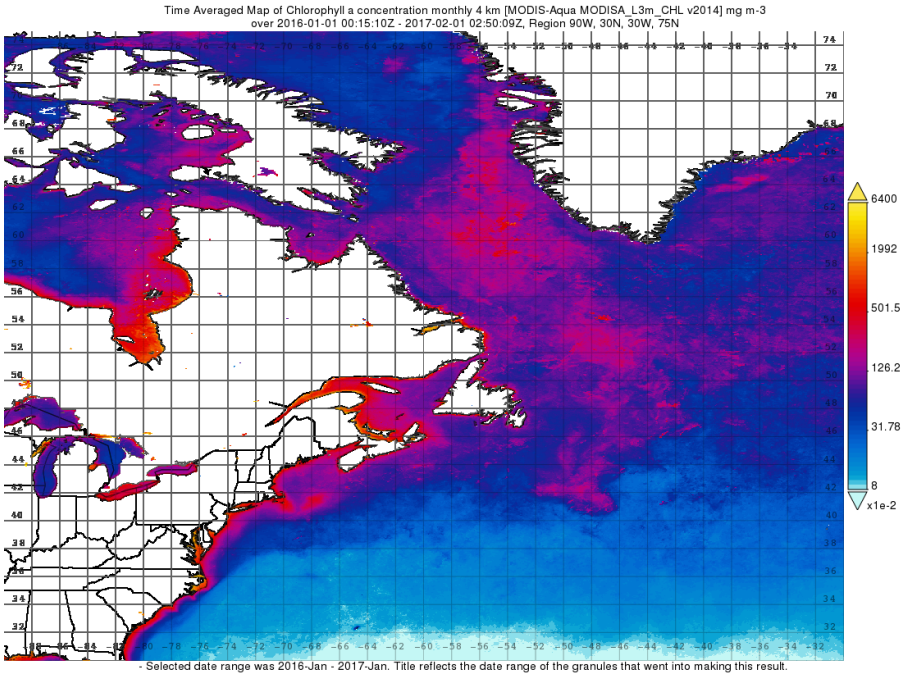

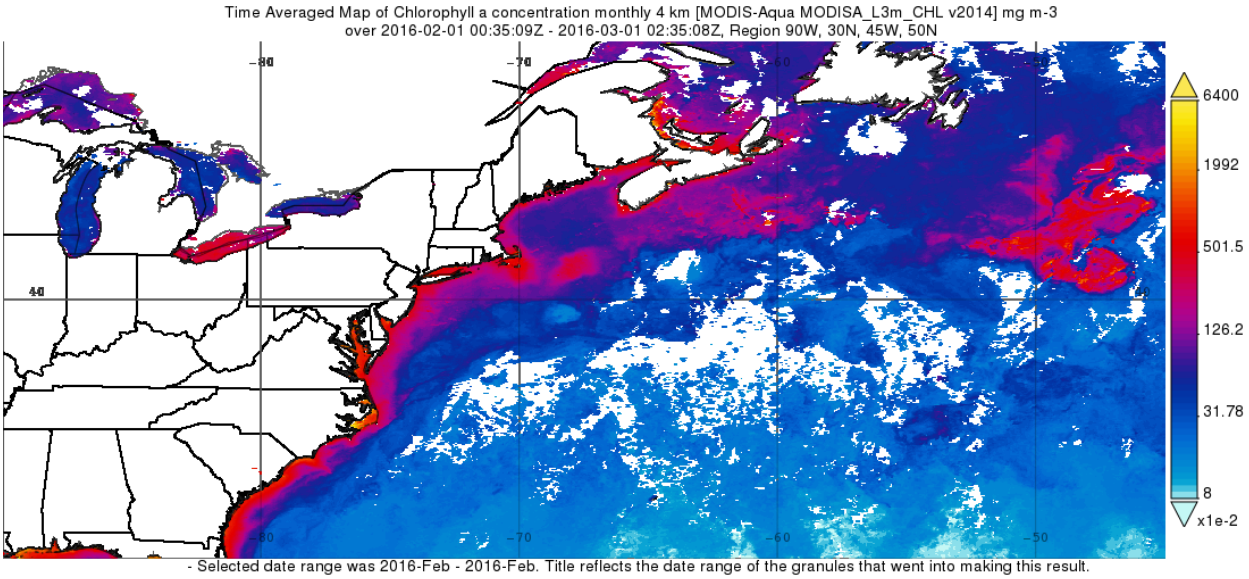

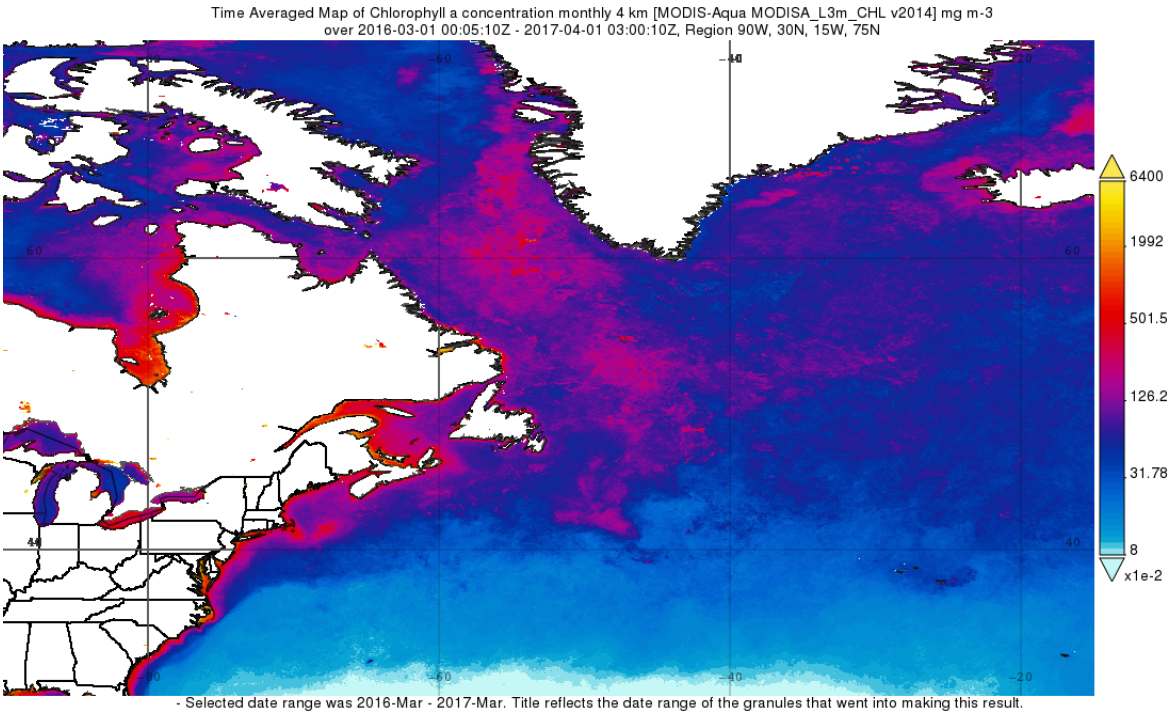

- Selected date range was 2016-Mar - 2017-Mar. Title reflects the date range of the granules that went into making this result.

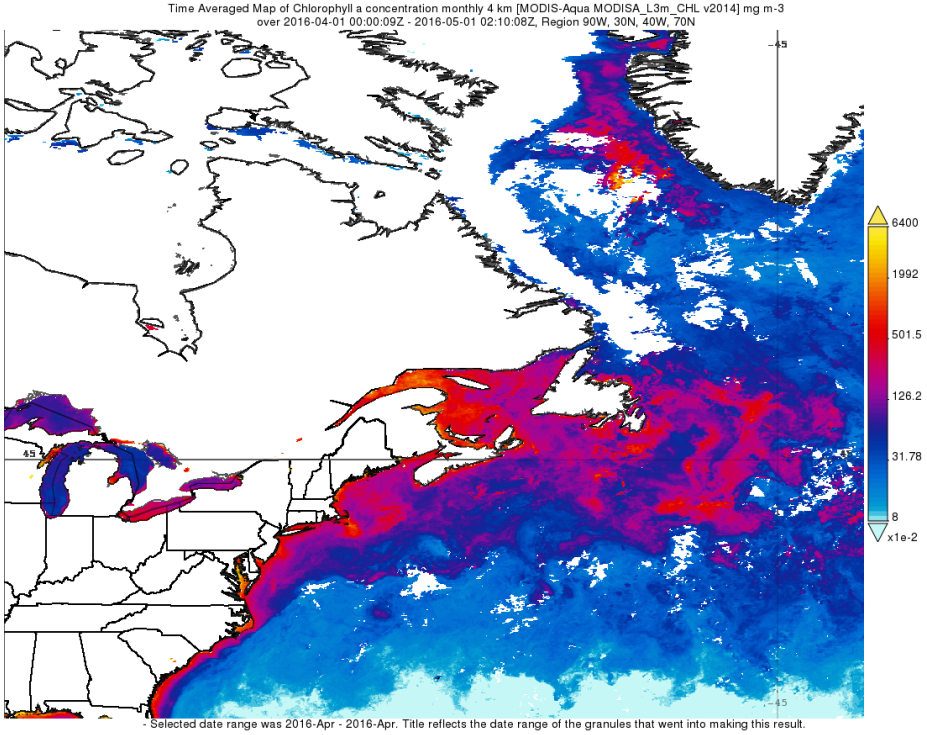

- Selected date range was 2016-Apr - 2016-Apr. Title reflects the date range of the granules that went into making this result.

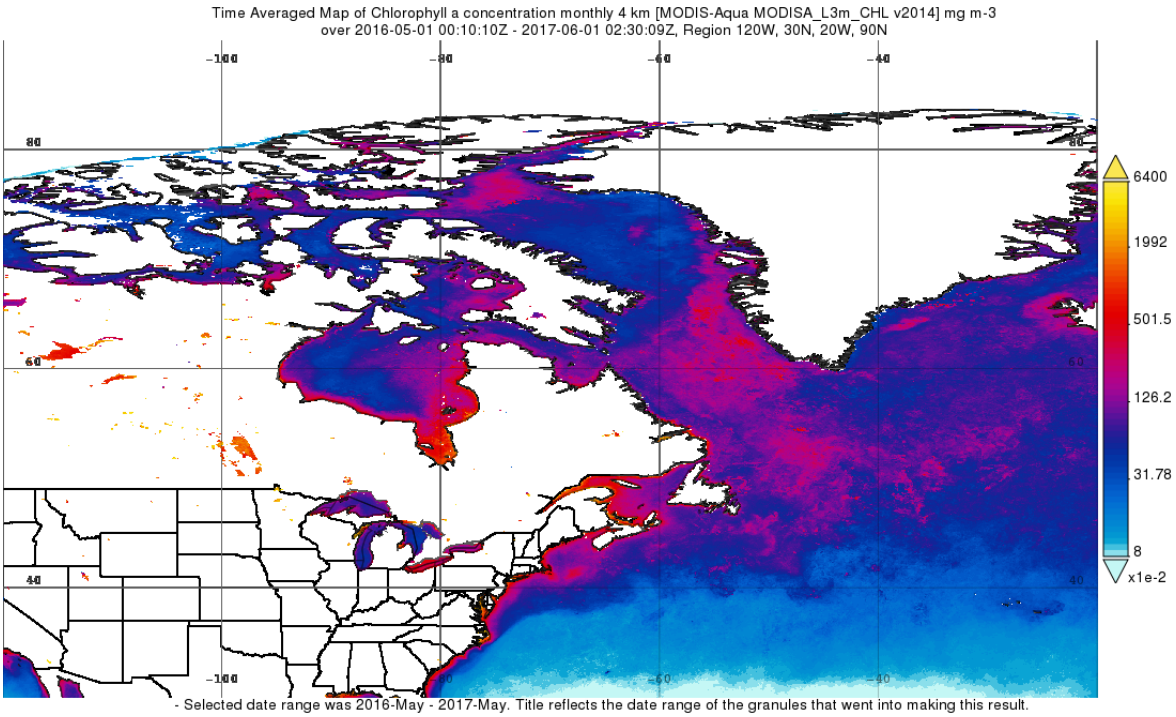

- Selected date range was 2016-May - 2017-May. Title reflects the date range of the granules that went into making this result.

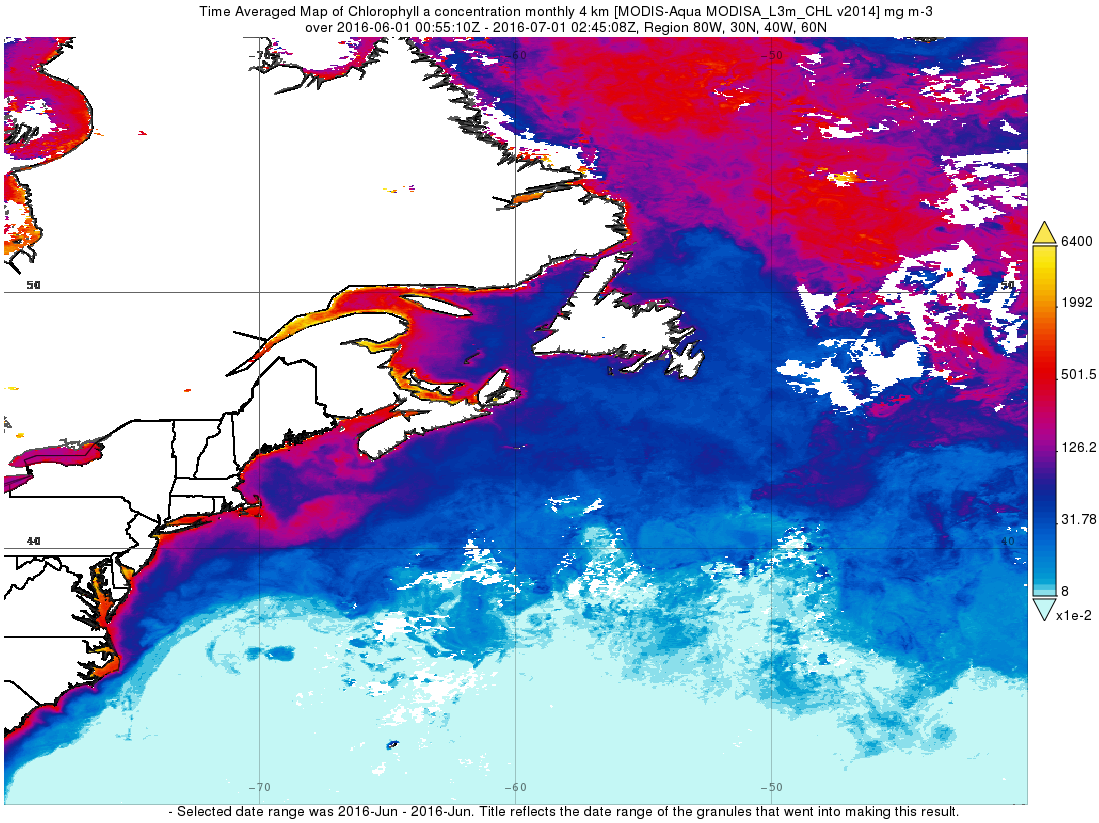

- Selected date range was 2016-Jun - 2016-Jun. Title reflects the date range of the granules that went into making this result.

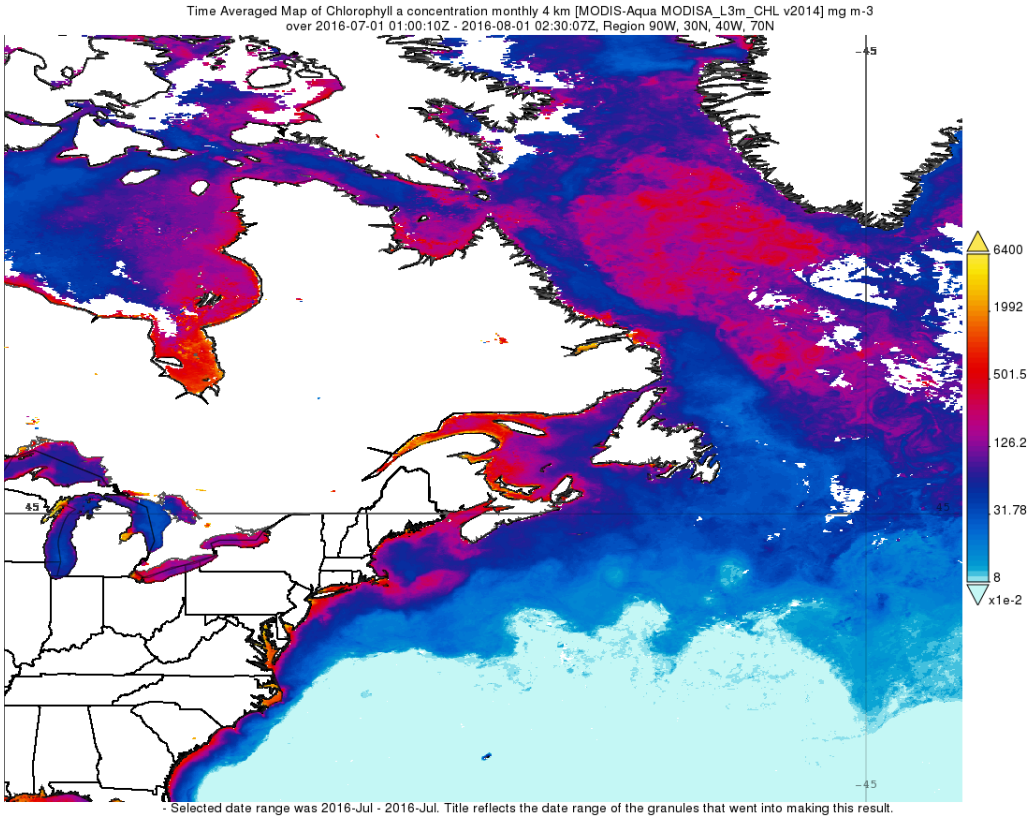
Time Averaged Map of Chlorophyll a concentration monthly 4 km [MODIS-Aqua MODISA_L3m_CHL v2014] mg m-3
over 2016-07-01 01:00:10Z - 2016-08-01 02:30:07Z, Region 90W, 30N, 40W, 70N
6400
1992
501.5
126.2
31.78
8
x1e-2
- Selected date range was 2016-Jul - 2016-Jul. Title reflects the date range of the granules that went into making this result.

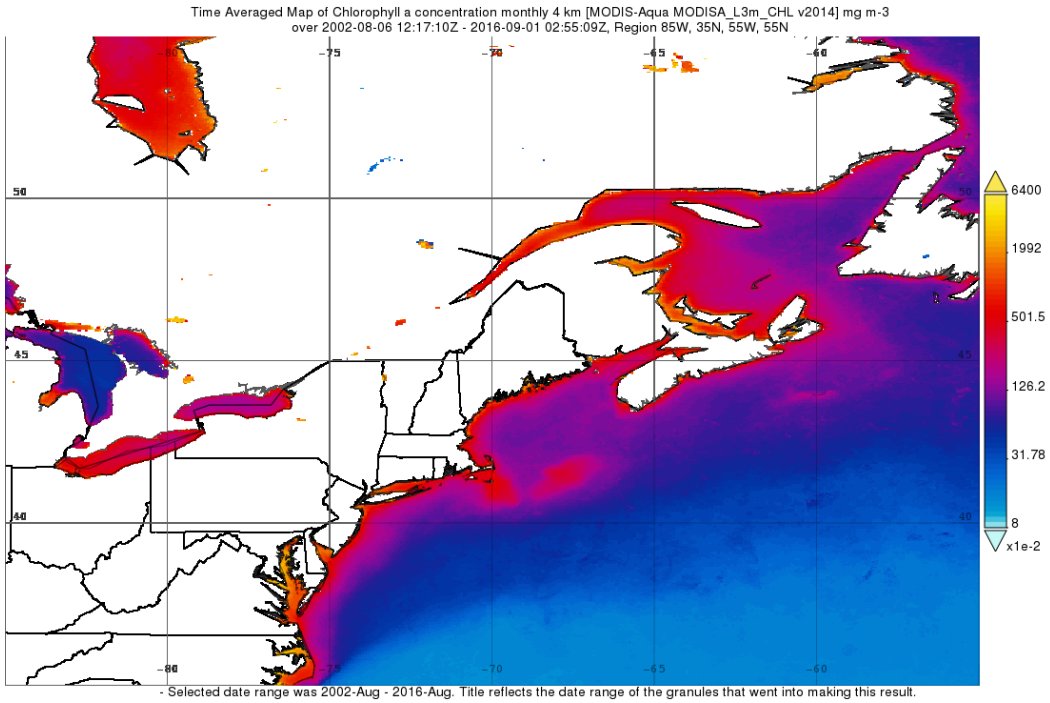
Time Averaged Map of Chlorophyll a concentration monthly 4 km [MODIS-Aqua MODISA_L3m_CHL v2014] mg m-3
over 2002-08-06 12:17:10Z - 2016-09-01 02:55:09Z, Region 85W, 35N, 55W, 55N
6400
1992
501.5
126.2
31.78
8
x1e-2
- Selected date range was 2002-Aug - 2016-Aug. Title reflects the date range of the granules that went into making this result.

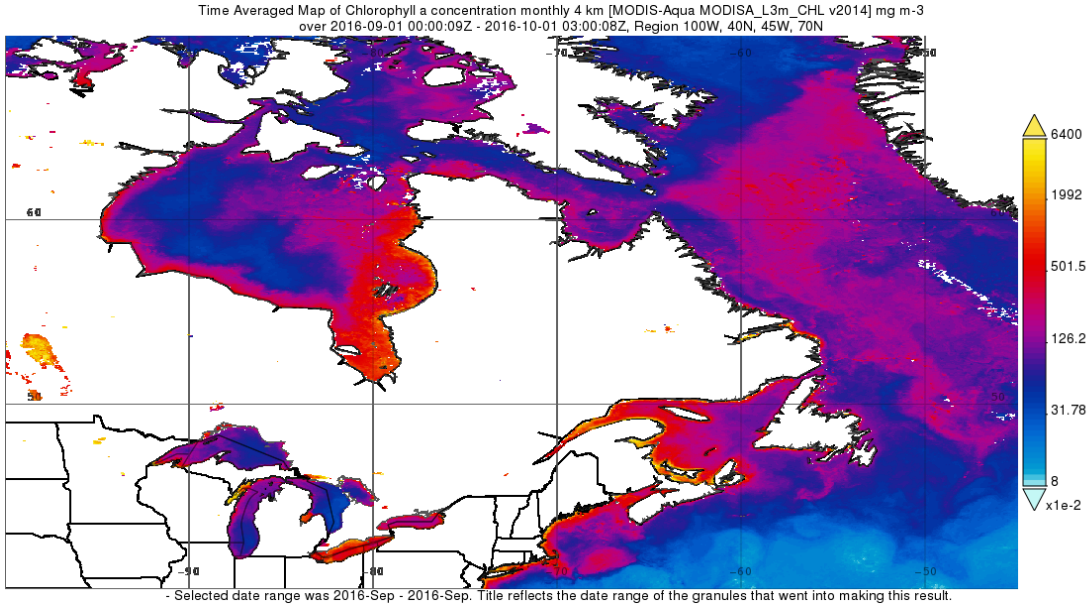

- Selected date range was 2016-Sep - 2016-Sep. Title reflects the date range of the granules that went into making this result.

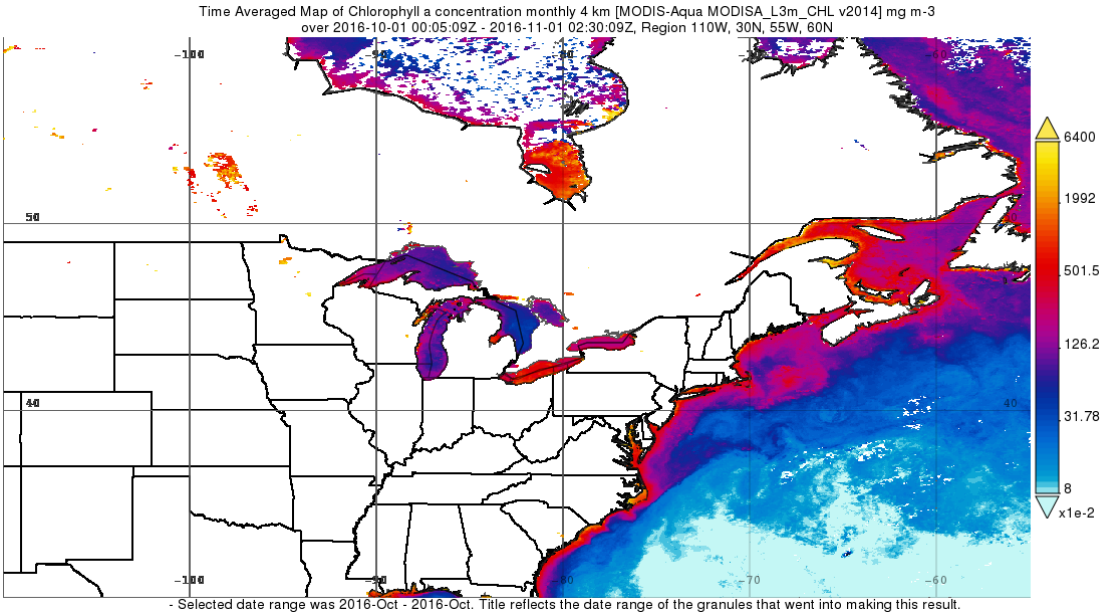

- Selected date range was 2016-Oct - 2016-Oct. Title reflects the date range of the granules that went into making this result.

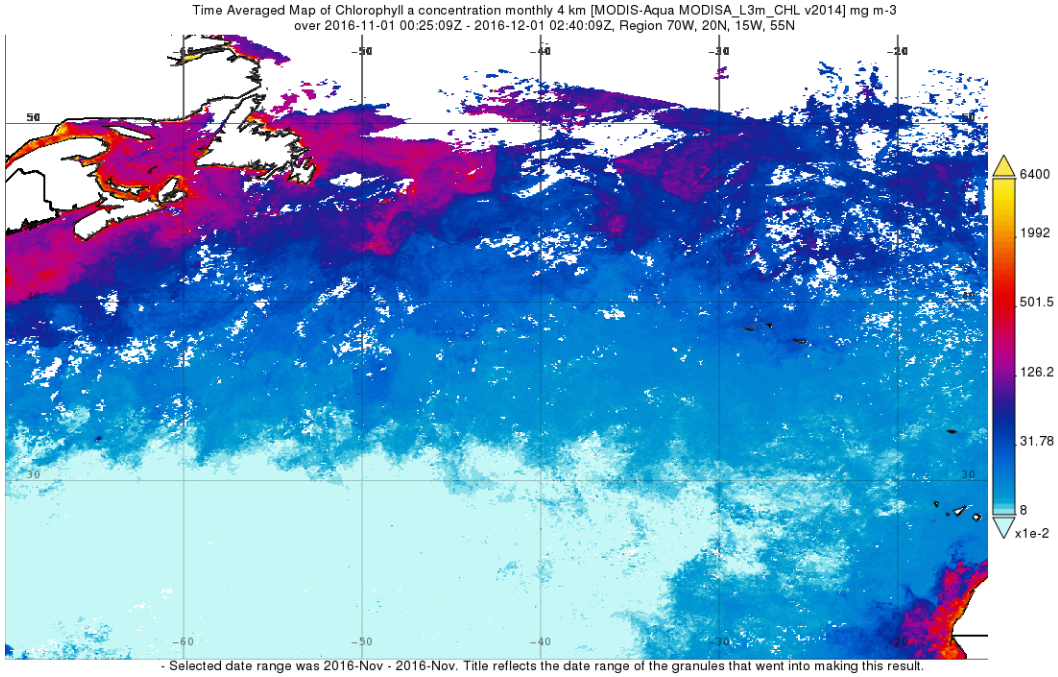

- Selected date range was 2016-Nov - 2016-Nov. Title reflects the date range of the granules that went into making this result.

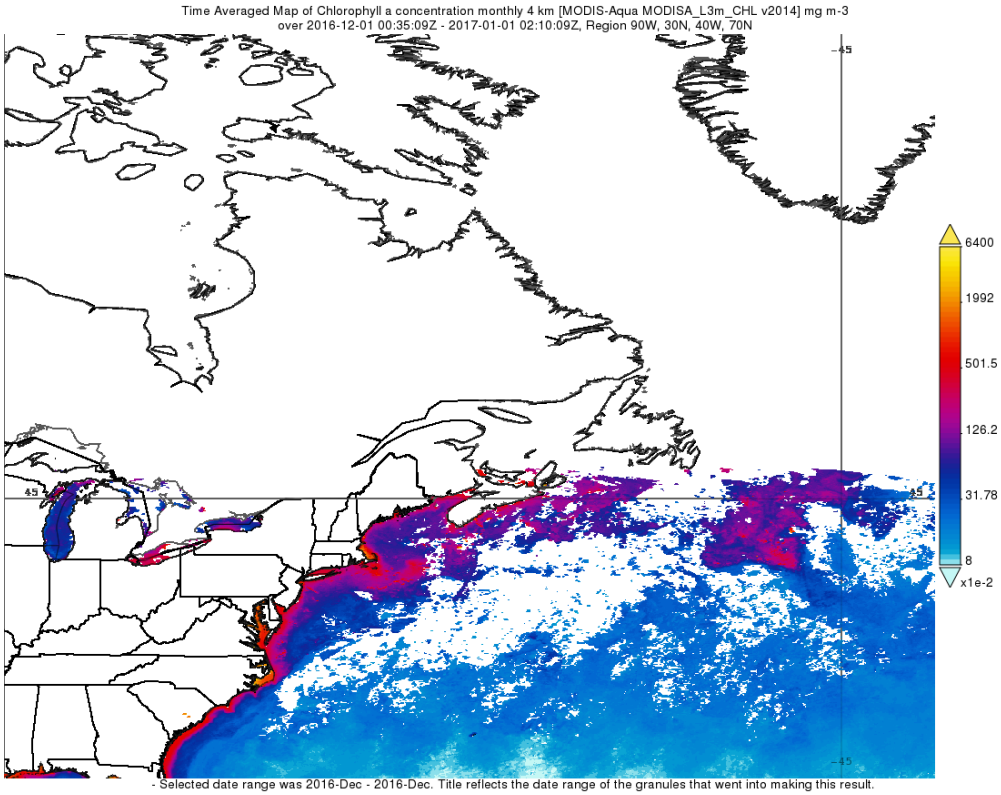

- Selected date range was 2016-Dec - 2016-Dec. Title reflects the date range of the granules that went into making this result.